QUANTIFICATION OF TURBULENCE STATISTICS FOR THE NEAR-WALL REGION IN UNSTRUCTURED PEBBLE BEDS USING DIRECT NUMERICAL SIMULATION

A Dissertation

by

GERRIT BOTHA

Submitted to the Office of Graduate and Professional Studies of
Texas A&M University
in partial fulfillment of the requirements for the degree of

DOCTOR OF PHILOSOPHY

Chair of Committee,	Yassin A. Hassan
Co-Chair of Committee,	Richard C. Kurwitz
Committee Members,	Maria King
	Hamn-Ching Chen
Head of Department,	John E. Hurtado

May 2019

Major Subject: Nuclear Engineering

ABSTRACT

The aim of this study was to employing high-fidelity computational fluid dynamics to investigate and quantify the turbulent flow effects for incompressible, isothermal fluid flows, in the near wall region of unstructured, randomly packed spheres. The flow domain treated in this study is a replication of an experimental setup and analogous to those encountered in pebble bed based high-temperature reactors. A new meshing strategy and meshing assumptions have been employed to decrease the mesh size and these were validated with the experimental results.

Quantifying turbulent flow effects sever a dual purpose: One, it assists lower-fidelity engineering tool development, such as those incorporating Reynolds averaged Navier-Stokes based methodologies, and two deepens our fundamental understanding of the physics involved for incompressible flows over complex geometries.

$Nek5000$, an open source spectral element computational fluid dynamics code, developed by Argonne National Lab was used to conduct this study. The code was used to perform a series of direct numerical simulations on the experimental geometry at low to moderate Reynolds numbers, matching the experimental flow parameters, to validate the model. This was done for a the full and section of the geometry to investigate the cross flow dependence in the problem.

Presented results include the comparison between experimental and numerical findings, the development of a high-fidelity database of the experimental geometry at low and moderate Reynolds number, identification of possible flow phenomena present in random packed spheres as well as the calculation of the first and second order statistics in the near wall domain of random packed spheres.

DEDICATION

To my Parents, Etienne and Louise Botha.

"Fear is temporary, regret is eternal."

ACKNOWLEDGMENTS

I would hereby want to thank my advisors, Dr. Yassin Hassan and Dr. Richard Kurwitz, for their support and guidance provided during my time at Texas A&M University. Their drive to proved the best opportunities for their students, both professionally and personally; and promote excellence in the field of nuclear engineering is an example that I shall strive to follow in my own career.

To Dr. Elia Merazi, Dr. Haomin Yuan and the research team at Argonne National Lab, for their numerous technical insights and contributions to the work presented in this dissertation. To Argonne National Lab, for providing internship opportunists for personal and professional growth in the field. The $Nek5000$ research team for providing the work opportunities and learning experiences, working with you all was insightful and enlightening to the field spectral element computational fluid dynamics and large scale computing.

To my parents and sister: Thank you for all the support and motivation you gave me on my adventures so far away from home. The encouragement, love and advice meant the world to me.

Then finally to all my friends, thank you for the support, without you all this would not be possible.

CONTRIBUTORS AND FUNDING SOURCES

Funding Sources

This research used resources of the Argonne Leadership Computing Facility, which is a DOE Office of Science User Facility supported under Contract DE-AC02-06CH11357.

NOMENCLATURE

Acronyms

ACF	Auto-correlation function
ALCF	Argonne Leadership Computing Facility
BDFk	k-step backward differentiation formula
CFD	Computational Fluid Dynamics
CFL	Courant-Friedrichs-Lewy
CU	Convective Unit
DNS	Direct Numerical Simulation
EXTk	k-th order explicit extrapolation schem
FCC	Face-centered-cubic
FTT	Flow through time
GIF	Generation Four International Forum
GLL	Gauss-Lobatto-Legendre
LES	Large eddy simulations
NS	Navier-Stokes
PBR	Pebble bed reactor
POD	Proper orthogonal decomposition
RANS	Reynolds Averaged Navier-Stokes
SEM	Spectral element methods
TKE	Turbulent kinetic energy
TRISO	Tri-structural isotropic
VHTR	Very high temperature gas-cooled reactors

Non-dimensional characteristic numbers

Fr	Froude number
Re	Reynolds number
St	Strouhal number

Characteristic units

L_D	Characteristic length scale
U_∞	Characteristic velocity

Mathematical operations

$\frac{\partial}{\partial[x_i,t]}$	Partial derivative
*	Non-dimensionalization
$\langle \dots \rangle$	Average
Σ	Summation

Mathematical symbols

ρ	Density
U_i	Instantaneous velocity
u_i	Fluctuating velocity
$\langle U_i \rangle$	Averaged velocity
P	Pressure
ν	Kinematic viscosity
F_i	Body forces
g	Gravitational acceleration
Δt	Time-step length
$\Delta x, \Delta y, \Delta z$	Spatial point separation
r	Radius
δ	Distance from wall

ϵ	Dissipation tensor
η	Kolmogorov length scale
θ	Angle
λ	Eigenvalues
μ	Dynamic viscosity
τ	Stress tensor
τ_η	Kolmogorov time scale
Ω	Domain
$\hat{\Omega}$	Reference element domain
u_η	Kolmogorov velocity scale
u^e_{ijk}	Basis Coefficient
N	Polynomial order
P	Production tensor
p	Pressure
T_{ijk}	Pressure transport tensor
Π_{ik}	Velocity-pressure-gradient tensor
x	Position
i, j, k	Index notation indices
r, t, s	Reference element indices
x, y, z	Cartesian components

TABLE OF CONTENTS

Page

ABSTRACT ii

DEDICATION iii

ACKNOWLEDGMENTS iv

CONTRIBUTORS AND FUNDING SOURCES v

NOMENCLATURE vi

TABLE OF CONTENTS ix

LIST OF FIGURES xii

LIST OF TABLES xviii

1. INTRODUCTION 1

    1.1 Background 1
        1.1.1 Pebble bed nuclear reactors 1
        1.1.2 Computational fluid dynamics 3
            1.1.2.1 Reynolds Averaged Navier-Stokes 4
            1.1.2.2 Large Eddy Simulations 4
            1.1.2.3 DNS 5
    1.2 Study objectives 5
    1.3 Dissertation structure 6
    1.4 Summary 7

2. THEORETICAL BACKGROUND 8

    2.1 Navier-Stokes equations 8
    2.2 Nek5000 schemes and Spectral element method 10
        2.2.1 Spatial discretization 10
        2.2.2 Temporal discretization 11
    2.3 Turbulent kinetic energy transport equation 12
    2.4 DNS requirements 13
    2.5 Proper orthogonal decomposition 14
    2.6 Summary 17

3. NUMERICAL EXPERIMENT I: TWO SPHERES WITH DIFFERENT SPACING 18

3.1 Background 18
3.2 Methodology 19
3.2.1 Case Outline 19
3.2.2 Computational Parameters 20
3.3 Results and Discussion 22
3.3.1 First and second order statistics 22
3.3.2 Turbulent kinetic energy 26
3.3.3 Proper orthogonal decomposition 31
3.4 Conclusions 34

4. NUMERICAL EXPERIMENT II: EXPERIMENTAL RANDOM PACKED PEBBLE BED 35

4.1 Background 35
4.2 Methodology 37
4.2.1 Case Outline 37
4.2.2 Meshing 40
4.2.3 Interpolation 43
4.2.4 Computational Consideration 44
4.2.5 Turbulent time scales 48
4.2.6 Statistical stationary 49
4.3 Results and Discussions 52
4.3.1 Inter-data-set comparisons 52
4.3.2 Turbulent Kinetic Energy 57
4.3.3 Experimental cross-verification 74
4.4 Conclusion 76

5. NUMERICAL EXPERIMENT III: RANDOM PACKED PEBBLE BED - REDUCED DOMAIN 78

5.1 Background 78
5.2 Methodology 79
5.2.1 Case Outline 80
5.2.2 Interpolation 81
5.2.3 Computational Consideration 82
5.3 Results and discussion 83
5.3.1 Plain selection 83
5.3.2 First-order statistics 86
5.3.3 Second-order statistics 93
5.3.4 TKE 100
5.4 Conclusions 108

6. CONCLUSIONS 111

6.1 Conclusions 111
6.1.1 Numerical Experiment I 111

6.1.2 Numerical Experiment II 112
6.1.3 Numerical Experiment III 113
6.1.4 Future Work 114

REFERENCES 115

APPENDIX A. REYNOLDS STRESSES 121

APPENDIX B. TURBULENT KINETIC ENERGY 123

B.1 Production 123
B.2 Dissipation 126

LIST OF FIGURES

FIGURE Page

1.1 Schematic representation of a PBR system connected to a Rankine cycle. 2

1.2 Schematic of CFD frameworks used to simulate fluid dynamics [1]. 4

3.1 Visual representation of the geometry and mesh. 20

3.2 Visual representation of the Kolmogorov calculations. 21

3.3 Pseudo-color field of the averaged stream wise velocity, $\langle U_y \rangle$, for the 4 sphere spacings. 23

3.4 Pseudo-color field of the in-plane Reynolds stress component, $\langle u_y u_y \rangle$, for the 4 sphere spacings. 24

3.5 Line profiles of $\langle u_y u_y \rangle$ in the wake region of two spheres. All the lines are normalized using the largest absolute value obtained from the six lines over the 4 spacings. 25

3.6 Pseudo-color field of the diagonal component of the turbulent kinetic energy production tensor, in the span wise direction P_{xx}, in the [0, y, z] plane. 27

3.7 Pseudo-color field of the diagonal component of the turbulent kinetic energy production tensor, in the stream wise direction P_{zz}, in the [0, y, z] plane. 27

3.8 Pseudo-color field of the diagonal component of the turbulent kinetic energy production tensor, in the stream wise direction P_{yy}, in the [0, y, z] plane. 28

3.9 Volume rendering of the span wise diagonal components of the turbulent kinetic energy dissipation tensor,P_{xx}, in the [0, y, z] plane. 29

3.10 Volume rendering of the span wise diagonal components of the turbulent kinetic energy dissipation tensor,P_{zz}, in the [0, y, z] plane. 29

3.11 Volume rendering of the stream wise diagonal components of the turbulent kinetic energy dissipation tensor,P_{yy}, in the [0, y, z] plane. 30

3.12 Pseudo-color field of the highest energy POD eigenfunctions in the [0, y, z] plane. .. 31

3.13 Pseudo-color field of the highest energy POD eigenfunctions in the [x, y, 0] plane. .. 32

4.1 Figures showing the experimental and computational domains. 38

4.2 The SolidWorks model superimposed on the experimental PIV region to compare accuracy of given pebble locations. 39

4.3 The method of how one tetrahedral element (left) gets converted to four hexahedral elements (right) [2]. 40

4.4 Hexahedral 8 element (left) and hexahedral 20 element (right) [3]. 41

4.5 A cut plane to show the effects of the moving mesh projection technique for N=3.... 42

4.6 Justification of the interpolation line and time history locations. 44

4.7 Section of the spectral-element mesh after sub-discretization, illustrating the boundary layers, pebble-pebble interactions and close proximity regions for N=5. 45

4.8 Volume rendering of U_{mag} after 35 CU of flow development. 46

4.9 Global maximum GLL spacing to Kolmogorov ratio for the different Reynolds numbers to ensure DNS requirements. 47

4.10 Temporal ACF for the entire time history (left) and zoomed in on the first 2 CU (right) of $\langle u_{mag} \rangle$ for the center point of line 3 (top) line 10 (bot). 49

4.11 Interpolated profiles for the steam-wise averaged velocity $\langle U_z \rangle$ (left) and the Reynolds stresses $\langle u_z u_z \rangle$ (right) for times $f(t) = 22$ FTT and $f(t+\tau) = 23$ FTT for the $N = 6$ data set. 50

4.12 Interpolated profiles for the averaged velocity $\langle U_x \rangle$ (left) and the Reynolds stresses $\langle u_x u_x \rangle$ (right) for times $f(t) = 22$ FTT and $f(t+\tau) = 23$ FTT for the $N = 6$ data set. 51

4.13 Interpolated profiles for the averaged velocity $\langle U_y \rangle$ (left) and the Reynolds stresses $\langle u_y u_y \rangle$ (right) for times $f(t) = 22$ FTT and $f(t+\tau) = 23$ FTT for the $N = 6$ data set. 51

4.14 Three-dimensional representation of the pebble packing structure around the plane of interest. 53

4.15 Pseudo color field of the in plane velocity magnitude in the plane [x/D,Y/D,-2.285D] with the velocity vector overlaid to show recirculation zones. 55

4.16 Pseudo color field of the in stream-wise Reynolds stress $\langle u_z u_z \rangle$ in the plane [x/D,Y/D,-2.285D]. 56

4.17 Pseudo color field of the averaged velocity magnitude $\langle U_{mag} \rangle$ for the the plane [-2.9D, Y/D, Z/D]. 57

4.18 Iso-volume rendering of the negative production $-10 \leq P_{zz} \leq -1$ for Re=1050 to show the complexity of the production tensor. 58

4.19 Pseudo color field of P_{xx} for the the plane [-2.9D, Y/D, Z/D]. 59

4.20 Pseudo color field of P_{yy} for the the plane [-2.9D, Y/D, Z/D]. 60

4.21 Pseudo color field of P_{zz} for the the plane [-2.9D, Y/D, Z/D]. 61

4.22 Pseudo color field of P_{xy} for the the plane [-2.9D, Y/D, Z/D]. 62

4.23 Pseudo color field of P_{xz} for the the plane [-2.9D, Y/D, Z/D]. 63

4.24 Pseudo color field of P_{yz} for the the plane [-2.9D, Y/D, Z/D]. 64

4.25 Pseudo color field of ϵ_{xx} for the the plane [-2.9D, Y/D, Z/D]. 65

4.26 Pseudo color field of ϵ_{yy} for the the plane [-2.9D, Y/D, Z/D]. 66

4.27 Pseudo color field of ϵ_{zz} for the the plane [-2.9D, Y/D, Z/D]. 67

4.28 Pseudo color field of ϵ_{xy} for the the plane [-2.9D, Y/D, Z/D]. 68

4.29 Pseudo color field of ϵ_{xz} for the the plane [-2.9D, Y/D, Z/D]. 69

4.30 Pseudo color field of ϵ_{yz} for the the plane [-2.9D, Y/D, Z/D]. 70

4.31 Pseudo color field of turbulent diffusion tensor in the, x-component, for the the plane [-2.9D, Y/D, Z/D]. 71

4.32 Pseudo color field of turbulent diffusion tensor in the, y-component, for the the plane [-2.9D, Y/D, Z/D]. 72

4.33 Pseudo color field of turbulent diffusion tensor in the, z-component, for the the plane [-2.9D, Y/D, Z/D]. 73

4.34 Pseudo color field of viscous diffusion tensor in the, x-component, for the the plane [-2.9D, Y/D, Z/D]. 74

4.35 Qualitative comparison between experimental, reprinted from [41] (left, averaged for $11s$) and DNS study (right, averaged for $115CU$) at $Z = -2.285D$. 75

5.1 Planar slices to show positions of interpolation lines. 80

5.2 Power spectrum taken in the center of the line location at [$Z/D = -2.285$]. 82

5.3 Psuedo-color of the averaged stream wise velocity, $\langle u_z \rangle$, for $Re = 1050$ to show the radial distribution of pebbles at different distances from the bounding wall. 84

5.4 Porisity analysis of the random packed pebble bed. 85

5.5 Psuedo-color of the averaged stream wise velocity, $\langle U_z \rangle$, for $Re = 1050$ to show the effects of the boundary condition for the simplified cases. 87

5.6 Normalized interpolated line profiles for $\langle U_z \rangle$. (Full: solid black, Wall: dash red, Symmetry: dot blue) 88

5.7 Psuedo-color of the averaged in-plane velocity, $\langle U_x \rangle$, for $Re = 1050$ to show the effects of the boundary condition for the simplified cases. 89

5.8 Normalized interpolated line profiles for $\langle U_x \rangle$. (Full: solid black, Wall: dash red, Symmetry: dot blue) 90

5.9 Psuedo-color of the averaged cross-flow velocity, $\langle U_y \rangle$, for $Re = 1050$ to show the effects of the boundary condition for the simplified cases. 91

5.10 Normalized interpolated line profiles for $\langle U_y \rangle$. (Full: solid black, Wall: dash red, Symmetry: dot blue) 92

5.11 Psuedo-color of the stream wise Reynolds stresses, $\langle u_z u_z \rangle$, for $Re = 1050$ to show the effects of the boundary condition for the simplified cases. 93

5.12 Normalized interpolated line profiles for $\langle u_z u_z \rangle$. (Full: solid black, Wall: dash red, Symmetry: dot blue) 94

5.13 Psuedo-color of the stream wise Reynolds stresses, $\langle u_x u_x \rangle$, for $Re = 1050$ to show the effects of the boundary condition for the simplified cases. 95

5.14 Normalized interpolated line profiles for $\langle u_x u_x \rangle$. (Full: solid black, Wall: dash red, Symmetry: dot blue) 96

5.15 Psuedo-color of the stream wise Reynolds stresses, $\langle u_y u_y \rangle$, for $Re = 1050$ to show the effects of the boundary condition for the simplified cases. 97

5.16 Normalized interpolated line profiles for $\langle u_y u_y \rangle$. (Full: solid black, Wall: dash red, Symmetry: dot blue) 98

5.17 Psuedo-color of the stream wise Production, $\langle P_{zz} \rangle$, for $Re = 1050$ to show the effects of the boundary condition for the simplified cases..... 99

5.18 Normalized interpolated line profiles for $\langle P_{zz} \rangle$. (Full: solid black, Wall: dash red, Symmetry: dot blue) 100

5.19 Psuedo-color of the in plane Production, P_{xx}, for $Re = 1050$ to show the effects of the boundary condition for the simplified cases..... 101

5.20 Normalized interpolated line profiles for P_{xx}. (Full: solid black, Wall: dash red, Symmetry: dot blue) 102

5.21 Psuedo-color of the cross flow Production, P_{yy}, for $Re = 1050$ to show the effects of the boundary condition for the simplified cases..... 103

5.22 Normalized interpolated line profiles for P_{yy}. (Full: solid black, Wall: dash red, Symmetry: dot blue) 104

5.23 Psuedo-color of the stream wise Production, ϵ_{zz}, for $Re = 1050$ to show the effects of the boundary condition for the simplified cases..... 105

5.24 Normalized interpolated line profiles for ϵ_{zz}. (Full: solid black, Wall: dash red, Symmetry: dot blue) 106

5.25 Psuedo-color of the in plane Production, ϵ_{xx}, for $Re = 1050$ to show the effects of the boundary condition for the simplified cases..... 107

5.26 Normalized interpolated line profiles for ϵ_{xx}. (Full: solid black, Wall: dash red, Symmetry: dot blue) 108

5.27 Psuedo-color of the cross flow Production, ϵ_{yy}, for $Re = 1050$ to show the effects of the boundary condition for the simplified cases. 109

5.28 Normalized interpolated line profiles for ϵ_{yy}. (Full: solid black, Wall: dash red, Symmetry: dot blue) 110

A.1 Normalized interpolated line profiles for $\langle u_x u_y \rangle$. (Full: solid black, Wall: dash red, Symmetry: dot blue) 121

A.2 Normalized interpolated line profiles for $\langle u_x u_z \rangle$. (Full: solid black, Wall: dash red, Symmetry: dot blue) 122

A.3 Normalized interpolated line profiles for $\langle u_y u_z \rangle$. (Full: solid black, Wall: dash red, Symmetry: dot blue) 122

B.1 Normalized interpolated line profiles for P_{xy}. (Full: solid black, Wall: dash red, Symmetry: dot blue) 123

B.2 Normalized interpolated line profiles for P_{xz}. (Full: solid black, Wall: dash red, Symmetry: dot blue) 124

B.3 Normalized interpolated line profiles for P_{yz}. (Full: solid black, Wall: dash red, Symmetry: dot blue) 125

B.4 Normalized interpolated line profiles for ϵ_{xy}. (Full: solid black, Wall: dash red, Symmetry: dot blue) 126

B.5 Normalized interpolated line profiles for ϵ_{xz}. (Full: solid black, Wall: dash red, Symmetry: dot blue) 127

B.6 Normalized interpolated line profiles for ϵ_{yz}. (Full: solid black, Wall: dash red, Symmetry: dot blue) 128

LIST OF TABLES

TABLE Page

4.1 Actual and Normalized Data for the Randomized Domain. 38

4.2 Computational Parameters to calculate Kolmogorov scales for Random packed pebble bed, Re = 1050. 48

5.1 Computational Parameters to calculate Kolmogorov scales for simplified Random packed pebble bed with symmetric boundary conditions, Re = 1050..... 83

1. INTRODUCTION

This study aims to investigate the fundamental turbulent flow effects that occur in the flow through a random, unstructured close-packed pebble bed, by employing direct numerical simulation (DNS). The goal was achieved by conducting numerical simulations and comparing the results with that of an experimental setup for different Reynolds numbers. From these, specific flow phenomena were investigated. A set of high-quality DNS reference data was developed and compared to that of work done, by L.Fick [1], on a structured packing arrangement. The transport of turbulent kinetic energy (TKE), temporal dependence of the averaged fields and the bounding wall effects on the bulk flow will be compared with experimental and previous results.

1.1 Background

Several concepts, systems and methods of importance to this study will be broadly outlined in the subsequent sections. An overview of pebble bed reactors (PBR), to which this research applies, is given. The tools used for fluid dynamic research, computational fluid dynamics (CFD), is covered. A brief outline of DNS, which is the CFD framework that will be used, is then discussed. The dissertation is then concluded by giving the significance and impact of this work.

1.1.1 Pebble bed nuclear reactors

The Generation Four International Forum (GIF) proposed the PBRs as one of the two very high-temperature gas-cooled reactors (VHTR) that is a concept to replace current operational nuclear power reactors [4]. The reactor is designed on the basses of an unstructured bed of spherical graphite fuel pebbles in which tri-structural isotropic (TRISO) fuel particles are dispersed [5]. The design offers energy transfer and conversion by either helium or molten salt as the primary working fluid. This can be coupled via a heat exchanger, to a secondary gas (Brayton) or steam (Rankine) thermodynamic power cycle [6]. The higher obtainable coolant temperatures that are achievable by these reactors open the versatility to be used for process heat and hydrogen production. These designs offer several improvements over the current light water reactor-based designs [1]:

1. Improved economics by having higher thermal efficiency.

2. Application flexibility by having higher core outlet temperatures allowing power generation and/or processes heat and hydrogen production.

3. Increased safety by having a lower power density and the stability of the graphite moderator and core during accidents.

Fig. 1.1 gives the schematic representation of a PBR that is connected to a Rankine cycle. The core graphite can either be in an annular or cylindrical configuration. Depending on the core power output, this region is filled with the order of hundreds of thousands of spherical graphite pebbles. The coolant is forced in from the top of the core, to avoid a fluidized bed and air ingress, which may result in undesired mechanical stress, wear and vibrations.

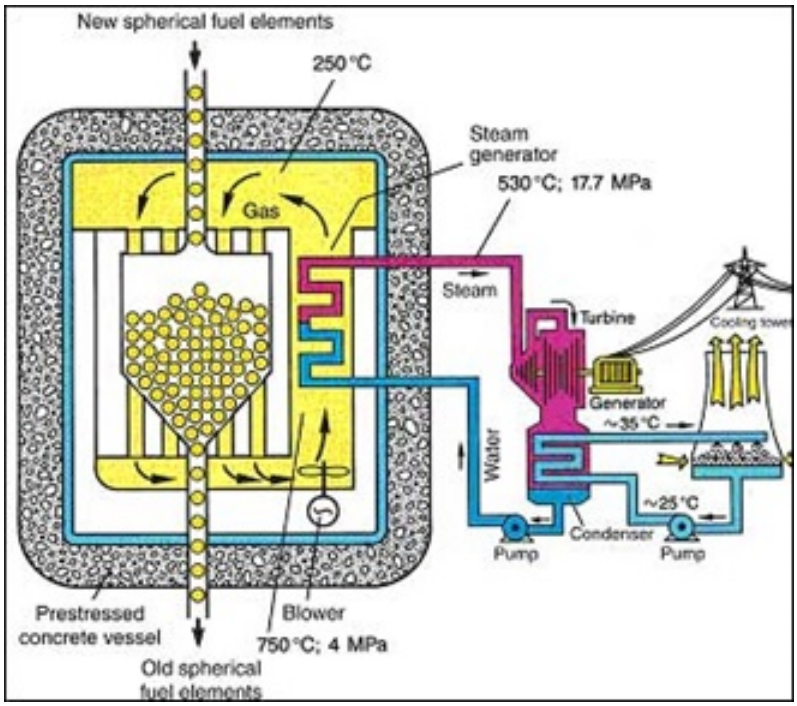

Figure 1.1: Schematic representation of a PBR system connected to a Rankine cycle.

Depending on the designed, it can either incorporate online or offline refueling. When the

system calls for online refueling, the pebbles are displaced towards the bottom of the core, where they are collected before they are re-inserted at the top. Due to the slow rate of the displacement the core can be considered as stationary when flow simulations are conducted.

Even though a few reactors, based on this designed, have been constructed, there are still several technical challenges that have been left unanswered. Some of which appear due to the constant change of the core geometry as pebbles are removed and added. Thus employing CFD, the relevant issues, such as coolant flow path predictions, stagnation and resulting hot-spot generation can be addressed for the bulk and near wall region.

1.1.2 Computational fluid dynamics

Most engineering systems that utilize a working fluid to transport energy, like nuclear reactors, operate in the turbulent fluid-flow regime. Turbulence is a time-dependent, three-dimensional, non-linear process, which can accurately be described by the Navier-Stokes (NS) equations [7]. Thus incorporating various frameworks and varying degrees of simplifications, CFD tools solve these equations numerically, for flows of interest.

As the computation resources to our disposal advanced over the last couple of decades, CFD has become an integrated part of the engineering design and research. CFD solutions provide simplified, safer and more cost-effective tools for research and development, than experiments. Complex phenomena, such as fluid flow and heat transfer can be characterized, without the need for complex experimental set-ups, thus cutting down on cost and set-up time. Even with this advantage, CFD tools are based on mathematical simplifications and assumptions, thus making simulating complex turbulent flow practical in general engineering and design applications. To ensure the assumptions and simplifications are adequate, CFD tools need to be validated, before the results obtained can be trusted for new and novel applications.

The different CFD frameworks for numerical simulations of pebble beds can be found in the subsequent sections. For a more detailed review of the framework, consult [8].

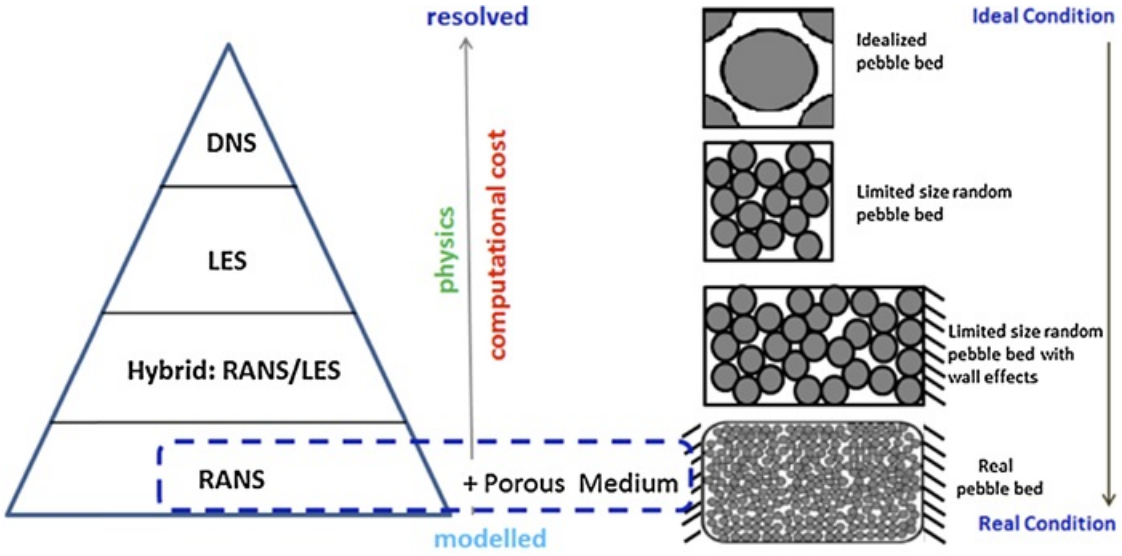

Figure 1.2: Schematic of CFD frameworks used to simulate fluid dynamics [1].

1.1.2.1 Reynolds Averaged Navier-Stokes

Depending on the simplifications and assumptions applied to the NS equations different numerical frameworks come to light. Fig. 1.2 details the different employable frameworks, their application and corresponding computational cost and accuracy. Full-scale practical systems can be approximated by using Reynolds averaged Navier-Stokes (RANS) and porous media based frameworks. These are computationally inexpensive, but rely on numerous assumptions and closure models. For the results from these frameworks to be accurate, explicit testing has to be done to ensure they deliver accurate results for the given geometry under question. RANS based studies have shown the limited ability of these models to generate accurate results in pebble based geometries [9]. RANS models are capable of capturing the overall averaged behavior of a system, but lack as the detail of the underlying physics is lost in the averaging process.

1.1.2.2 Large Eddy Simulations

With an increase in computational cost, higher fidelity methods, such as large eddy simulations (LES) and hybrid RANS/LES methods can capture more of the underlying physical phenomena present in complex geometries [10]. As computational tools and computer resources become more

advanced, these tools become more lucrative for engineering design and research [11, 12].

1.1.2.3 DNS

The most accurate is that of DNS, which explicitly solves the discretized NS equations using numerical methods. The unrepresented accuracy comes from not needing to model the small scale turbulent motions, unlike the RANS and LES approaches. With the high spatial and temporal accuracy comes the biggest increase in computational costs, due to the capture of all the physical phenomena in the flow. Due to the high expense, DNS is not used for design, but rather for fundamental research. For this study NEk5000, a spectral element CFD code, will be employed.

Spectral element methods (SEM) are higher-order spatial methods, which is a subclass of finite-element frameworks [13]. Due to the low numerical dissipation of SEM frameworks, it is well suited for DNS, where detailed investigations are performed on the physical flow effects and dissipation of turbulent kinetic energy in complex flow geometry.

The computational cost associated with DNS is still the biggest prohibiter for using DNS. This limits both the physical size of the computational domain, as well as the achievable Reynolds number that can be investigated. Thus DNS is applied to smaller idealized subsystems that are found within practical systems, while low to moderate Reynolds numbers can be considered.

1.2 Study objectives

The objective of this study is to add to our understanding of the dynamics of turbulent flow in unstructured random PBR geometries. The results of this study can be used to optimize the current engineering research and design tools. This allows the broader application of this work.

By performing several simulations applicable to the flow in pebble beds, and analyzing the results the above-mentioned goal can be obtained. Three studies, with a specific set of goals where proposed and conducted. The goals of the different studies can be summarized as follow:

1. Flow over two spheres in free stream with different spacing:

    - Verify the simulation methodology by using available numerical simulations and experimental literature.

- Confirm increased meta-stable behaviour of data averaged over long time-integration periods
- Confirm existence of critical sphere placement for wake separation for spheres in tandem.

2. Experimental geometry:

   - Verify simulation methodology and mesh generation of unstructured random packed pebbles.
   - Verify simulation boundary conditions and simplification in geometry.
   - Compare first- and second order turbulent statistics to that of experimental setup using moderate Reynolds numbers.
   - Generate a high-fidelity database of time-invariant flow data:
     - First- and second-order turbulence statistics.
     - Turbulent kinetic energy budgets.
   - Identify and isolate temporal instabilities present in the flow.

3. Simplified Experimental geometry:

   - Investigate the decrease in computational cost by simulating a smaller domain
   - Investigate how different boundary conditions affect the flow in the random pack pebble bed.
   - Compare first- and second order turbulent statistics to that of the full numerical setup using moderate Reynolds numbers.

1.3 Dissertation structure

For this dissertation, each numerical experiment will be treated as independent, with their own results and discussion sections. The different cases will be tied together with an overall introduction, background, mathematical theory and conclusion sections.

A brief overview of the dissertation can be summarized as:

- Section 1: Introduction. General information and relative background and objectives for the study.
- Section 2: Mathematical theory. A brief overview of the required mathematical theory required for the subsections.
- Section 3-5: Numerical studies
  - Two spheres in tandem with different spacing
  - Experimental geometry verification
  - Simplified domain investigation
- Section 6: Conclusion and future work

1.4 Summary

To summarize and finish this section an introduction of the practical engineering system under consideration was given, along with the introduction to CFD and DNS, as the tools employed for the study.

The proposed objectives, to create a first-of-its-kind, DNS results for the near wall region of a random packed pebble bed was given, as well as the steps that will be taken to achieve these goals.

2. THEORETICAL BACKGROUND

The mathematical theory relevant, to the preformed study, will be covered in this section. As the tools and theory used here are already well established, only a short discussion, with the relevant reference will be given. For the derivations of these tools the reader can consult the references. When theory, that is only relevant to a specific section is used, it will be covered there accordingly. This will ensure that this chapter remains brief.

The conservation laws in the form of the NS equations are the basis for this study. The numerical methods employed by Nek5000 to solve the discretized NS equations are then discussed. The TKE transport equations, and the relevant terms are then discussed. To ensure that the numerical simulation conforms to DNS requirements, which itself requires access to information in the TKE budgets, are then treated.

2.1 Navier-Stokes equations

Using the derivation done by [7], the NS equations for incompressible fluids, with constant properties, give the conservation of mass, in Einstein notation, as:

$$\frac{\partial \rho}{\partial t} + \frac{\partial}{\partial x_i} = 0 \tag{2.1}$$

And the conservation of momentum:

$$\frac{\partial U_i}{\partial t} + U_j \frac{\partial U_i}{\partial x_j} = -\frac{\partial p}{\partial x_i} + \nu \frac{\partial U_j}{\partial x_i} \frac{\partial U_i}{\partial x_j} + \rho F_i \tag{2.2}$$

Because the flow under consideration has constant fluid properties the conservation of mass Eq.(2.1) reduces to the divergence-free condition:

$$\frac{\partial U_i}{\partial x_i} = 0 \tag{2.3}$$

To simplify, the NS equations are non-dimensionalised using appropriate characteristic parameters. Defining L_D and U_∞ as the characteristic length and velocity scales, the following non-dimensional length, velocity and time occur:

$$x_i^* = x_i / L_D \tag{2.4}$$

$$U_i^* = U_i / U_\infty \tag{2.5}$$

$$t^* = \frac{t}{L_D / U_\infty} \tag{2.6}$$

from Eq. 2.4-2.6 and assuming that convection is dominant the non-dimensional pressure is:

$$p^* = \frac{p}{\rho U_\infty} \tag{2.7}$$

This allows the NS equations to written in the non-dimensionalized form:

$$\frac{\partial U_i^*}{\partial t^*} + U_j^* \frac{\partial U_i^*}{\partial x_j^*} = \frac{\partial p^*}{\partial x_i^*} + \frac{1}{Re} \frac{\partial U_j^*}{\partial x_i^*} \frac{\partial U_i^*}{\partial x_j^*} + \frac{1}{Fr} \frac{F_i}{g} \tag{2.8}$$

with the two dimensional less Reynolds and Froud numbers given as:

$$Re = \frac{U_\infty L_D}{\nu} \tag{2.9}$$

$$Fr = \frac{U_\infty^2}{g L_D} \tag{2.10}$$

With no external forces acting on the fluid, the Froud number, $Fr \to \infty$. This leaves us with the non-dimensional equations:

$$\frac{\partial U_i^*}{\partial x_j^*} = 0 \tag{2.11}$$

$$\frac{\partial U_i^*}{\partial t^*} + U_j^* \frac{\partial U_i^*}{\partial x_j^*} = -\frac{\partial p^*}{\partial x_i^*} + \frac{1}{Re} \frac{\partial U_j^*}{\partial x_i^*} \frac{\partial U_i^*}{\partial x_j^*} \tag{2.12}$$

This is the governing equations that will be used for the remained of the dissertation. For ease of writing and simplification, the * is removed from the notation, as it is assumed we are working with the non-dimensional forms of the equations. Using Reynolds decomposition, the instantaneous velocity fields can be decomposed as the sum of the average and fluctuating fields:

$$U_i = \langle U_i \rangle + u_i \tag{2.13}$$

Thus when taking the density as unity and calculating the variance and covariance of the fluctuating fields, the Reynolds stresses can be given as $\langle u_i u_j \rangle$.

2.2 Nek5000 schemes and Spectral element method

Partial differential equations can be solved by using the SEM, a high-order finite element method. The domain is discretization into disjointed elements, with the solution and geometry approximated by high order polynomial expansions within each element [13, 14]. These methods combine the geometric flexibility of low-order finite-element techniques with the high-order accuracy of the spectral method.

For three-dimensional flows, as considered for turbulence, the SEM divides the computational domain into hexahedral elements. Each element‘s face consists of non-degenerate parallelograms. Each element is sub-divided onto a local Cartesian mesh, resulting in a NxNxN tensor [15]. The solution is evaluated in this tensor-product box using Lagrange polynomials, evaluated at Gauss-Lobatto-Legendre (GLL) collocation points. GLL distributions are clustered closer to the boundary of the element, this is due to the accuracy in the approximation, interpolation and quadrature properties. An overview of how the SEM is implemented in NEK5000 will now be discussed. For more about SEM [16] can be consulted.

2.2.1 Spatial discretization

Originally SEM was developed to use Chebyshev collection points within each element [13], but later the scheme was modified to use GLL points by incorporating the Galerkin formulation [14].

With SEM, the entire domain, Ω_f, is comprised of a set of non-overlapping sub-domains, Ω^e, so that:

$$\Omega_f = \bigcup_{e=1}^{E_f} \Omega^e \quad , e \in E_f \tag{2.14}$$

within each element, a variable $u(x, y, z)$ can be represented as:

$$u(x, y, z)|_{\Omega^e} = \sum_{k=0}^{N} \sum_{j=0}^{N} \sum_{i=0}^{N} u^e_{ijk} h_i(r) h_j(s) h_k(t) \tag{2.15}$$

where the basis coefficients are given by u^e_{ijk}. $h_i(r)$, $h_j(r)$ and $h_k(r)$ are the N-th order one-dimensional Lagrange polynomials evaluated at the GLL points. The arguments of the polynomials (r, s, t) are the coordinates in the canonical reference element, $\hat{\Omega} = [-1, 1]^3$. For $(x, y, z) \in \Omega^e$ an non-parametric mapping relates Ω^e as the the image of $\hat{\Omega}$ under the polynomial mapping in 2.15. For this mapping it is assumed that the angles at the edges of Ω^e are bounded away from 0° and 180°, thus making it un-invertible with smooth element edges.

The pressure is discretized in the same manner as that of the velocity, where the only difference being the Lagrange interpolants are of the order $N - 2$, when evaluating the GLL points. Thus this forms the well known $\mathbb{P}_N - \mathbb{P}_{N-2}$ SEM formulation [1, 15].

2.2.2 Temporal discretization

Time stepping in Nek5000 is solved by means of a semi-implicit scheme. With this, the viscous terms in the NS equation, Eq. 2.12, is solved by using a k-step backward differentiation formula (BDFk) that is based on a truncated Taylor expansion. The convective term, which is non-linear, is treated with a k-th order explicit extrapolation scheme (EXTk) [15]. For the work done, the simulations were solved using $k = 3$ resulting in a BDF3/EXT3 time stepping scheme. This scheme is globally third-order accurate.

In order to maintain stability, with an explicit numerical scheme, there is a time-constrained placed on the time step size, Δt, that can be used. The Courant-Friedrichs-Lewy (CFL) condition

gives the stability criteria for the time step as:

$$\Delta t \leq CFL \times MIN_{\Omega_f} \left\{ \frac{\Delta x}{|u_x|}, \frac{\Delta y}{|u_y|}, \frac{\Delta z}{|u_z|} \right\} \tag{2.16}$$

where the x, y and z distances between the spatial collection points are given by Δx, Δy and Δz, the corresponding velocities are given by $|u_x|$, $|u_y|$ and $|u_z|$ and MIN_{Ω_f} refers to the minimum over the entire flow domain.

2.3 Turbulent kinetic energy transport equation

To understand the turbulent flow process, it is integral to understand the evolution of the turbulent kinetic energy. As DNS allows the flow fields to be decomposed by means of Reynolds decomposition, each term of the TKE equation can be computed for each time-step, at each location of the domain. Following the work done by [7] and using the notation of [17], the TKE equation is given by:

$$\frac{\partial \langle u_i u_k \rangle}{\partial t} + \langle U_j \rangle \frac{\partial \langle u_i u_k \rangle}{\partial x_j} = P_{ik} - \frac{\partial}{\partial x_j} T_{ijk} + \Pi_{ik} - \epsilon_{ik} \tag{2.17}$$

with the first term giving the time evolution of the Reynolds stresses, the section the convection of the Reynolds stresses. The Reynolds stress production tensor, P_{ik}, is defined as:

$$P_{ik} = -\langle u_i u_k \rangle \frac{\partial \langle U_i \rangle}{\partial x_j} - \langle u_i u_j \rangle \frac{\partial \langle U_k \rangle}{\partial x_j} \tag{2.18}$$

the Reynolds transport, T_{ijk}, is:

$$T_{ijk} = \langle u_i u_j u_k \rangle + \langle u_k p \rangle \delta_{ij} + \langle u_i p \rangle \delta_{kj} - \nu \frac{\partial \langle u_i u_k \rangle}{\partial x_j} \tag{2.19}$$

the pressure strain correlation, Π_{ik}, is given by:

$$\Pi_{ik} = \left\langle p \left(\frac{\partial u_i}{\partial x_k} + \frac{\partial u_k}{\partial x_i} \right) \right\rangle \tag{2.20}$$

and the dissipation, ϵ_{ik}, is:

$$\epsilon_{ik} = 2\nu \left\langle \frac{\partial u_i}{\partial u_j} \frac{\partial u_k}{\partial u_j} \right\rangle \tag{2.21}$$

Each of these terms can be calculated, during the simulation, in Nek5000 by using subroutines that was developed by [18]. Later sections will discuss the different terms for the TKE as they are calculated for the different cases, as presented in the introduction.

2.4 DNS requirements

In order to classify a numerical simulation as a DNS study, all length and time scales, for the specific turbulent flow, has to be resolved. The turbulence processes and the concept of energy cascades, as introduced by [17], showed that different sized eddies are present in the flow. The mean flow imparts TKE to the largest eddies, which has a length scale similar to the geometry, to smaller scales until the dissipation scale, which is the smallest length scale. In this scale, the energy is dissipated into unusable internal energy or heat.

The most widely accepted theory for the energy cascade process and the smallest possible scales in turbulence flow is that of Kolmogorov theory. This theory is based on three hypotheses. Firstly, the Kolmogorov similarity hypothesis [19] states that turbulent flows of high Reynolds numbers have a homogeneous and universal dissipative scale that is only determined by the fluid‘s kinematic viscosity, ν, and the dissipation, ϵ, of the energy. From this hypothesis, three Kolmogorov scales can be defined, namely length, velocity and time as:

$$\eta = \left(\frac{\nu^3}{\epsilon}\right)^{1/4} \tag{2.22}$$

$$u_\eta = (\nu\epsilon)^{1/4} \tag{2.23}$$

$$\tau_\eta = \left(\frac{\nu}{\epsilon}\right)^{1/2} \tag{2.24}$$

For a numerical simulation be to consider a direct numerical simulation these scales are the minimum criteria the discretization should adhere to. When the temporal and spacial discretization of

the numerical study is finer than that of the Kolmogorov time and length scales, all possible scales of motion can be fully captured by the the numerical simulation, thus classifying it as DNS.

To ensure that the simulations adhere to DNS requirements, these scales were calculated and compared to ensure conformance for each simulation and studied Reynolds number. These shall be discussed in the following chapters.

2.5 Proper orthogonal decomposition

One of the more powerful analytical tools to identify the energy content in turbulent flows, is the implementation of proper orthogonal decomposition (POD). POD allows the basis modal decomposition of turbulence, which is nearly infinite in dimensions, and capturing the dominant features with a drastically reduced number of representative modes.

With turbulence being such high dimensional phenomena, POD allows different applications and analysis of the results. The first application is to reconstruct the full set of governing NS equations by approximating it with a basis set of low-dimensional data. Representing a high-order system with low-dimensional approximation is termed reduced-order modeling. This method consists of a system of differential equations that is time integrated to determine the temporal coefficients. Combining these temporal coefficients with the spatial information contained within POD modes, analysis can approximate the dynamics and reconstruct the flow under investigation.

Due to POD highlighting the highest energy structure in the temporal flow, by decomposing the system optimally, it can be employed to investigate the underlying physical effects that drive the flow.

If the reader requires more theory on POD, they can consult [20] and the method of snapshots which is used to gather the data for POD [21]. How POD is implemented in Nek5000 can be found in [22] and it will be discussed next.

When investigating and determining a good representation a set of scalar fields $\{u^k\}$, where each field is a function of $u = u(x)$ and defined on the interval $0 \leq x \leq 1$, each function of u has to be decomposed and projected onto candidate basis functions. For this, it is assumed that all the functions belong to an inner product space, $L^2([0, 1])$, of square integrable functions, where the

inner product is defined as:

$$(f, g) = \int_0^1 f(x)d(x)dx \tag{2.25}$$

From this, the goal is to find a basis function, $\{\phi_j(x)\}_{j=0}^{\infty}$, for the space L^2, that the finite-dimensional representation in the form of

$$u_N(x) = \sum_{j=1}^{N} a_j \phi_j(x) \tag{2.26}$$

can describe the typical members of the data, better than any other basis can for the same dimension. This usually incorporates some form of averaging, which for our case will be time averaged over an ensemble consisting of $u^k(x) = u(x, t_k)$ members, taken from sequential time integration.

When the square space, L^2, is to be taken as a more general Hilbert space $\mathcal{H}$, the best condition of selecting the basis function, implies that the normalized averaged projection of u onto ϕ should be maximized,

$$max\left\{ \phi \in \mathcal{H} \frac{\left\langle (u, \phi)^2 \right\rangle}{||\phi||^2} \right\} \tag{2.27}$$

Calculus of variations are used to solve the problem by generating an eigenvalue problem of the following form:

$$\mathcal{K}\phi = \lambda\phi \tag{2.28}$$

The optimal basis functions are thus given by the eigenfunctions $\{\phi^j\}$ of the the $\mathcal{K}$ operator, that is defined by the computational data, also termed the POD modes.

When expanding Eq. 2.28, the equation becomes

$$\begin{aligned}\mathcal{K}\phi(x) &= \int_{\Omega} K(x,x')\phi(x')d(x') \\ &= \lambda\phi(x)\end{aligned} \tag{2.29}$$

where the kernel $K(x,x') = \langle u(x,t)u(x',t)\rangle$, and a dyadic product is implied for the vector multiplication. When the finite dimensional domain with the Hilbert domain $\mathcal{H} = \mathbb{R}^N$ is considered, with the simulation data coming from a set of M vectors $u^k \in \mathbb{R}^N$, and the arithmetic mean is given by $\langle\ .\ \rangle$. From this the Kernel may be given as:

$$\mathcal{K}_{ij} = \frac{1}{M}\sum_{k=1}^{M} u_i^k u_j^k \tag{2.30}$$

From this definition, the Kernel $\mathcal{K}$, is a real, symmetric $N \times N$ matrix and Eq. 2.28 is a standard matrix eigenvalue problem in $\mathbb{R}^N$. For DNS, the number of grid points N, can be quite substantial. Due to the size of DNS data, solving the eigenvalue problem becomes impractical due to the size of the matrix. This is the reason we convert to the method of snapshots to solve the $M \times M$ problem.

When the method of snapshots is used, a collection of M vectors are used to generate the kernel in Eq. 2.30. This is formed from a series of linearly independent flow realizations that is sequentially taken during the time integration of the turbulence case. If the vector $\{u^i\}_{i=1}^M$ is taken as the realization of the flow field and $(.,.)$ is the inner product of the N-dimensional vector space. The discrete version of the inner product $L^2(\Omega)$ allows the eigenfunctions to be written as:

$$\phi = \sum_{k=1}^{M} a_k u^k \tag{2.31}$$

Where the coefficients a_k have to be computed. Combining Eq. 2.30, the eigenvalue problem of

Eq. 2.28 can be given as:

$$\left(\frac{1}{M}\sum_{i=1}^{M} u^i (u_i)^T\right) \sum_{k=1}^{M} a_k u^k = \lambda \sum_{k=1}^{M} a_k u^k \tag{2.32}$$

We can simplify the left hand side of the equation to:

$$\sum_{i=1}^{M} \left[\sum_{i=k}^{M} \frac{1}{M}(u^k, u^i) a_k\right] u_i \tag{2.33}$$

the basis function is to find a solution for the coefficients a_k, so that

$$\sum_{i=1}^{M} \frac{1}{M}(u^k, u^i) a_k = \lambda a_i, i \in (1, M) \tag{2.34}$$

The $M \times M$ eigenvalue problem solved in Nek5000 takes this form to compute and compare the POD modes for the different flow cases.

2.6 Summary

The required mathematical theories that form the base of this study was detailed in this section. This includes the relevant conservation, the equations for turbulent kinetic energy transport, the basis of Nek5000‘s spectral element methods and the discretization requirements for DNS. The following sections will cover the initial study, meshing strategy and experimental comparisons to validate the modeling assumptions made.

3. NUMERICAL EXPERIMENT I: TWO SPHERES WITH DIFFERENT SPACING

This section acts as a continuation of the work done by [1] where it was found that the addition of another sphere affected the temporal dynamics of flow over a sphere. The exact effect of the pebble placement was not investigated. Within random packed pebble beds, the complex geometry allows for pebbles with different spacings, with potential endless underlying effects coming into play. In order to isolate the effect of the pebble spacings 4 different idealized spacings where simulated and compared. This was done to try and find a better understating on the different simultaneous temporal effects that is present within a randomly unstructured pebble bed.

The section kicks off with a brief introduction and verification of the modeling done, for flow over conical bluff bodies. The justification and previous work done, on a single sphere, can be found in [1]. The methodology and modeling approaches for the 4 cases are then given. Followed by the results and comparison between the 4 cases for the most important results. The section is then ended by the conclusions drawn from the study.

3.1 Background

Numerous engineering and research areas require the understandings about incompressible flow over bluff bodies. From fundamental fluid dynamics research, to high-temperature nuclear reactors have some form of fluid flow over spherical components.

The complexity and computational burden of extracting high fidelity DNS results from actual engineering systems have left fundamental research the only sector that can utilize the power and accuracy of DNS. This results that the majority of high fidelity DNS results only covers flows oversimplified single spheres, in a free stream with little to no experimental data for verification or validation. Examples of where DNS have been incorporated is that of low Reynolds Number flows, especially pertaining to the transition region [23]. These simulations‘ main focus was the representation and visualization of the first- and second order turbulence statistics of the wake region [24, 25].

More recent work has been done by [26, 27, 26, 28] on an idealized, fully structured case. This research focused on the temporal dynamics of the flow while still keeping the geometry fairly simple. This does approximate the actual geometry better, but the random packing structure can introduce even more temporal dynamics.

From a numerical simulation perspective, most practical flows over spherical bodies, as in that of gas-cooled nuclear reactors, has been Reynolds averaged Navier-Stokes (RANS) or hybrid-RANS approaches, as done in [29, 30, 31]. All these were done on idealized structured cases, mostly iso-thermal, to quantify the effects of contact treatment and turbulence statistics. With the numerical and modeling uncertainties associated with these modeling approaches, the answers have to be validated by either DNS or experimental data.

For this work, $four$ different pebbles spacings were investigated: $1.5D$, $2.0D$, $2.5D$ and $3.0D$. This was to support DNS verification data and continue work published by [1]. This will also finally serve as a baseline for PIV results on random pebble beds, done by [32]. For these cases the Reynolds number of 1000 was used.

The verification of flow over a single sphere was done by [1] as well as 2 spheres with a $2.0D$ spacing. The comparisons of the other spacing of first and second order turbulence statistics are given.

3.2 Methodology

The outlines for the case, with the associated geometric, flow and computational parameters used is given in this subsection.

3.2.1 Case Outline

The general geometry used for this study is that of two tandem spheres within a free stream, as seen in Figure 3.1a. The mesh was generated by using ICEM-CFD's block meshing tools after which the mesh was converted using the native Nek5000 tool, exo2nek. The mesh consists of a rectangular box ranging from $[-5D \leq x, z \leq 5D]$ and $[-5D \leq y \leq -25D]$. Within this box, a spherical to rectangular o-grid transition conforms to the sphere surface. Where the pebble

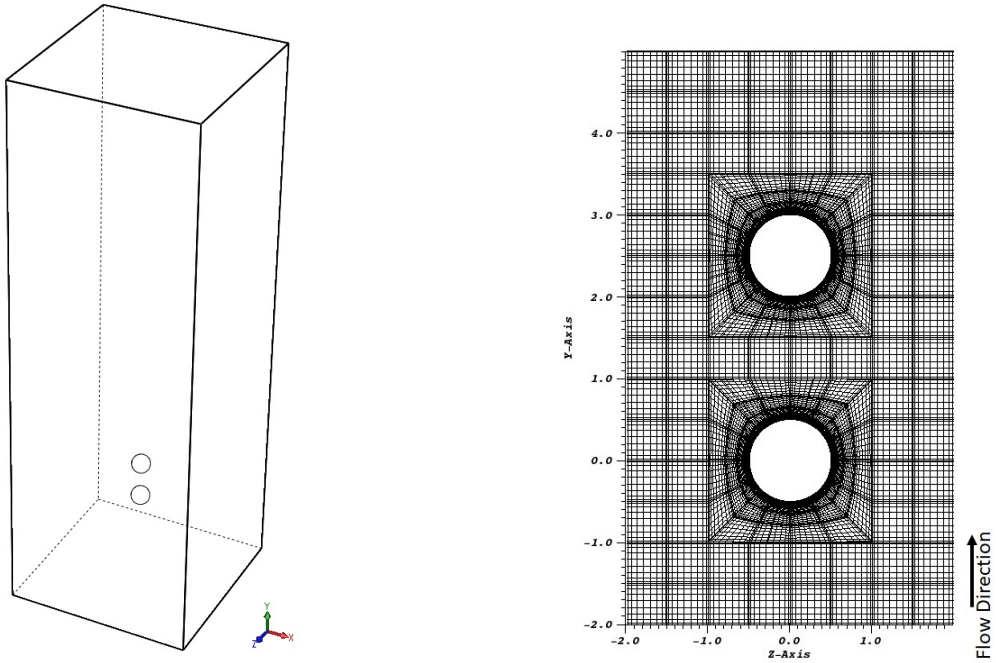

(a) An isometric view of the total domain with a spacing of 2.0D.

(b) A slice view of the mesh at x=0.

Figure 3.1: Visual representation of the geometry and mesh.

diameter is defined as $D = 1$. Four different pebble spacings where simulated, the center to center distances set as $1.5D$, $2.0D$, $2.5D$ and $3.0D$. The pebble spacings and blocking was chosen, so that the pebbles can be moved without changing the element count of the domain. This resulted in a mesh of 31025 elements for all 4 cases.

All the flow and boundary conditions were kept consistent for all the cases. No-slip wall conditions were applied to the sphere surfaces, while all other boundaries received a uniform constant stream wise velocity of $U_y = 1$. The outlet top surface was treaded as a pressure outflow boundary. The simulation was set up with a Reynolds number of a 1000 to match the conditions of [1] and the experimental [23].

3.2.2 Computational Parameters

The free stream velocity, $U_\infty = 1$, and the pebble diameter $D = 1$ was used to define the Reynolds number. Assigning a unit density to the fluid, allows the Reynolds number to be defined

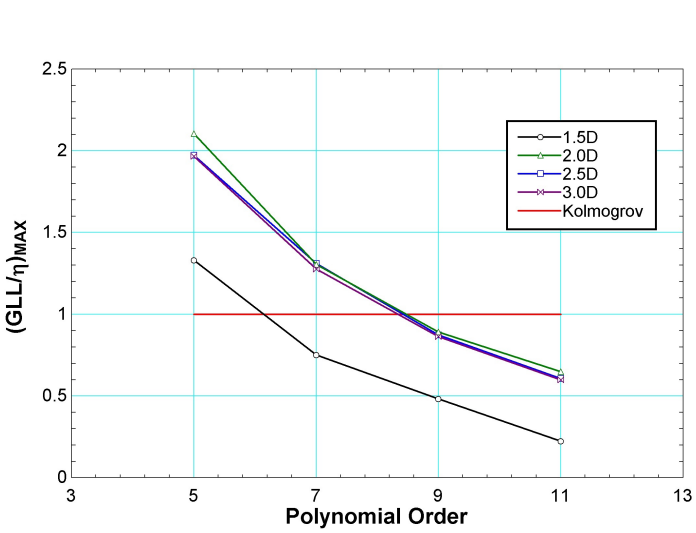

(a) Maximum grid spacing to Kolmogorov ratio vs polynomial order.

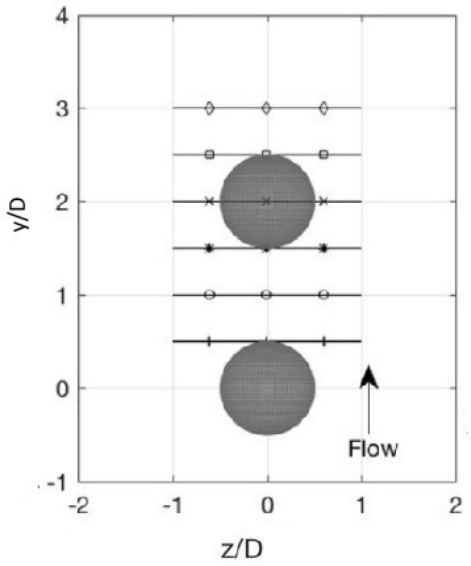

(b) Line profile locations for interpolation.

Figure 3.2: Visual representation of the Kolmogorov calculations.

as $Re = 1/\mu$. To investigate the influence of the pebble spacing on the flow the Reynolds number was chosen to match that done in previous work and proposed experimental conditions. The verification and defense of the choice in Reynolds number was done by [1], if required the reader can consult the previous work done.

To ensure that DNS requirements are met for all 4 cases the Kolmogorov scales were calculated. The ratio of the local grid size to length scale was calculated for a set period of time and the global maximum was plotted as a function of polynomial order, Figure 3.2a, for all 4 cases. From this, a polynomial order of $N = 9$ was used for production runs for all the cases.

Work done by [33, 34] showed that for cylinders in tandem, there exists a critical spacing where wake separation is only seen from the front cylinder. [1] showed that for a single sphere Kelvin-Helmholtz instabilities existed. With the different spacings, one would expect to see a spacing where the vorticity closely resembles that on a single sphere and as the spacing increases the second sphere‘s influence would become visible.

The Argonne Leadership Computing Facility IBM Blue Gene/Q clusters located at Argonne

National Laboratory, was used to run these cases. The flow was developed for 200 convective units ($CU = D/U_\infty$) at a lower polynomial order of $N = 5$. This allowed for rapid time stepping of the cases. After development, the production runs were commenced. The flow was averaged for $800CUs$ after the flow has been developed, with a time step of 4×10^{-3}. The simulation utilized 16384 CPU cores to solve the flow field over 22.618×10^6 collection points.

3.3 Results and Discussion

The results obtained form the 4 numerical experiments are given in the following sub-section.

3.3.1 First and second order statistics

The statistics of this subsection was averaged after the simulation has reached a statistical steady state. Due to the symmetry of singular spherical bluff bodies, a common practice for numerical experiments, are to average interpolated line profiles azimuthally around the axial centerline. This azimuthal averaging is established to produce well-averaged statistics. This is supposed to hold up, because the statistics develop to a time-invariant azimuthal symmetric condition. In work done by [35] there was found that a low-frequency switching of the azimuthal location occurred in complex spherical geometries. As found by [1] there also exists the same, low-frequency shifting in the simplified two sphere case.

Based on the fact that azimuthal averaging cannot be implemented for the two-sphere case the longer integration period was required to obtained well-resolved statistics, as found by [1, 25, 24]. The $2.0D$ simulation was run and compared to that of [1] and it was found averaging over 800 CUs produced the same results.

Figure 3.3 shows the averaged streamwise velocity at the $[0, y, z]$ plane, all plotted over the same minimum and maximum value for better comparisons. The averaged velocity field of a single sphere was found to be symmetrical. Here it can be seen that for all 4 cases a fairly symmetric wake region is also observed downstream of the downstream sphere, as in [1]. When inspecting $\langle U_y \rangle$ in the gap region they profile does not present a symmetric profile. It is also seen that the flow switch the direction it is biased towards, indicating the pebble placement has an influence on

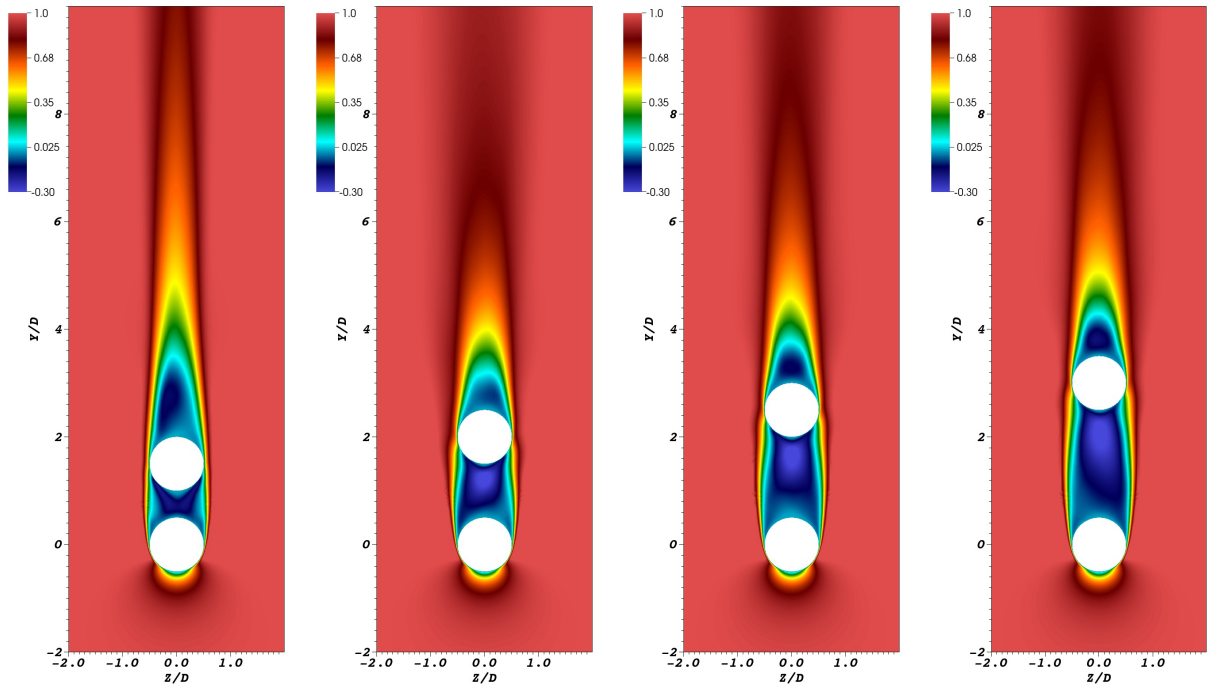

(a) 1.5D (b) 2.0D (c) 2.5D (d) 3.0D

Figure 3.3: Pseudo-color field of the averaged stream wise velocity, $\langle U_y \rangle$, for the 4 sphere spacings.

this. Figure 3.3a seems to be fairly symmetric, as the downstream pebble distance is increased the recirculation region, $\langle U_y \rangle \leq 0$, is biased towards $z/D \leq 0$. As the distance increases the biasness decreases to almost symmetry before it switches to $z/D \geq 0$ for the last spacing. This indicates that a critical pebble spacing occurs, as in that of tandem cylinders observed by [34].

The representation of the Reynolds stress tensor is simplified, due to the choice of unity for the fluid density. This results in the Reynolds stress tensor being represented by the single-point, single-time covariance tensor, $\langle u_i u_j \rangle$. Figure 3.4 shows the in-plane $\langle u_y u_y \rangle$ component of the Reynolds stress tensor for the $four$ spacings. Not only can the same asymmetry be seen in the four cases, but also a significant change in magnitude and biasness as the gap distance is increased. This is observed even after the statistics have reached a stationary state. It can be seen for the smallest gap, the Reynolds stresses are significantly lower and there is no localized maximum in the gap region. Then as the gap increases the maximum is biased towards $z/D \leq 0$ for $2.0D$. A further increase results in an almost symmetric stress tensor in Figure 3.4c, before finally the

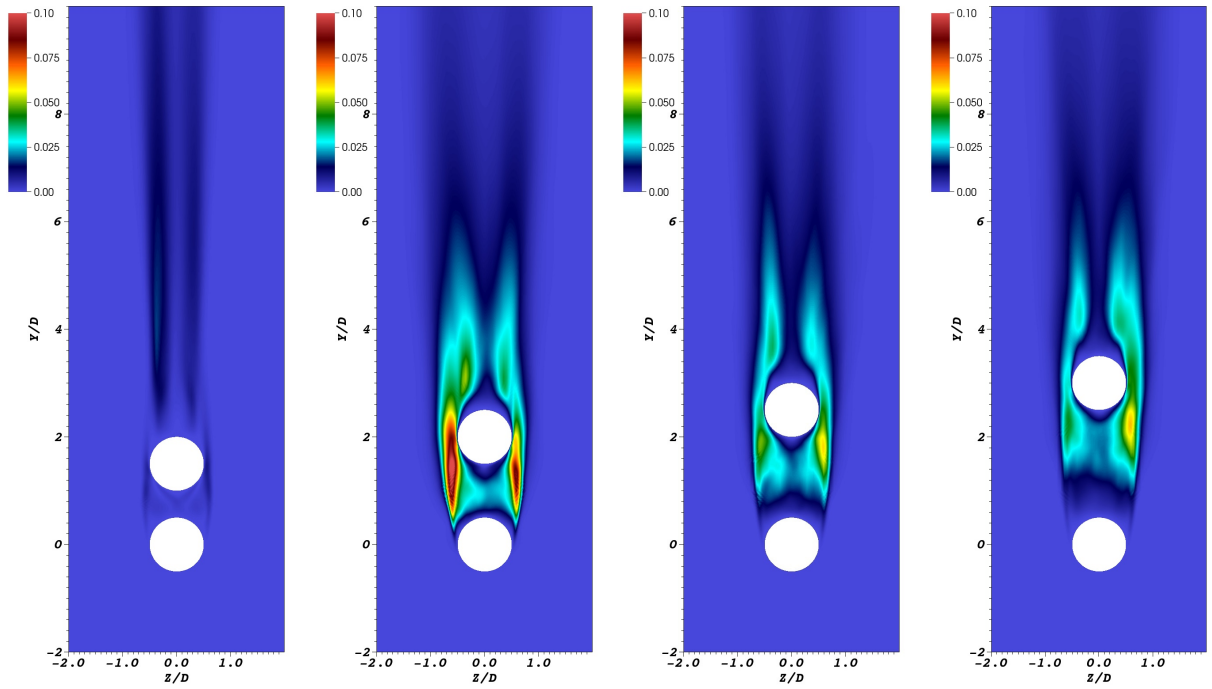

(a) 1.5D (b) 2.0D (c) 2.5D (d) 3.0D

Figure 3.4: Pseudo-color field of the in-plane Reynolds stress component, $\langle u_y u_y \rangle$, for the 4 sphere spacings.

maximum shifts to $z/D \geq 0$, but to magnitude decreases as the spacing is increased. This verifies the existence of a critical sphere placement around $1.5D$ and again around $2.4D$.

Figure 3.2b shows the interpolation line positions for each case.

Figure 3.5 is the interpolated line profiles $\langle u_y u_y \rangle$ in the near wake region for the four spacings. The lines were constructed from 100 equally spaced individual points. Figure 3.5a is situated at $Z/D = 0.5$ and each consecutive line's Z/D position is increased with $0.5D$. To ensure that the results from all $four$ cases could be compared, the data was normalized for each line by using the absolute maximum value for each line over all four spacings.

$$X_{norm} = max(max(|X_{ij}|)_{i=1,100})_{j=1,4} \tag{3.1}$$

Where X is the normalized variable. This normalization allows the comparison and represen-

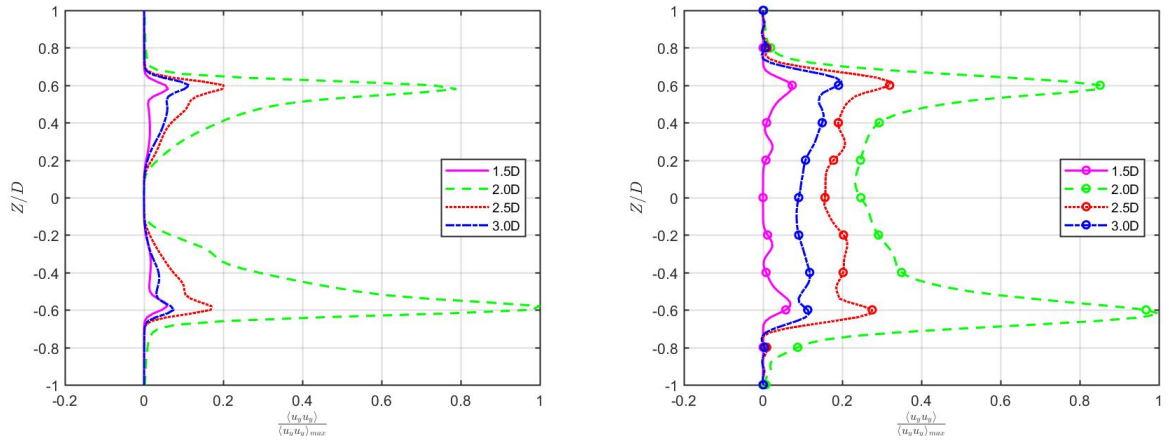

(a) Y/D = 0.5

(b) Y/D = 1.0

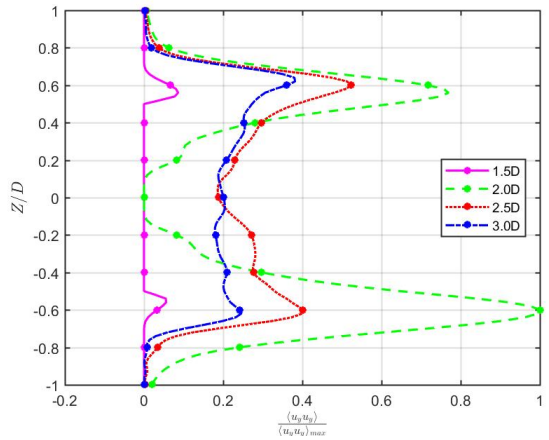

(c) Y/D = 1.5

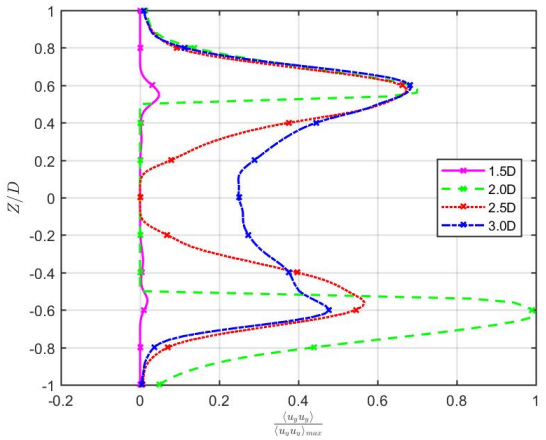

(d) Y/D = 2.0

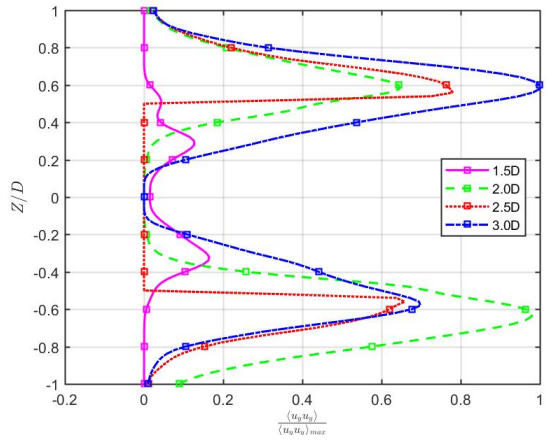

(e) Y/D = 2.5

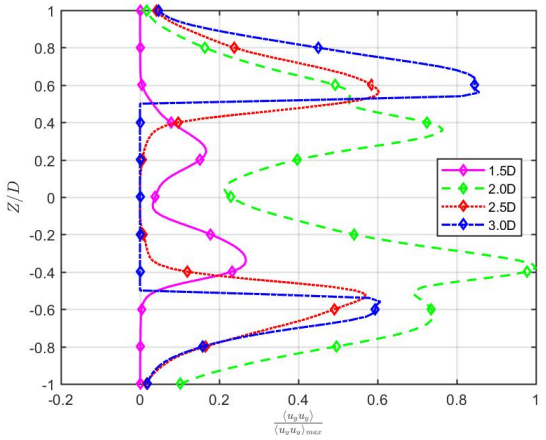

(f) Y/D = 3.0

Figure 3.5: Line profiles of $\langle u_y u_y \rangle$ in the wake region of two spheres. All the lines are normalized using the largest absolute value obtained from the six lines over the 4 spacings.

tation of the data between the four different cases as well as how the relative magnitudes for each case at the current position.

When looking at the first line, it is seen that $\langle u_y u_y \rangle$ starts as a narrowly peaked profile with $2.0D$ clearly having the largest magnitude. And having a slight asymmetry towards $Z/D \leq 0$. As we move downstream to $Y/D = 1.0$, the relative magnitudes of spacing $1.5D$, $2.5D$ and $3.0D$ start to increase. For $1.5D$ the profile still have a fairly symmetric profile at this point. $2.0D$ shows the maximum being biased towards $Z/D \leq 0$, where the last two cases are biased towards $Z/D \geq 0$.

At $Y/D = 1.5$ the magnitudes of $2.5D$ and 3.0 increases even furtherer and the profile become broader. For $1.5D$ no significant change is observed. It seems like the downstream pebble is in the slipstream of the first sphere and the flow is dumped behind the downstream pebble, resulting in little to no recirculation of the closest spacing.

Moving further downstream to $Y/D = 2.0$ it is seen that the profile of $1.5D$ decreases. This line is at the back of the downstream pebble, this is the smallest Reynolds stress region between the 4 cases. For the $2.5D$ the profile is moving away from the broad shape and it is taking on a more narrow peak profile. $3.0D$ still exhibit the narrow peak profile, where the peak is biased towards $Z/D \geq 0$.

For the lines at $Y/D = 2.5$ it is interesting to see that case $3.0D$ and $2.0D$ have equal maxims, but the maximum‘s location has switched. These profiles are almost mirror images of one another. Case $1.50D$‘s stresses are still at least an order magnitude smaller than that of the others.

At the last line, $Y/D = 3.0$ the stresses seem to be all of relative equal values, except for the smallest gap. Case $2.0D$ shows an interesting development, where the profile exhibit two less dominant peaks. The profile is also broadening as we are in the wake of the downstream sphere.

From the presented statistics, it is evident that the spacing of the second sphere not only influences the magnitude but as well as the symmetry of the observed nominally steady solution.

3.3.2 Turbulent kinetic energy

This subsection will present some of the selected components of the turbulence kinetic energy transport equation. Production and dissipation tensors where chosen to be presented.

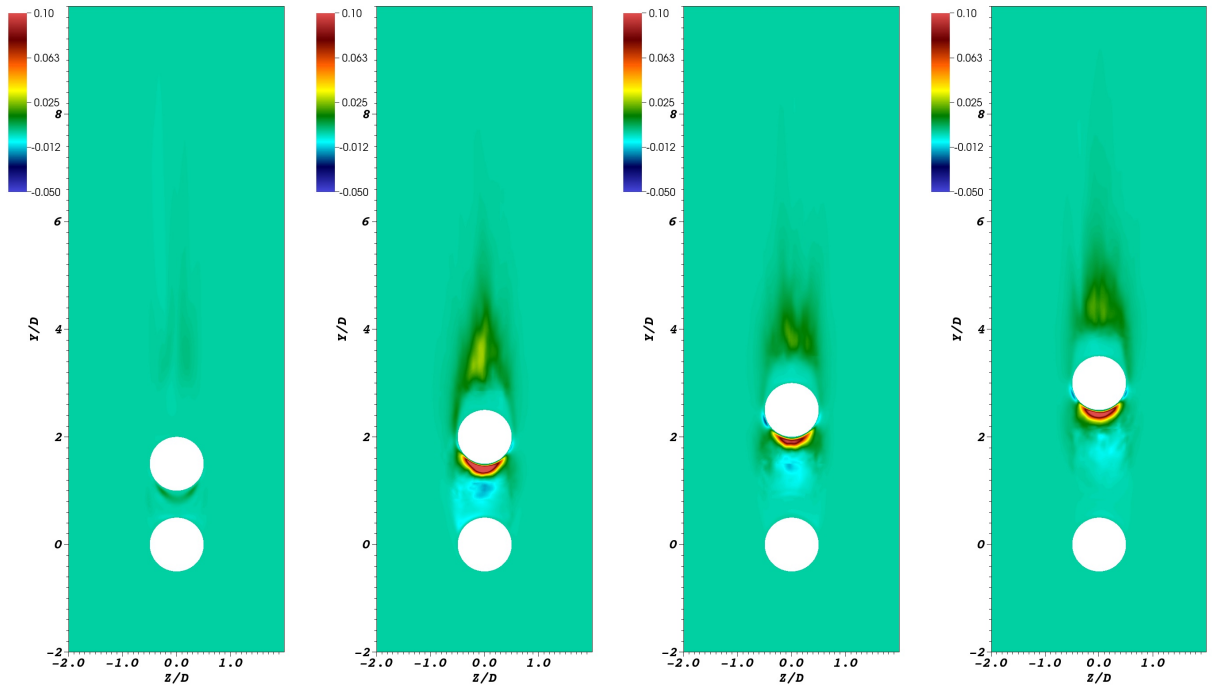

(a) 1.5D (b) 2.0D (c) 2.5D (d) 3.0D

Figure 3.6: Pseudo-color field of the diagonal component of the turbulent kinetic energy production tensor, in the span wise direction P_{xx}, in the [0, y, z] plane.

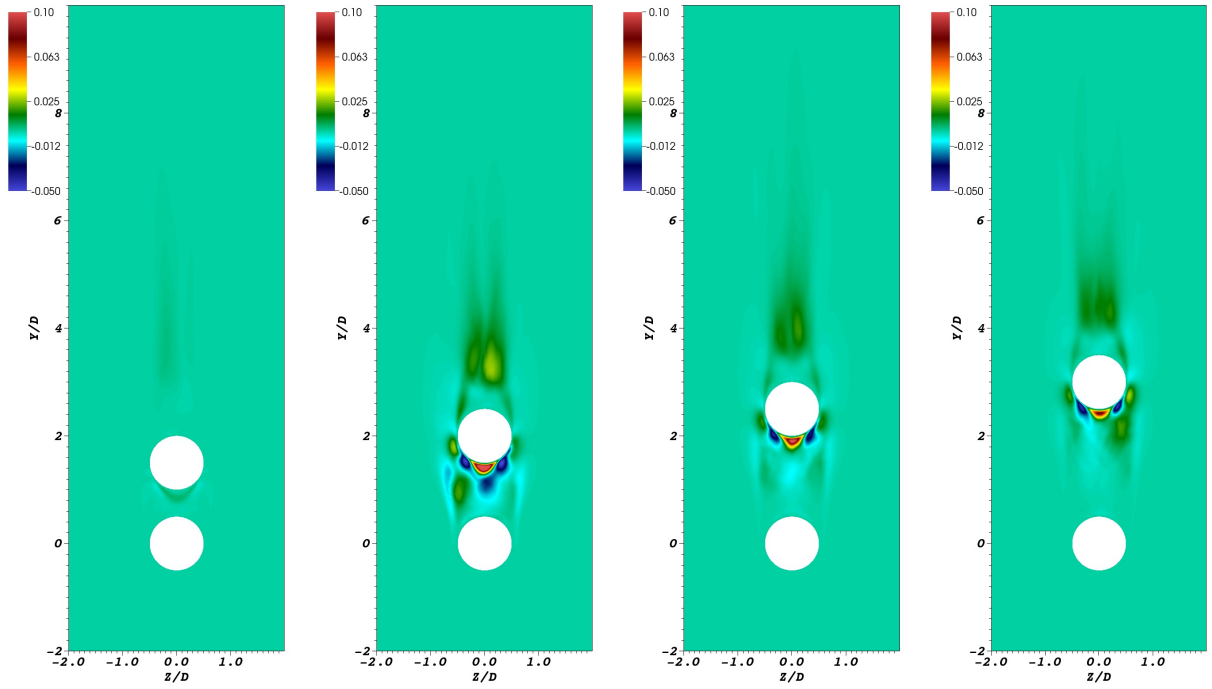

(a) 1.5D (b) 2.0D (c) 2.5D (d) 3.0D

Figure 3.7: Pseudo-color field of the diagonal component of the turbulent kinetic energy production tensor, in the stream wise direction P_{zz}, in the [0, y, z] plane.

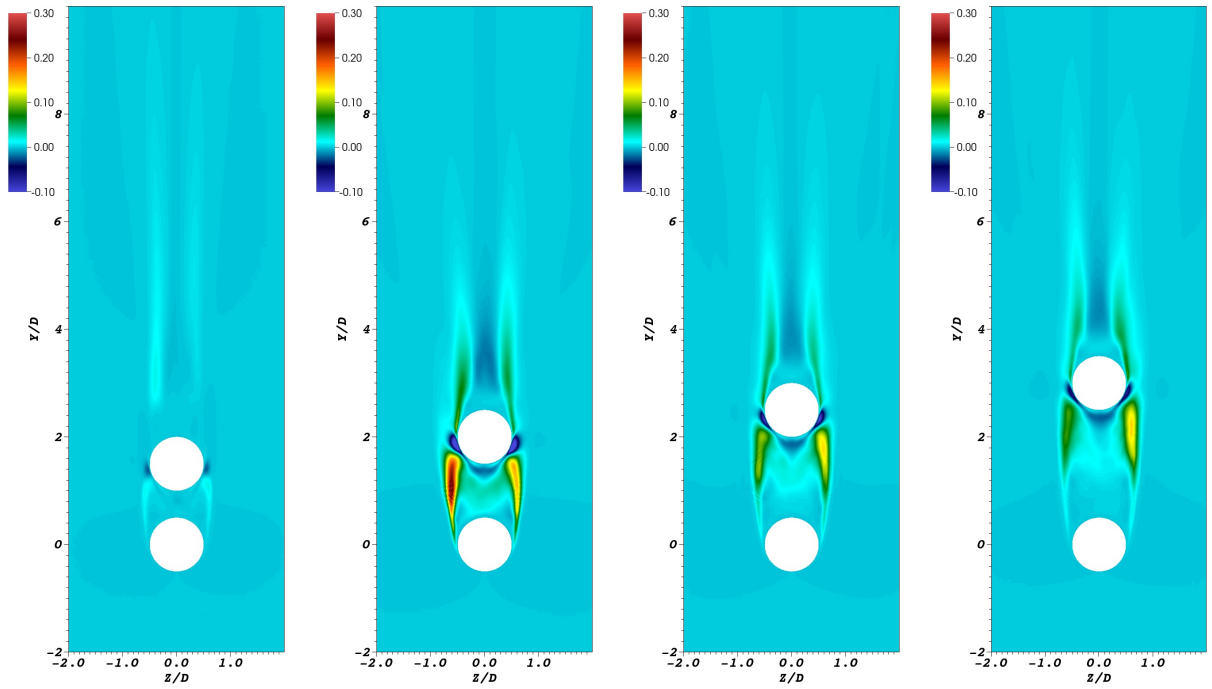

(a) 1.5D (b) 2.0D (c) 2.5D (d) 3.0D

Figure 3.8: Pseudo-color field of the diagonal component of the turbulent kinetic energy production tensor, in the stream wise direction P_{yy}, in the [0, y, z] plane.

When looking at the structures and magnitudes of the lateral components, P_{xx} and P_{zz}, Figures 3.6 and 3.7, it is seen they present similar magnitudes and structures, except for the $1.5D$ case. It clear that there is little to no production in the recirculation region, indicating that the downstream pebble is in the slipstream of the first and the generate wake is produced by the first pebble being shed behind the downstream sphere. From the other three cases, the maximum and position shows were the shear-layer Kelvin-Helmholtz instability manifests on the periphery of the recirculation region. the highest lateral production is found in the recirculation region of the $2.0D$ case.

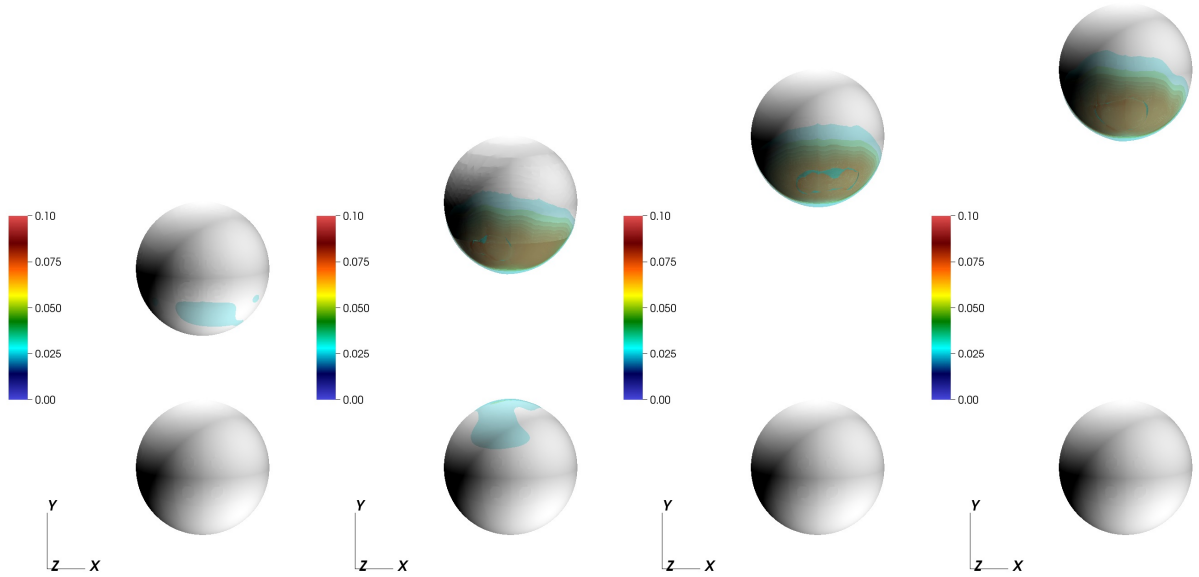

(a) 1.5D (b) 2.0D (c) 2.5D (d) 3.0D

Figure 3.9: Volume rendering of the span wise diagonal components of the turbulent kinetic energy dissipation tensor,P_{xx}, in the [0, y, z] plane.

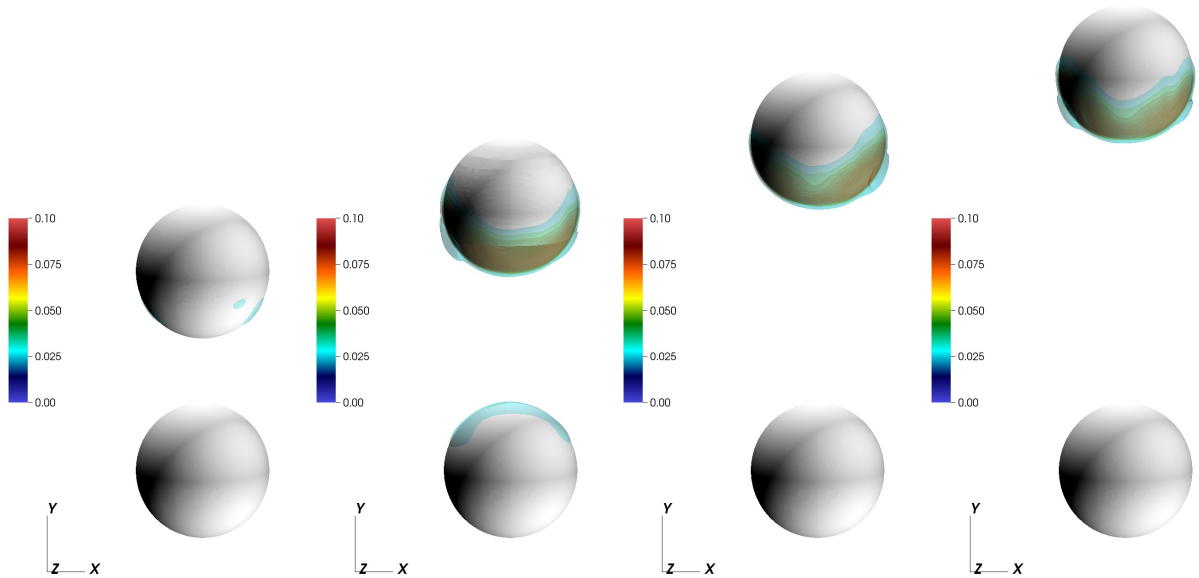

(a) 1.5D (b) 2.0D (c) 2.5D (d) 3.0D

Figure 3.10: Volume rendering of the span wise diagonal components of the turbulent kinetic energy dissipation tensor,P_{zz}, in the [0, y, z] plane.

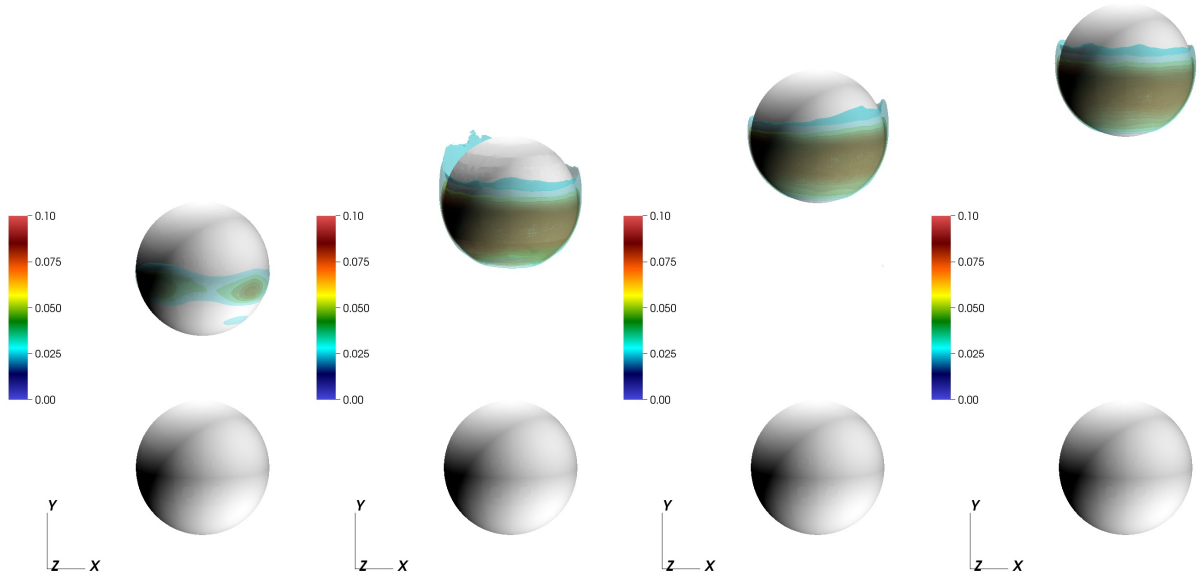

(a) 1.5D (b) 2.0D (c) 2.5D (d) 3.0D

Figure 3.11: Volume rendering of the stream wise diagonal components of the turbulent kinetic energy dissipation tensor,P_{yy}, in the [0, y, z] plane.

Looking at the streamwise production P_{yy} in Figure 3.8, negative non-zero production originates at the sphere surface where the wake separates from the sphere. For the $1.5D$ case, it is seen that the production almost engulfs the downstream sphere, where for the other cases the production is dumped before. There is also a clear asymmetry in the production of turbulent kinetic energy in the cases with larger spacings. The switch in maximum is also seen from $Z/D \leq 0$ in $2.0D$ to $Z/D \geq 0$ in $2.5D$ indication in the existence of a transition region. This is consistent with the velocity and Reynold stresses discussed in the previous section.

When investigating the dissipation of turbulent kinetic energy for the four cases, it is seen that the maxima are concentrated on the surface of the downstream sphere. In order to better visualize the dissipation of turbulent kinetic energy, volume renderings were used to represent the structures. With the $1.5D$ case, very little dissipation can be seen, this is coupled to the fact that the production for this case is also much lower than the others. When looking at the structure of the spanwise dissipation, it seems like to structure is rotated 90° degrees.

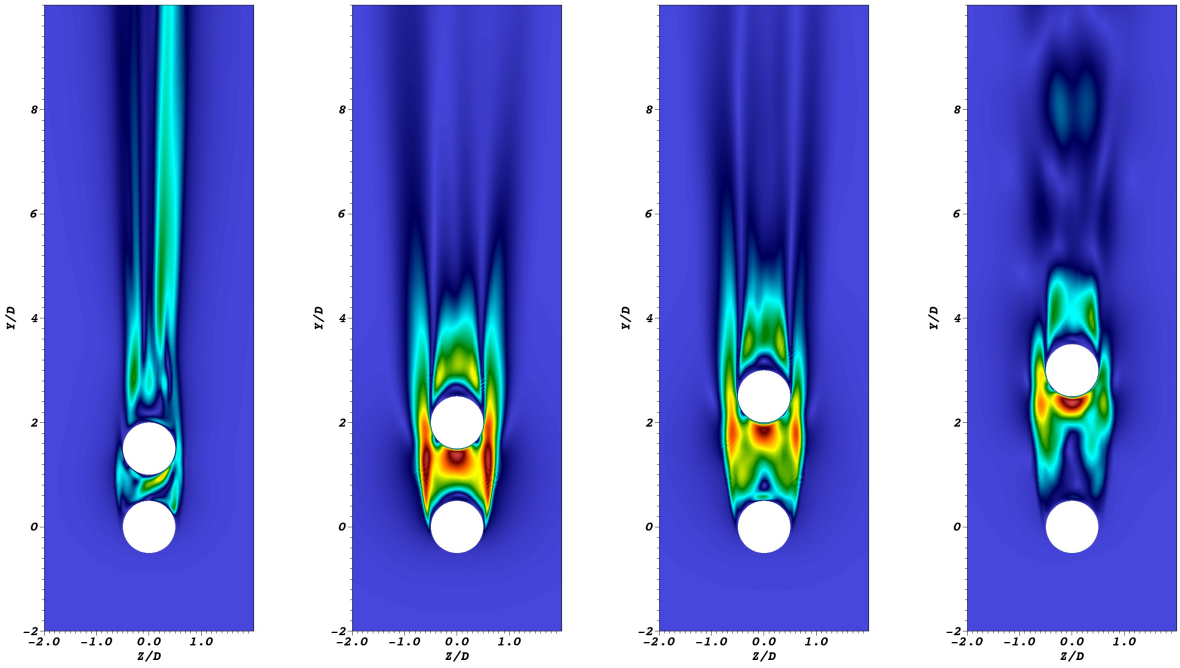

(a) 1.5D (b) 2.0D (c) 2.5D (d) 3.0D

Figure 3.12: Pseudo-color field of the highest energy POD eigenfunctions in the [0, y, z] plane.

For the streamwise dissipation, Figure 3.11, the $1.5D$ case exhibit a band of dissipation on the equator of the downstream sphere, corresponding to the fact there is little to no recirculation happening in the gap between these two spheres. Then investigating the other three cases, a symmetric even distribution is seen on the upstream surface of the downstream sphere.

3.3.3 Proper orthogonal decomposition

Applying proper orthogonal decomposition to the flow field allows the isolation of the underlying coherent structures within the turbulent flow. These structures are separated into spatial variables which contain the highest energy. For turbulent flows, the spatial variables under consideration is that of the turbulent kinetic energy. The method of snapshots and the algorithm used for the POD analysis in Nek5000, and the details can be found in [22].

For the cases under consideration, 3000 instantaneous flow fields snapshots were taken, every $0.2\ CU$, resulting in a total of $600\ CU$ or $20\ FFT$. [1] stated that due to the low Reynolds number the turbulent kinetic energy at higher wave numbers are neglectable and the snapshots

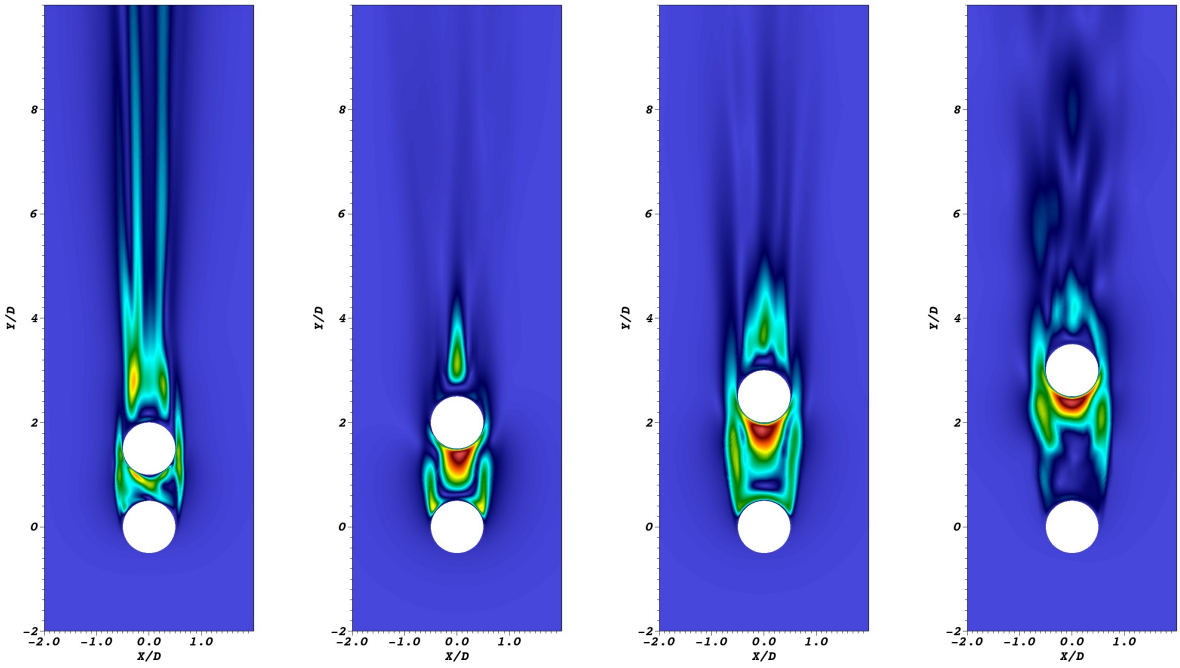

(a) 1.5D (b) 2.0D (c) 2.5D (d) 3.0D

Figure 3.13: Pseudo-color field of the highest energy POD eigenfunctions in the [x, y, 0] plane.

were sufficient. To ensure this the snapshot frequency was doubled to ensure all the relevant wavenumber are captured in the POD modes. If the assumption made was correct the POD modes for the $2.0D$ case should be equal to that of [1] in both planes.

Fig. 3.13 and 3.12 shows the magnitude of the most energetic POD eigenfunction for the four cases, in the $[0, y, z]$ and $[x, y, 0]$ planes respectively. [35] showed that for a single sphere the coherent cyclic structures are found in the wake of a single sphere. It was also found that adding a second sphere at $2.0D$ that the concentration of the structures is changed.

Inspecting Fig. 3.12b and 3.13b the similarity in the $[0, y, z]$ plane is evident to that of [1]. For the $[x, 0, z]$ plane, the general structure of the first POD mode does resemble that found in the previous work, but less energy is contained around the downstream sphere‘s wake region. This can be that the higher snapshots frequency captured higher frequencies that contained energy, that was missed in the previous assumption.

When decreasing the spacing to $1.5D$, in Fig.3.12a and 3.13a, it is seen that the highest mode of

energy is mostly concentrated in the wake of the downstream sphere. The structures are elongated tubular in form with a small asymmetric concentration on the downstream surface of the second sphere. This follows the trend of the Reynolds stress being much lower for this case than the other 3 spacings, indicating some form of critical sphere separation distance exists. The structure does not resemble that of a single sphere, not that of the larger spacings. This highlights the different flow physics that will come into play when investigating the fully random packing geometry in the next chapter.

Fig. 3.12c and 3.12c see relatively the same structure as in the $2.0D$ case, with slightly lower magnitude and the highest concentration upstream of the downstream pebble. In Fig. 3.12c the appearance of a small concentration of energy appearing on the downstream surface of the first sphere along with a small symmetrical profile. For Fig. 3.13c the profile emanating from the first sphere surface extends past the downstream sphere, and is biased towards $x \leq 0$. The concentration of energy occurring on the downstream sphere‘s surface seems to flatten out a bit.

Fig. 3.12d and 3.12d more asymmetry comes into view for both the up and downstream sphere. The higher energy modes separate from the upstream pebble and the cyclic structures, seen in the single sphere case of [1], start to become visible downstream of the second sphere. The concentration of the maximum on the downstream surface of the second sphere is flatter than that seen in the previous two cases.

3.4 Conclusions

In this section the incompressible flow, with a Reynolds = 1000, over two spheres with different spacings where given and discussed. The work was a continuation of work done by [1], where the verification and validation were done for a single sphere. The results here obtained was verified with those found in his work for a spacing of $2.0D$

The work done here can serve as an introduction to randomly packed pebble bed work. From the results the influence of the downstream pebble spacing on the temporal dynamics of the system was evident. The results show not only does the spacing influence the asymmetry of the solution, but also the magnitude, even for long time ingratiation periods. These results shall be used to

define the randomly packed experimental setup, with similar Reynolds numbers.

There was found that a critical sphere spacing exists where separation form the downstream sphere is not observed, due to the close proximity. This resulted in little to no turbulent kinetic energy production and recirculation in the gap between the spheres, with a small spacing. A spacing where the maximum production and asymmetry occurs was observed. When the spacing is increased even further the asymmetry switches side and the maximum decreases. From these results it is clear that when the random packed pebble bed is observed a complex combination of different flow phenomena shall be present.

The POD analysis of the turbulent flow showed the coherent structures that are present in the flow. This discussion illustrated the qualitative difference of the highest energy modes in the flow to one another. The spacing of the spheres had a clear influence on the vortex street that was observed for the four cases.

The continuation of the work shall focus on a randomly packed experimental setup, where the interpretation of the results shall draw from the two pebble case.

4. NUMERICAL EXPERIMENT II: EXPERIMENTAL RANDOM PACKED PEBBLE BED

The following section presents the results obtained from the randomly packed geometry, which was obtained from the experimental setup. This study was done in parallel to that of the different spacing cases. To see if the same structures could be observed in the random case.

The layout of this section will start will a background stating the importance of the problem, followed by a case outline. The newly adaptive meshing strategy will be discussed and the location of the interpolation lines. How the simulation was simplified in order to mesh the random geometry is discussed and then determining the adequate discretization and statistical stationarity is discussed. The study is concluded by comparing the results obtained from the experiment to see how minor geometric differences and inaccuracies affected the flow.

4.1 Background

The Generation IV International Forum has selected the veryihigh-temperature reactor (VHTR) as one of the reactor concepts that have the potential to replace the current generation of rectors, due to the safety and versatility the reactors posses. These safety and efficiency features, along with the different VHTR designs can be found in [4, 5].

The PBR, a sub-class of the VHTR, can have either a cylindrical or annular core, with hundreds of thousands of fuel spheres, embedded with TRISO particles, randomly distributed within the core. Some of the designs feature an on-line refueling system where spheres are extracted from the bottom, tested for burn-up and reinserted at the top if required. The alternative is a more conventional off-line refueling approach that can be used. For both of these cases, the core does not have a structured packing and is completely random.

Depending on the primary coolant loop, inert gas or molten salt, a PBR can have secondary and tertiary power conversion cycles. These cycles can provide thermal energy for chemical processes such as hydrogen production, or employ Rankine or Brayton cycles, or a combination to produce power and/or process heat. This versatilely of the PBR makes it such a good candidate to replace

the current nuclear fleet.

In order to license and design a nuclear reactor, a thorough understanding of the fluid flow and flow phenomena through the core is critical. As stated, each core is essentially unique due to the random packing and or the fuel loading process. Unlike Gen II and III reactors where the core is structured with identical fuel assemblies, PBR cores only consist of spheres. This randomness coupled with the high curvature of the complex geometry makes PBR cores some of the most complex flow geometries to simulate. This complexity coupled with the size of these cores has hampered, not only computational studies [12], but also experiments [36]. Due to this, heuristic approaches had been utilized that developed empirical correlations form macro-scale data. These correlations [37] are of importance for engineers to calculate parameters such as pressure and temperature distributions throughout the core. Some of these correlations are frequently referenced [37] when determining the accuracy of the large scale results obtained from CFD tools.

With regulatory framework becoming more stringent and focused on reactor safety, more emphasis has been placed on detailed analysis of the flow physics. Current correlations and frameworks, might be insufficient to capture the complex flow phenomena in these new reactor designs, as they only focus on large-scale effects. Due to the increase of computational capabilities over the last few years and using CFD as a research tool, more and more detailed studies of these geometries has been made. Current CFD tools are able to cover all the entire range of scales that are present within PBR systems, from one-dimensional full system [36], to high detail three-dimensional CFD simulations have been conducted at pebble scale [38].

Numerous challenges have to be overcome to simulate pebble bed flows with CFD. The size coupled with the large degree of curvature introduced by the spheres causes bluff body effects such as flow separation and reattachment. RANS based turbulence models, the method usually employed in these geometries struggle to fully capture all the physics. With this, the success of these approaches has been limited when it comes to the details of the flow analysis [38]. The fact there is limited two- and three-dimensional experimental data results in problems validating RANS-based approaches. This comes from the complexity of the flow domains which complicate

the data gathering for experimentalists [32].

Schemes that are better suited to accurately capture the flow through pebble beds are LES and DNS. LES solves the majority of the turbulent length scales, while modeling the dissipative scales in the given flow. DNS, on the other hand, employs no modeling and solve all the turbulent scales past the dissipation scales. Although these frameworks are more accurate, the computational effort that goes with them are significant. These approaches, due to their computational cost, are usually used for fundamental and idealized cases [1, 18, 12, 32]. By studying these cases the flow physics are better understood and used to improve the RANS-based models. This allows RANS-based approaches to give better results for flow through pebble beds.

This section covers the steps taken to capture the high curvature of the geometry with a morphing mesh approach as well as the TKE budget terms for incompressible, isothermal flow over a random packed pebble bed. This TKE is discussed for three different Reynolds numbers, as conducted by the experimental set-up. There is also a preliminary experimental comparison to see how certain simplifying assumptions and geometric uncertainties influenced the simulated results.

4.2 Methodology

This section will present the research methodology used for the random pebble base. The scope of the problem, computational aspects and consideration, as well as discretization and simulation parameters, will be given.

4.2.1 Case Outline

The flow domain covered in the rest of this dissertation is that of a randomly packed pebble bed obtained from an experimental set-up, done by Texas A&M, the specifications of the geometry can be found in Table 4.1. The experiment consisted of uniform diameter acrylic pebbles randomly placed into an acrylic tube, as seen in Figure 4.1a. A section of the core, several pebble diameters thick, was then scanned using PIV. A graphical algorithm was then used to determine the coordinates of each pebble‘s center by combining multiple snapshots, spaced equal distance apart.

Table 4.1: Actual and Normalized Data for the Randomized Domain.

Parameter	Actual	Normalized
Number of scanned pebbles	147	147
Pebble Diameter	22.25 mm	1
Tube Inner Diameter	140.01 mm	6.285
Scanned Height	123.48 mm	5.55

(a) Experimental set-up.

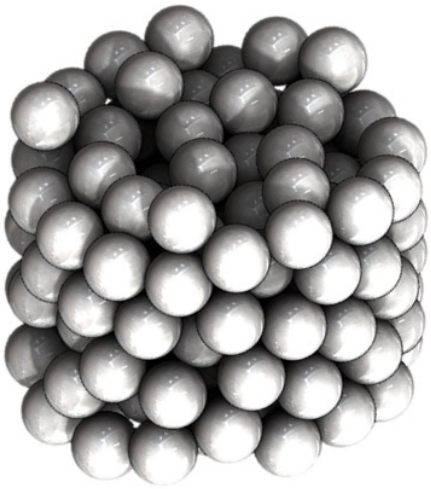

(b) Solid Works geometry.

Figure 4.1: Figures showing the experimental and computational domains.

Due to the high curvature of the pebbles, light infraction resulted in some fuzzy pebble boundaries. The lack of high quality on the boundaries required the algorithm being run multiple times to determine an average pebble coordinate. These coordinates were then used to determine the flow domain in SolidWorks, Figure 4.1b, which would then be used to generate the mesh. When

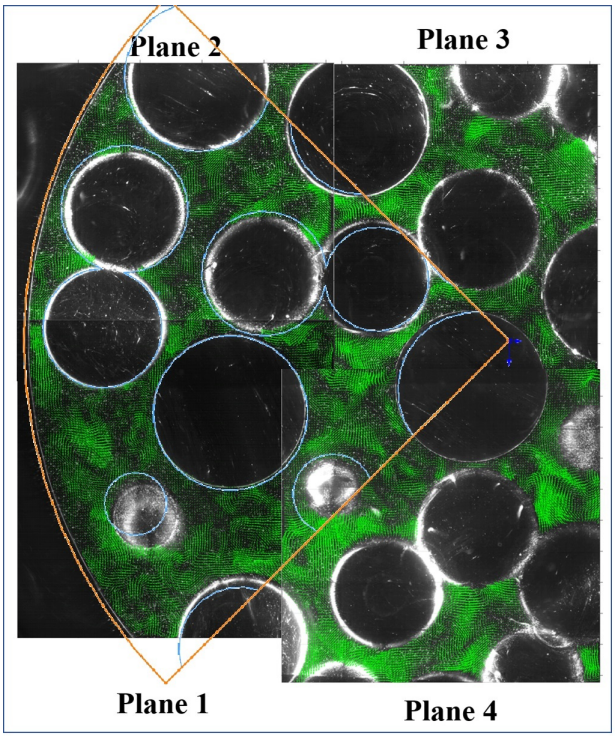

Figure 4.2: The SolidWorks model superimposed on the experimental PIV region to compare accuracy of given pebble locations.

the coordinates and SolidWorks model were inspected, Figure 4.2, minor deviations were found in the pebble locations due to experimental uncertainties. Due to the quality of the PIV images and the method used some of the pebbles showed minor overlap and some deviation from the actual location. An initial shaking algorithm was used to see if these overlaps could be removed, but due to the nature of the problem, the final geometry was significantly different from that of the experimental one. In the end, it was decided to keep the overlaps, as this can potentially capture pebble deformation due to continues operation and friction experienced in actual reactors, which will result in non-uniform pebble diameters.

From literature, only limited DNS and LES investigations on flow over pebbles have been conducted. Most of these studies were done on idealized, structured pebbles cases, as seen in work done by [1]. No DNS studies have been done on randomly packed pebble beds, nor have extensive experimental results been published, [32].

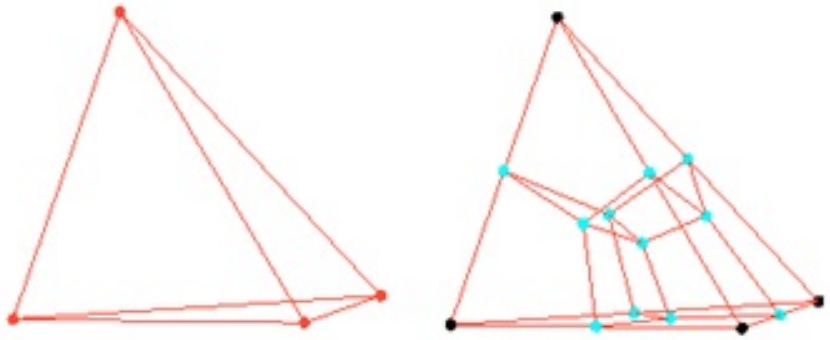

Figure 4.3: The method of how one tetrahedral element (left) gets converted to four hexahedral elements (right) [2].

Within the flow domain all wall surfaces, pebbles and bounding wall, was treated as no-slip walls. To approximate the effect of downstream pebbles, the inlet and outlet of the domain were set to periodic conditions. This was used to replicate an infinite pebble bed, due to the lack of actual geometry.

4.2.2 Meshing

As mentioned in the previous chapter and work done by Fick [1], Nek5000 requires the domain to be decomposed into hexahedral elements. For simple geometries such as the two pebbles and unit cell [1] the traditional block meshing can be utilized to generate a structured mesh. When the complexity of the geometry passes a certain threshold, this method becomes time-consuming and sometimes even impossible. For idealized cases the symmetry of the geometry can be exploited, but for the random pebble case, no such symmetry or unit cell exists, thus making conventional block meshing techniques inadequate for this case.

In order to generate a structured mesh for Nek5000, a new meshing approach had to be developed. A tet-hex meshing method, developed by Argonne National Lab, was used and modified to mesh the unstructured pebble bed. The basis of this approach is to decompose each tetrahedral element into 4 hexahedrons. This method utilizes the ability of a tetrahedral mesh to capture complex geometries, while allowing a structured mesh for Nek5000.

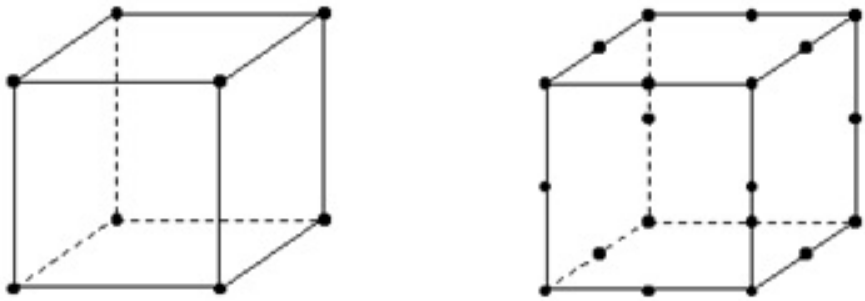

Figure 4.4: Hexahedral 8 element (left) and hexahedral 20 element (right) [3].

Current commercial and open-source codes provide the ability of automatically generating pure tetrahedral meshes for any geometry. For this study, ANSYS-meshing [2] was used to generate the pure tetrahedral mesh after which ANSYS-ICEM [3] was used to convert the mesh elements from tetrahedral to hexahedral. The method of how one tetrahedral element is decomposed into four hexahedral elements is shown in Figure 4.3.

The hexahedral elements generated from this method is known as hex8 elements, as they can be defined by the 8 corner vertexes. It is known that Nek5000 utilize second order elements to better capture the curvature of the geometry. These hex20 elements [3] have points defined halfway between each corner vertex, as seen in Figure 4.4. Hex20 elements can be projected to fully describe and capture the curvature of the geometry. With the ability to project the mid-side nodes, larger and few elements can be used to capture the geometry. Not only does this decrease the mesh size significantly, but the mesh conforms better to the geometry. This allows structured meshed to be generated for complex geometries, such as the random packed pebble bed.

With the ability to generate a structured mesh with the tet-to-hex method and the knowledge of the mid-side nodes of hex20 elements, the moving boundary projection method, used for the random pebble case, can be described.

First, the geometry was modified by increasing the pebble radius with the boundary layer thickness. The bounding wall radius was in turn, reduced by the boundary layer thickness. Next, the new flow domain was imported into meshing package of ANSYS WORKBENCH [3]. The ge-

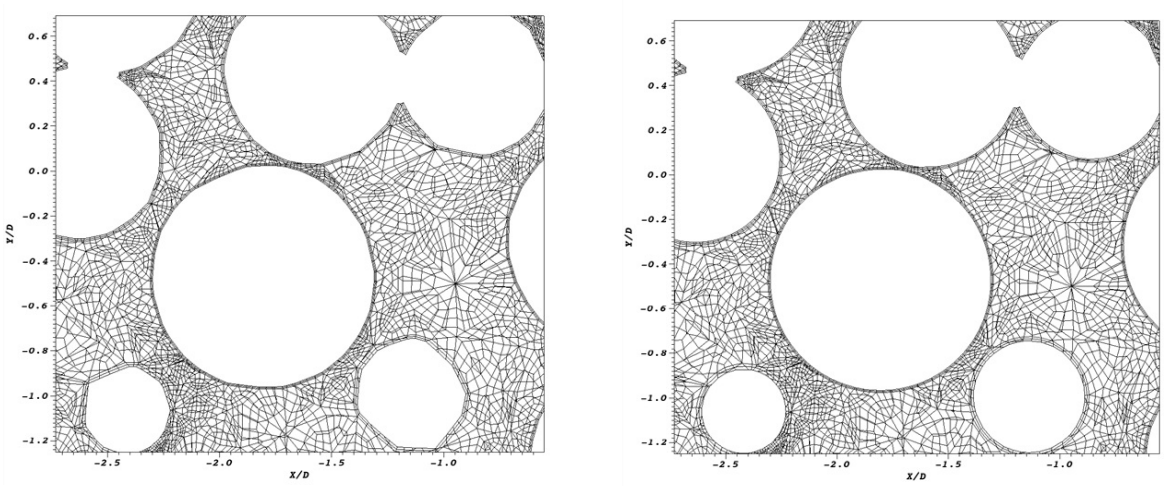

(a) Before moving boundary projection is applied.

(b) After moving boundary projection is applied.

Figure 4.5: A cut plane to show the effects of the moving mesh projection technique for N=3.

ometry was then meshed using a full tetrahedral mesh. The base size was increased to ensure a minimum cell quality of 0.01 as obtained.

Next the tetrahedral mesh is imported in ICEM-CFD [3]. Where the tetrahedral mesh is converted into hexahedral elements, by dividing each tetrahedral into 4 hexahedrons. From this point, the boundary surface elements are extruded by the boundary layer thickness, resulting in uniform hexahedral elements on the surface of the pebbles. This method resulted in the mesh of 865,394 elements, having the required boundary layer thickens, but not conforming to the shape of the pebbles, as seen in Fig 4.5a

The mesh is then exported to the standard Nek5000 format and all required wall and periodic boundary conditions are applied. Once within Nek5000 a mesh morphing algorithm, initially developed by Yuan at Argonne National Lab for a single pebble, was then modified for the entire domain and used to project the boundary layer elements to the geometry.

When the mesh is loaded into Nek5000, each base element is subdivided by an Nth-order GLL polynomial. Knowing the coordinates of each pebble‘s centroid, as well as the location of each surface element vertex the distance between the sphere radius and surface element vertex can be

calculated. Using the know difference in position, a radial velocity field is applied to all surface elements, as a function of the relative distance it should move. A protected layer thickness, δ , is selected to ensure all elements a set distance from the surface element moves the same distance. This keeps the boundary layer thickness uniform over all elements. The algorithm then determines the distance, h, to the closest wall following the radial outward facing normal, from the element. The velocity is then diffused for a set number of time steps following the decaying function:

$$v(t) = v(t) + 100e^{(\frac{h(t)}{\delta})^2} + 100e^{(\frac{h(t)}{2\delta})^2} \tag{4.1}$$

This allows for large element movement where the distance between pebbles are large and dampens the movement where pebbles are in close proximity of one another. This dampening protects elements in between two walls, in close proximity, of being warped and causing negative Jacobians. Figure 4.5b shows a sectional view of the mesh after all surface element movement has been carried out.

From these figures, the pebble-pebble interaction is taken care of due to the increase of the initial geometry, where the boundary elements of pebbles in close proximity is not moved to ensure mesh quality. Depending on the orientation of the cut plane and the pebble locations the effects of the boundary elements not moving can be seen as flattening of the pebbles.

4.2.3 Interpolation

Figure 4.6a shows the location and direction of the laser sheet, as well as the different windows the camera was focused on to take the PIV measurements. Due to the diffusion of the laser sheet it was recommended to keep the DNS investigation to the region for windows 1 to 4, as these would give the best data for the near wall region close to the laser sheet origin. From this, the interpolation and time history locations were selected within this region. Figure 4.6b shows the sphere ID as well as the numbering convention used for the interpolation lines and time history probes for the domain in the [X/D, Y/D, -2.285D] plane.

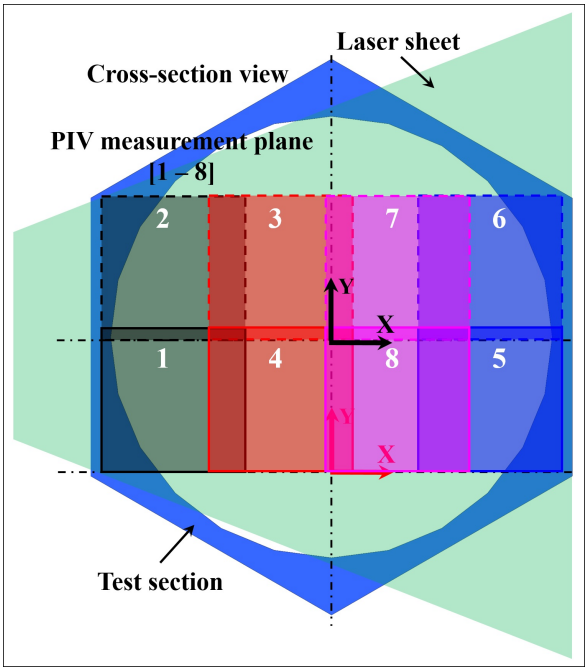

(a) PIV laxer location and window overlap at [X/D,Y/D,-2.285D]

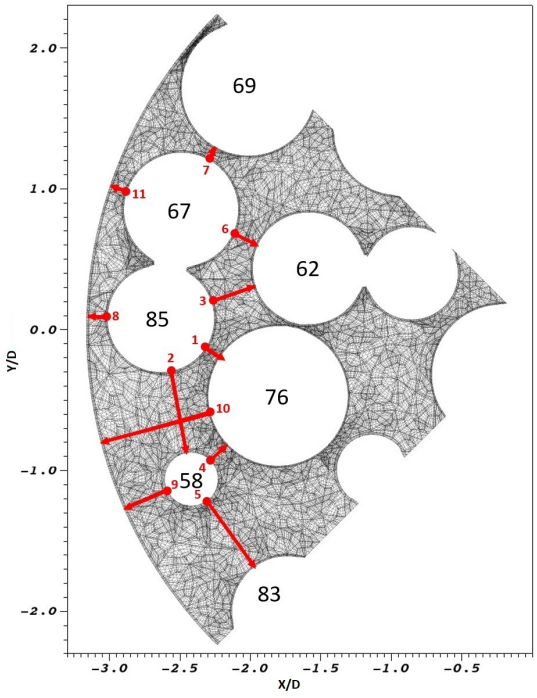

(b) Numbering convention for the line probes in the random packed pebble bed.

Figure 4.6: Justification of the interpolation line and time history locations.

The interpolation line locations, for the pebble-pebble and pebble-wall, was chosen so that the lines are normal to the specific surface. Each line was subdivided into 100 equally spaced points of the length, L, of the line. To simplify, all the lengths were normalized to one for better representation. With the random packing nature of pebble bed, the tail of the arrow indicated the origin ($L = 0$) as well as the line number, where the arrow tip is the end ($L = 1$).

4.2.4 Computational Consideration

As stated the mesh was generated using the tet-to-hex method to create a full hexahedral mesh with adequate boundary layer thickness. This meshing technique resulted in a mesh with 865,394 elements. Figure 4.7 shows a plane of the mesh at [X/D,Y/D,-2.285D] for the N=5 mesh, that is the 5th-degree mesh resulting in 108 million GLL collection points. From the left two pebbles, the pebble interaction can be seen. In the bottom left corner, the flattening due to the two pebbles in close proximity can be seen. As iterated, this occurs due to the projection dampening mentioned

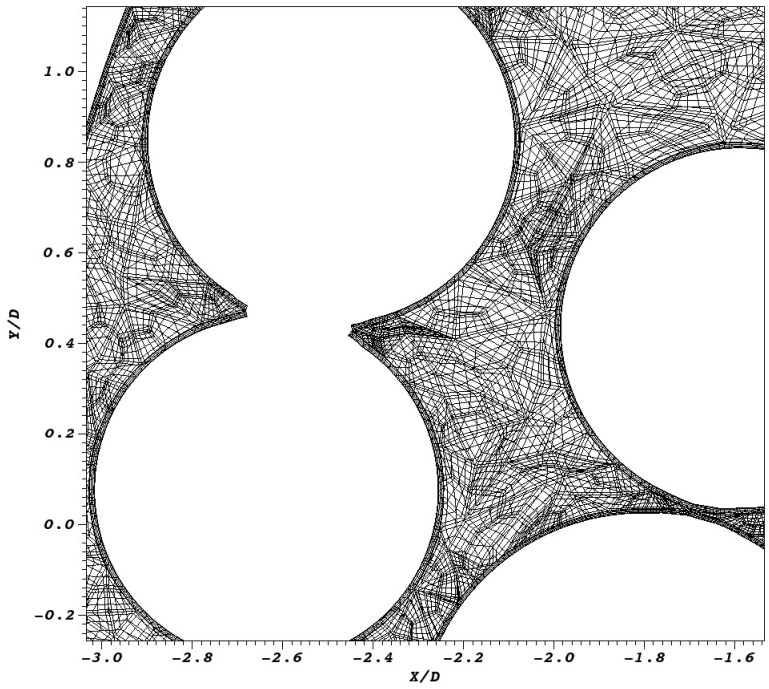

Figure 4.7: Section of the spectral-element mesh after sub-discretization, illustrating the boundary layers, pebble-pebble interactions and close proximity regions for N=5.

in Eq. 4.1. This motion dampening ensures that elements in tiny flow paths are not moved which could result in highly skewed or elements with negative Jacobians.

The little numerical dispersion [39] and dissipation exhibited along with the validation [40] of SEM makes it advantageous to be utilized for DNS. The vicious terms of the Navier-Stokes equations were solved by utilizing an implicit third-order backward differentiation (BDF3) scheme. A third-order, explicit extrapolation (EXT3) scheme was utilized to solve the nonlinear terms. The previous chapters can be referenced if the reader requires more detail regarding the time-stepping scheme.

To decrease the computational time required to develop the flow, third-degree polynomials were used with rapid time-stepping. The flow was allowed to develop for 35 convective time units (D/U), where 5 convective units correspond to roughly 1 flow-through time (FTT). Fig 4.8 shows a cut section of a volume rendering of the instantaneous velocity field for Re = 430 and 1050 after 35 CU, which illustrates the random packing and flow structures.

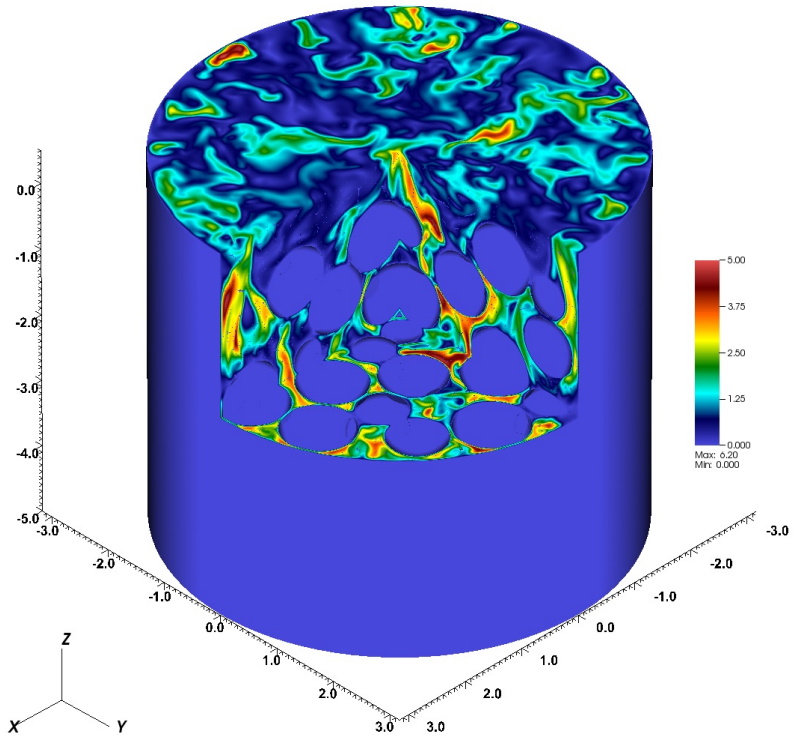

(a) Re = 430

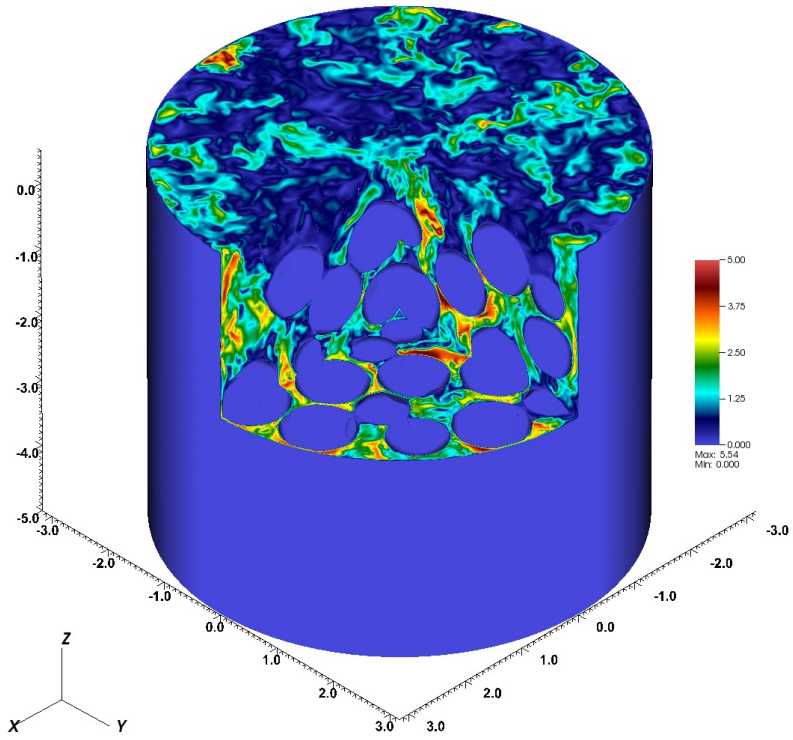

(b) Re = 1050

Figure 4.8: Volume rendering of U_{mag} after 35 CU of flow development.

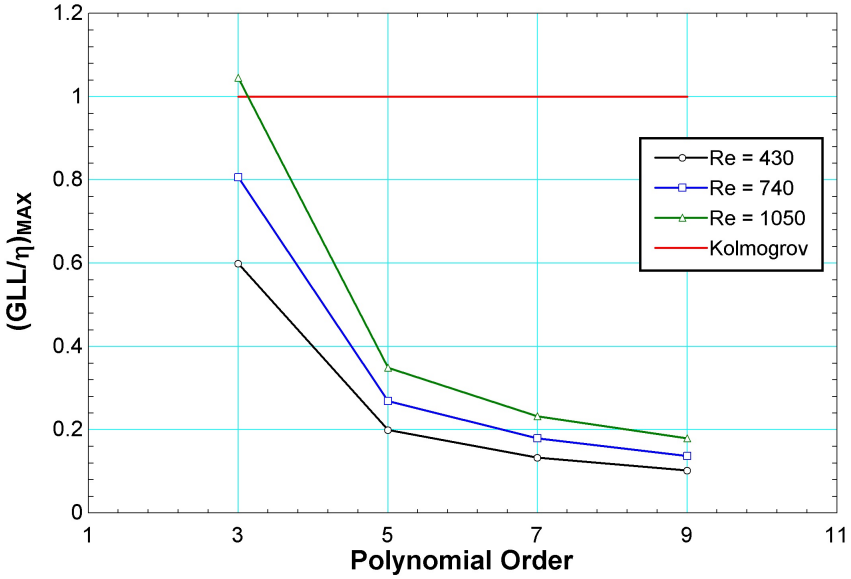

Figure 4.9: Global maximum GLL spacing to Kolmogorov ratio for the different Reynolds numbers to ensure DNS requirements.

To ensure DNS requirement were achieved the TKE dissipation and Kolmogorov scales were calculated for each point in the domain for 1 FTTs at third-, fifth-, seventh- and ninth-degree discretization. Figure 4.9 shows the global maximum Kolmogorov length scale to grid spacing ratio for the different Reynolds numbers. From this figure, it is seen that only a slight decrease in the ratio is observed when increasing above fifth-order discretization. Table 4.2 shows the computational cost used to calculate the Kolmogorov scales for the highest Reynolds number of 1050.

From Fig 4.9 and Tab 4.2 the sheer computational cost required for DNS can be seen. Fick [1] showed that increasing the polynomial order past the DNS requirements only increases the computational expenses without affecting the results. From this, a fifth-order polynomial is used for all the production runs.

The production runs, as well as the post-processing was performed on the IBM Blue Gene/Q MIRA and CETUS clusters located at the ALCF at Argonne National Laboratory.

Table 4.2: Computational Parameters to calculate Kolmogorov scales for Random packed pebble bed, Re = 1050.

	Polynomial Degree		
Parameter	5^{th}	7^{th}	9^{th}
Time Step length	1×10^{-4}	5×10^{-5}	2.5×10^{-5}
GLL points	108.17×10^6	296.83×10^6	630.87×10^6
Nodes (Cores)	$1024(16384)$	$2048(32768)$	$4096(65536)$
Total FTT	1	1	1
Core Hours/FTT	245.76×10^3	737.28×10^3	4.571×10^6

4.2.5 Turbulent time scales

The auto-correlation function (ACF) is used to characterize the temporal dependencies of a random signal. The ACF is useful as it characterizes the time scales of turbulent motion at a specific point with itself over time. The ACF of the three different cases can be compared to show that the data sets deliver a consistent time evolution of the fluctuating velocities, and thus if they are resolved in time. The ACF for the three different fluctuating velocity magnitudes, u_{mag}, is plotted in Fig 4.10. For each Reynolds number, the fluctuating velocities of the last 60 seconds were extracted from the total time history and the ACF calculated. The center point data for lines 3 and 10 were chosen for the temporal investigation. These were chosen as a near wall and far field location, as well as in large and moderate flow restriction. For each case data, the signal was lagged with $200,000$ time steps, which equated to $20CUs$, and the ACF was computed.

From Fig 4.10, top and bottom right, the ACF decays rapidly to for both lines within the first $0.2CU$, after which it starts to oscillate and approach zero asymptotically. For line 3 (top left and right) the frequency of the oscillations is higher with only one or two local minimum and maximum. Due to the strong mean flow gradient present in the large contraction for line 3, little correlation would be expected. For line10 (bottom left and right) the span of the gap is larger. With the larger flow path the average mean flow gradient is weaker and a lower oscillation in the correlation is seen. For the low (430) and intermediate (740) Reynolds number a few predominant

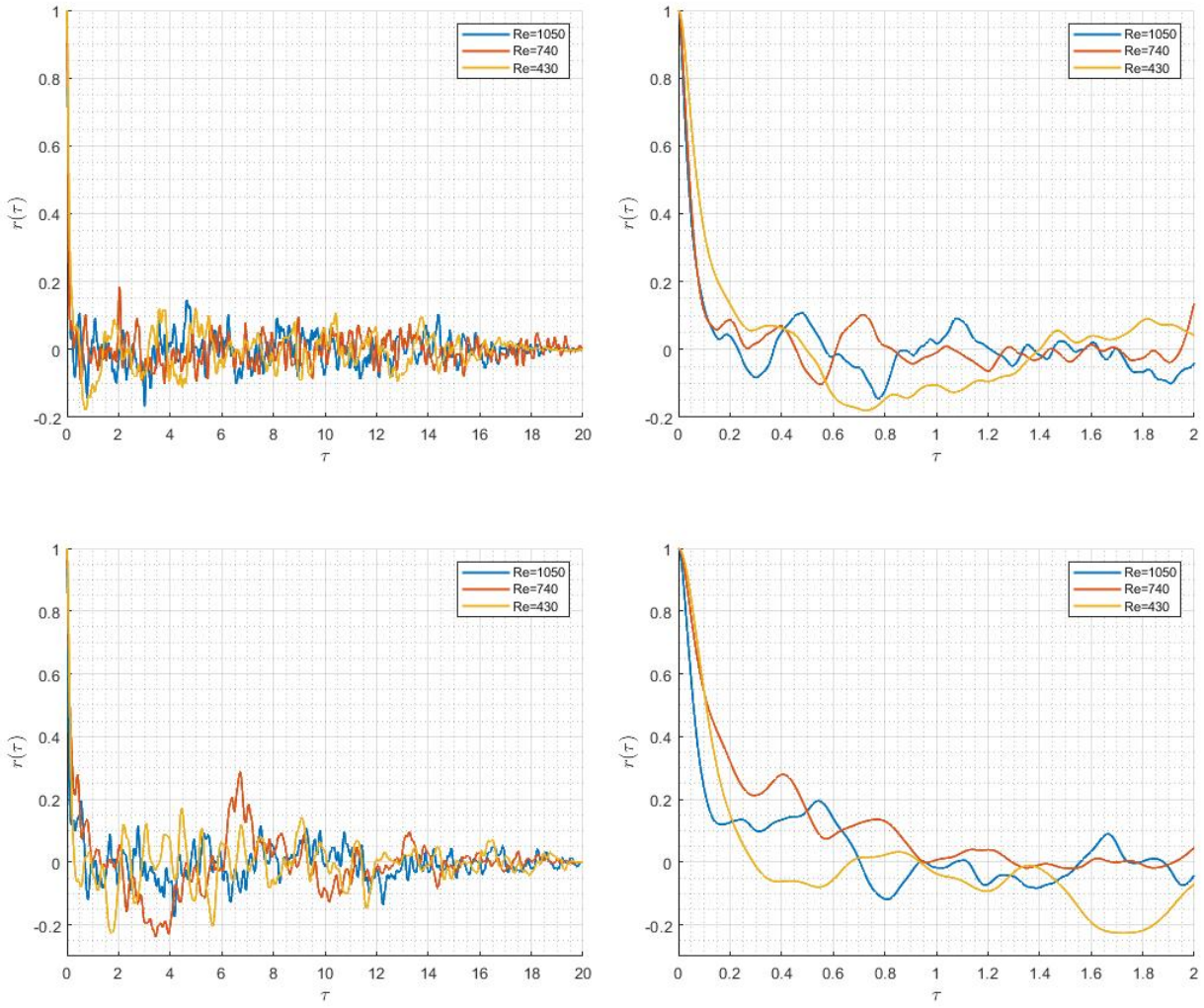

Figure 4.10: Temporal ACF for the entire time history (left) and zoomed in on the first 2 CU (right) of $\langle u_{mag} \rangle$ for the center point of line 3 (top) line 10 (bot).

peaks can be seen at around $\tau = 2$ and 6 for $Re = 430$ and $\tau = 4$ and 7 for $Re = 740$. Indicating an increase in correlation. As the time signal is increased, these also decrease and approaches zero asymptotically.

4.2.6 Statistical stationary

From the Kolmogorov calculations, Table 4.2, the computational cost to run consecutive FTTs can be seen as the polynomial order was increased. As Fick [1] showed with his FCC cases, the

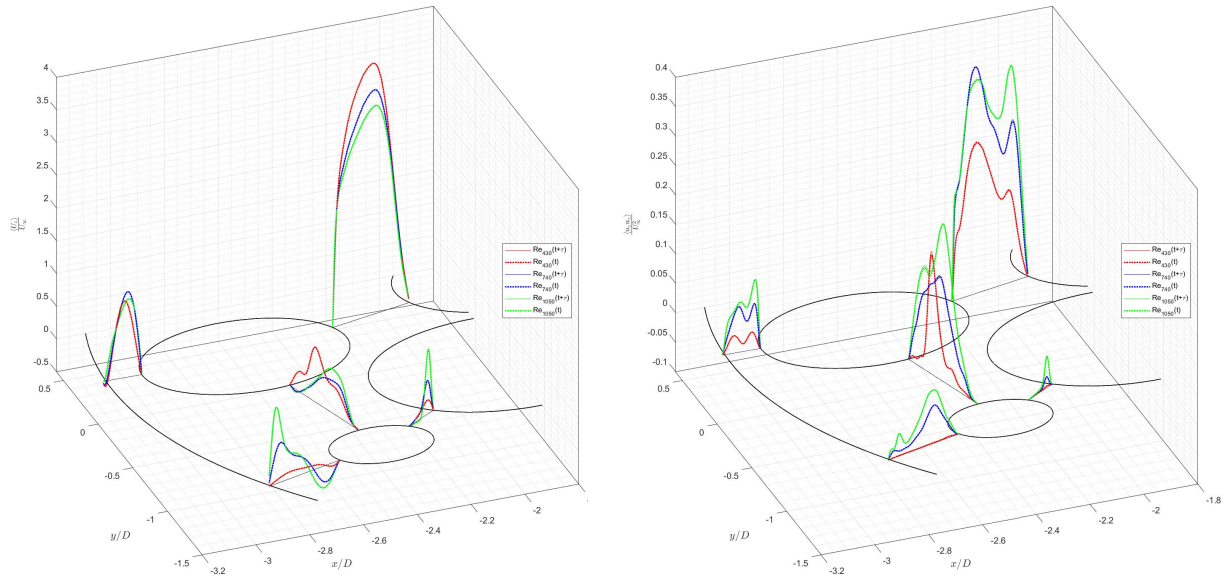

Figure 4.11: Interpolated profiles for the steam-wise averaged velocity $\langle U_z \rangle$ (left) and the Reynolds stresses $\langle u_z u_z \rangle$ (right) for times $f(t) = 22$ FTT and $f(t+\tau) = 23$ FTT for the $N = 6$ data set.

increase in polynomial order did not affect the solution, but rather the time it took for converge.

For the three Reynolds numbers under investigation, a total of 23 FTTs were simulated at $N = 5$. In order to efficiently use resources and the ALCF queue scheduler a checkpoint save and restart methodology was used. The production runs were submitted for 6-hour intervals that resulted in 2 CUs of simulation data per submission. The averages and the TKE budget terms were computed and outputted every CU or $10,000$ time steps. This was done to enter the shortest possible queue system, allowing for as frequent submissions as possible.

Once 1 FTTs (5CUs) data was present, the total running averages were calculated. To ensure that the flow has been averaged long-enough and that the statistics are satisfactory, the two most recent averaged line-out results were compared to one another to ensure that the solution is time independent. The shift size, measured in FTT‘s, between the different compared checkpoints are indicated by τ. The interpolation lines are projected onto the [x,y,0] plane and illustrated at the corresponding location within the domain. The line locations and numbering convection detailed

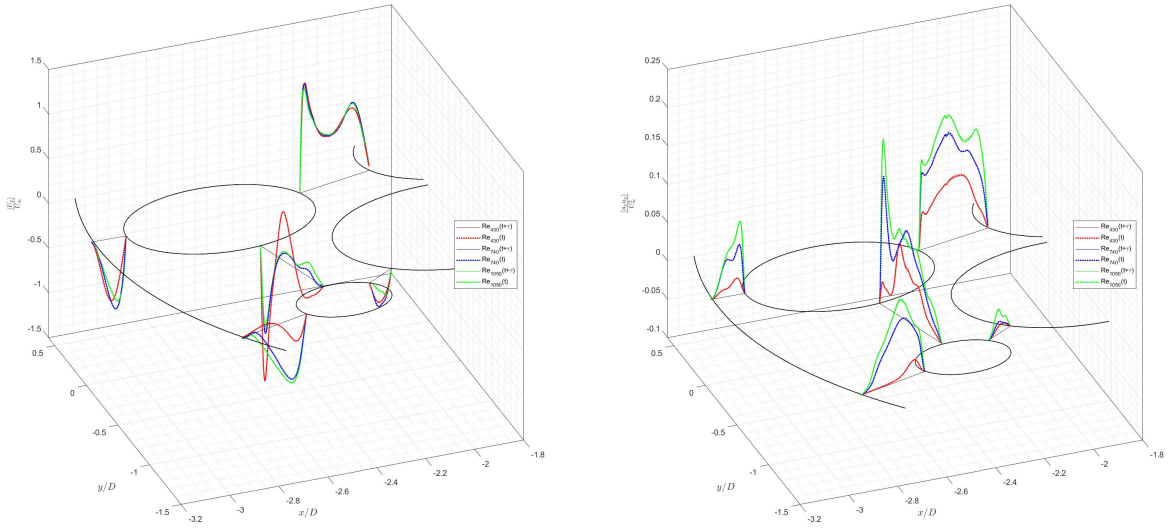

Figure 4.12: Interpolated profiles for the averaged velocity $\langle U_x \rangle$ (left) and the Reynolds stresses $\langle u_x u_x \rangle$ (right) for times $f(t) = 22$ FTT and $f(t+\tau) = 23$ FTT for the $N = 6$ data set.

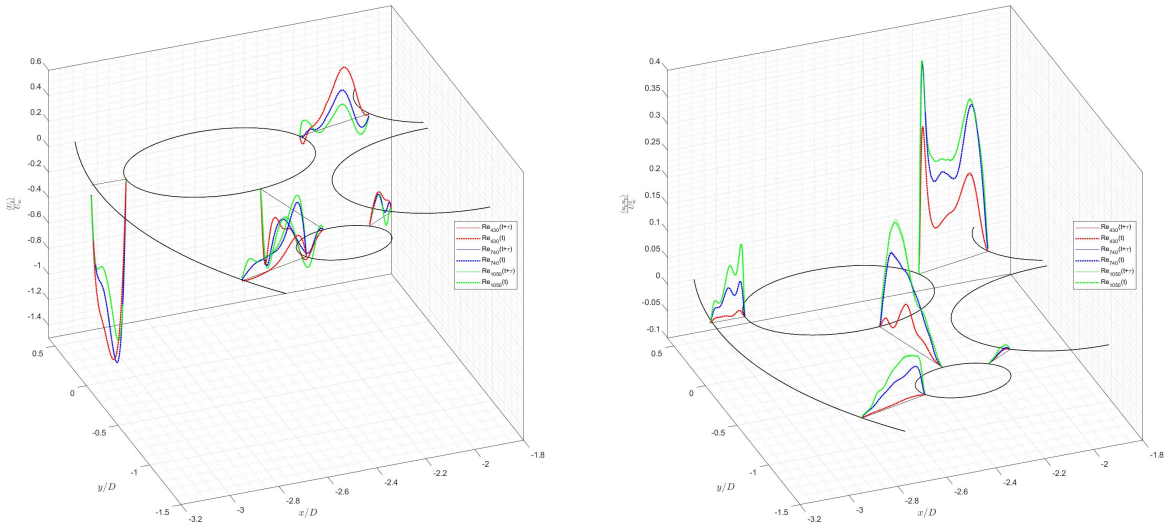

Figure 4.13: Interpolated profiles for the averaged velocity $\langle U_y \rangle$ (left) and the Reynolds stresses $\langle u_y u_y \rangle$ (right) for times $f(t) = 22$ FTT and $f(t+\tau) = 23$ FTT for the $N = 6$ data set.

in Fig. 4.6b was used.

The diagonal components of the averaged velocity and Reynolds stresses, non-dimensionalised by the inlet velocity, are shown in Fig 4.11, 4.12 and 4.13. Form these the convergence for the fifth-degree data set for all three Reynolds numbers can be seen. The interpolation lines are drawn for the defined coordinates within the [X/D,Y/D,-2.285D] plane. For the chosen time shift of τ the data shows acceptable statistical stationarity for both the near and far field profiles.

4.3 Results and Discussions

The subsequent section is a discussion of the quantitative and qualitative analysis of the data in the near wall region for the three different Reynolds numbers. As this is a DNS study no grid independence was done, as Fick [1] showed that increase polynomial orders do not affect the flow solution and the computational and storage resources required for GCI in this cases was also not feasible. Rather than a grid independence study, a boundary sensitivity study, presented in the next chapter, was done by decreasing the domain side to a quarter of the original case. Different boundary conditions were enforced on the cut plane to see how it would affect the streamwise, and lateral flow for the domain as limited experimental data was available. For this section Visit was used to visualize the flow data.

4.3.1 Inter-data-set comparisons

Figures 4.11, 4.12 and 4.13 shows the averaged velocity and Reynolds stresses for the three different Reynolds numbers. From the stream-wise velocity in Fig 4.11 the effects of the different Reynolds numbers can be seen. For the larger flow paths, such as line 3, the lower Reynolds number has a higher averaged velocity, while in narrow contractions the flow is less. This is due to the flow being more vicious driven. With the higher viscosity of the lower Reynolds number flow, the fluid prefers the larger flow regions as the wall effects and friction in narrow regions essentially block of the flow. As the inlet Reynolds number is increased by a decrease of viscosity. The wall effects in narrow regions become less dominant and the flow can penetrate the smaller region, thus redistributing the flow and decreasing the average flow in the larger flow paths. In the near wall

region, a change in stream-wise velocity direction is observed close to the bounding wall.

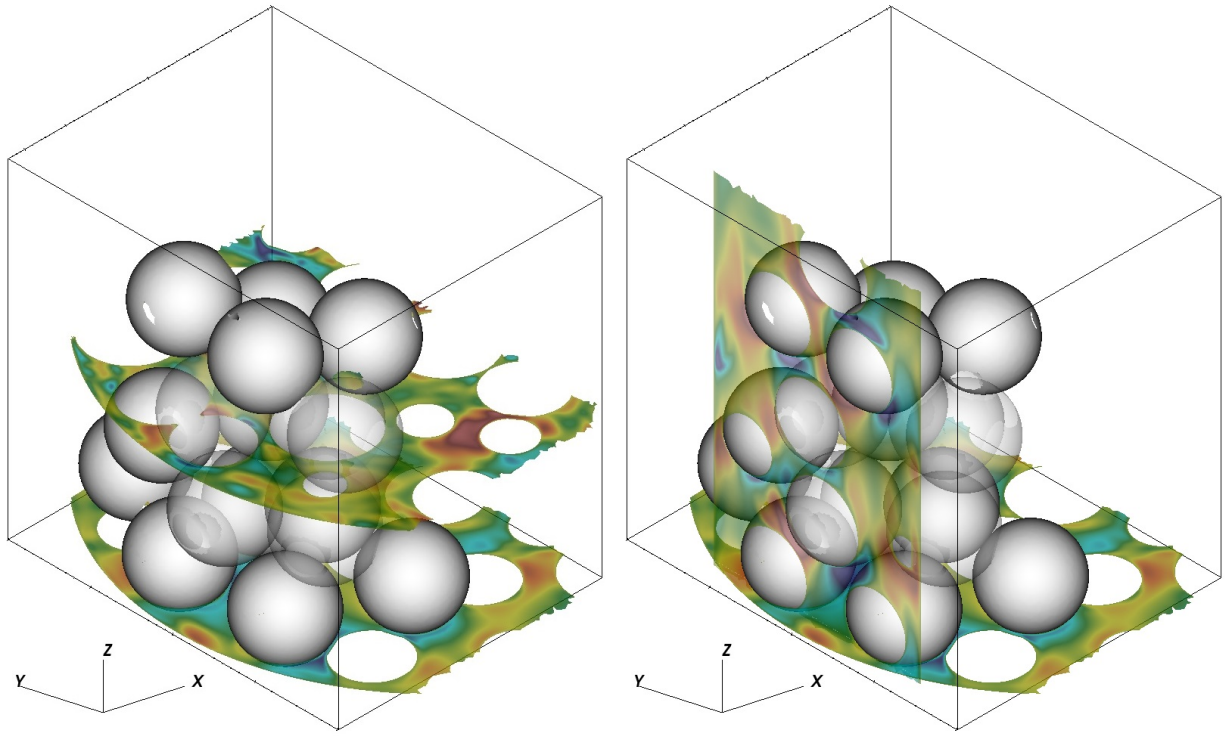

(a) Plane [X/D, Y/D, -2.285D] (b) Plane [-2.9D, Y/D, Z/D]

Figure 4.14: Three-dimensional representation of the pebble packing structure around the plane of interest.

Due to the complex geometry of the random packed pebble bed, some time needs to be spent on investigating the pebble structure around the plane of interest. Figure 4.14 shows the near wall region that will be investigated. Figure 4.14a shows the location of the horizontal plane at [X/D, Y/D, -2.285D], with the closest pebbles turned transparent to show the inter pebble regions. This also serves as a visual interpretation of the packing structure so sensible analysis of the TKE terms can be performed. From this and Fig. 4.6b that plane intersects the downstream surface of pebbles 63 and 85, the upstream surfaces of pebbles 58, 67, and 69 and pebble 76 through the origin. Knowing how the pebble surfaces change in the stream-wise direction will further aid in the sensible analysis of flow paths, recirculation as well as detachment and reattachment zones.

Figure 4.14b shows the cut plane in the near wall region, at [-2.9D, Y/D, Z/D] that will be used to identify stream-wise structures. The bottom plane [X/D, Y/D, -4/D] is just a preview to give a point of reference for the bounding wall location.

Fig 4.15 shows the pseudo-color plot of the averaged in-plane velocity magnitude, $\langle U_{xy} \rangle$, with the vector direction overlaid to show the regions of recirculation. Vectors pointing on the pebble surfaces shows regions of reattachment and vectors pointing from the surfaces shows flow separation regions. With the plane intersection, the upstream surface of pebble 58 (The small sphere profile in the near wall region) the separation from the surface can be seen as the flow enters the recirculation zone. It can also be seen that flow detaches from the left side of pebble 85 and flows towards 76 to reattach momentary before entering the larger expansion region.

For the low Reynolds number, Fig. 4.15a, a large low-velocity stagnation point can be seen between $[-1.5Y/D \leq -0.7]$ close to the wall. As the flow is increased, Fig. 4.15b, this stagnation region shrinks and smaller secondary circulations regions develop closer to the pebble surfaces where the detachment occurs, the maximum velocity is also decreased as the flow becomes more turbulent and the smaller inter pebble regions can be penetrated by the flow. With the highest Reynolds number, Fig. 4.15c, a further decrease in the recirculation region and total velocity is seen. There is still a strong flow detachment from the upper pebble, but more secondary reticulations form in the larger inter pebble gaps.

The diagonal components of the streamwise Reynolds stresses, $\langle u_z u_z \rangle$, is shown in Fig. 4.16. For the lower Reynolds number Fig. 4.16a the Reynolds stresses are more concentrated in the larger flow regions between the pebbles. Due to the flow being accelerated and having a strong mean flow gradient in the contractions between the pebbles low Reynolds stresses are seen here. The Reynolds stresses are more concentrated in the regions of secondary circulations regions, as the flow in these regions is not as strongly driven by the mean flow. As the Reynolds number is increased Fig. 4.16b the maximum flow is decreased and more secondary flow paths can be used. From this, the Reynolds stresses are more spread out as more fluctuations are present in the larger inter pebble regions. The Reynolds stress is seen to follow the secondary recirculation regions that

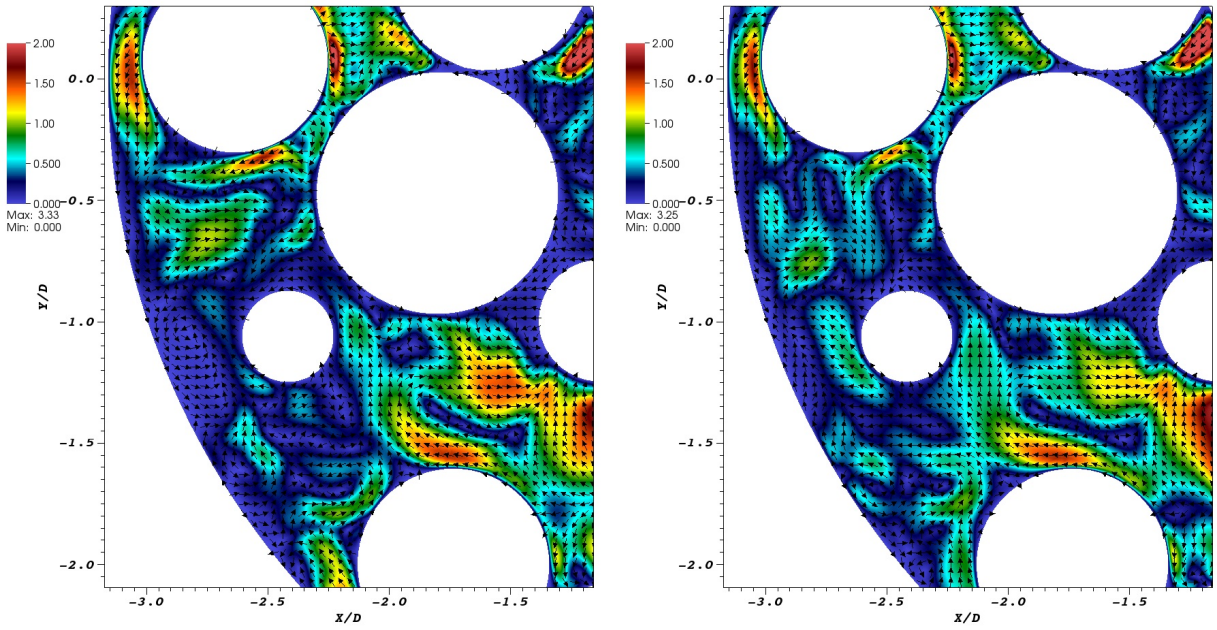

(a) Re=430

(b) Re=740

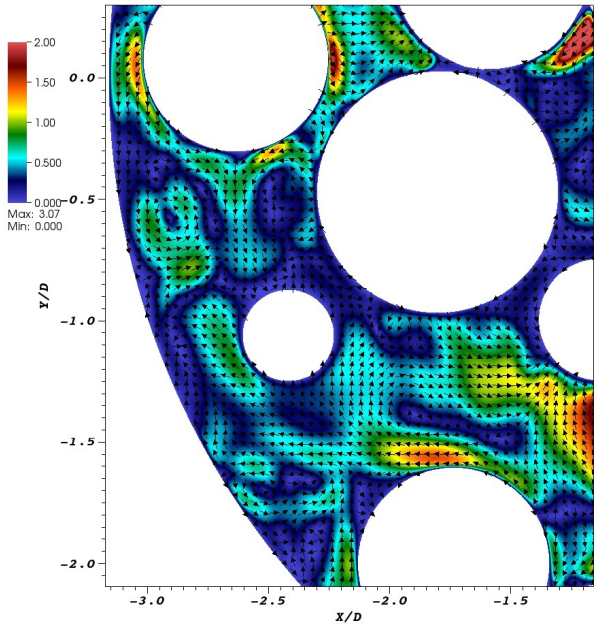

(c) Re=1050

Figure 4.15: Pseudo color field of the in plane velocity magnitude in the plane [x/D,Y/D,-2.285D] with the velocity vector overlaid to show recirculation zones.

are less driven by the mean flow and contain more fluctuations. Finally for the largest Reynolds number, Fig. 4.16c the effects of the reduced mean velocity can be seen was more fluctuations and

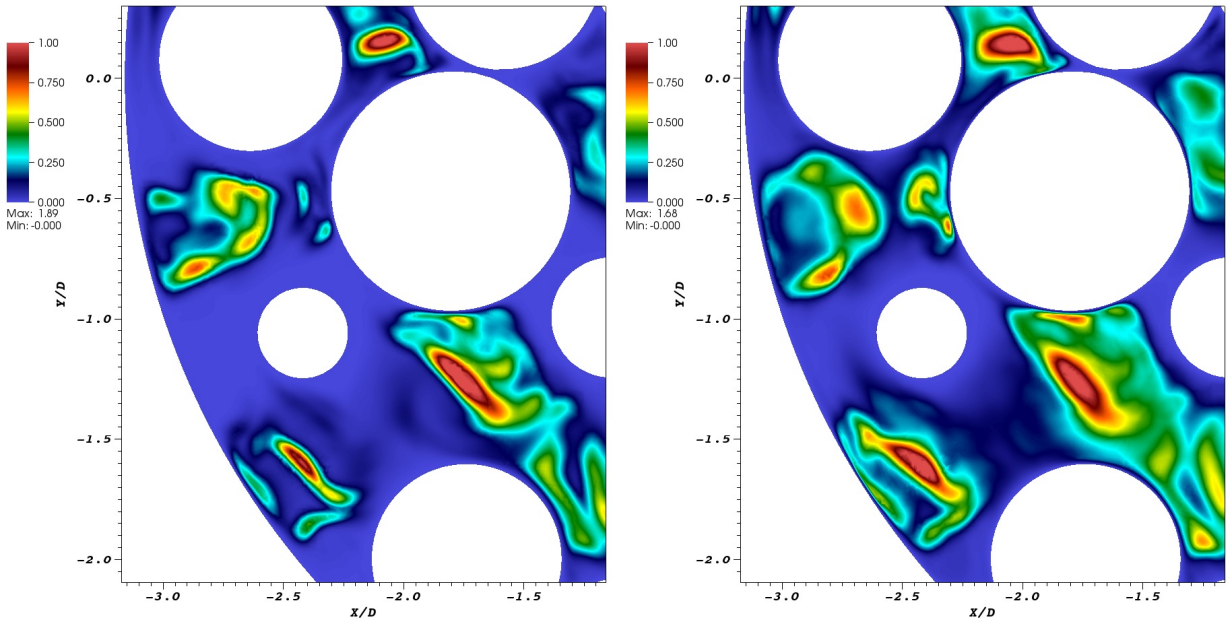

(a) Re=430

(b) Re=740

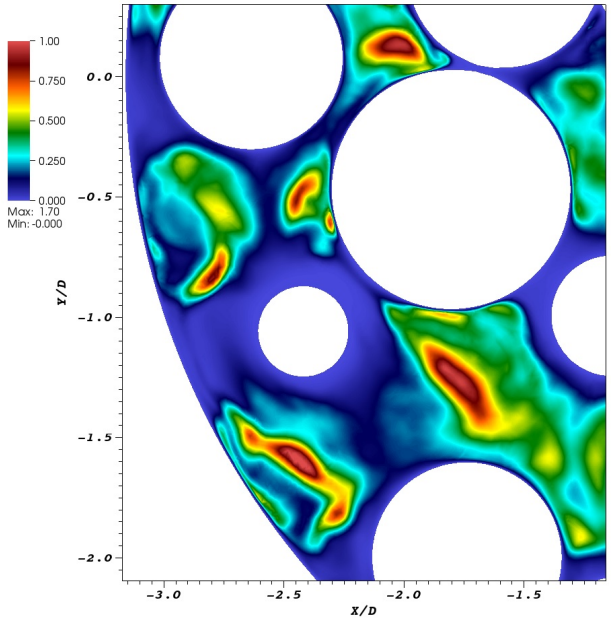

(c) Re=1050

Figure 4.16: Pseudo color field of the in stream-wise Reynolds stress $\langle u_z u_z \rangle$ in the plane [x/D,Y/D,-2.285D].

Reynold stresses are seen in the larger as well as smaller inter pebble regions.

To put the flow dynamics into better perspective the averaged velocity magnitude, $\langle U_{mag} \rangle$, is

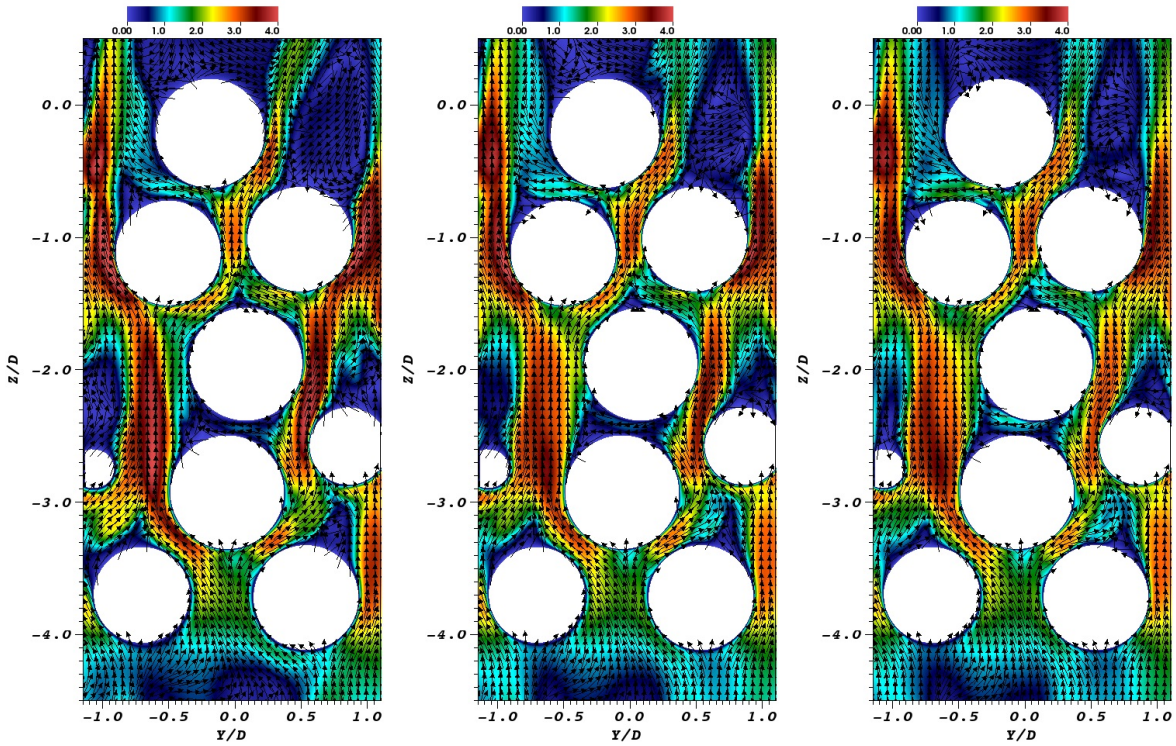

(a) Re=430 (b) Re=740 (c) Re=1050

Figure 4.17: Pseudo color field of the averaged velocity magnitude $\langle U_{mag} \rangle$ for the the plane [-2.9D, Y/D, Z/D].

plotted in Fig. 4.17. From the pseudo-color plot, the recirculation zone can be clearly seen in the wake of the pebble located at $[Y/D = -1, Z/D = -2.8]$. Here we can see that for the lower Reynolds number, Fig. 4.17a, the flow detaches from the pebble surface and produces a relatively large recirculation region. As the Reynolds number is increased, Fig. 4.17b and 4.17c, all the low-velocity regions decrease in size as well as a decrease in overall velocity magnitude as more secondary flow penetrates the smaller inter pebble flow paths.

4.3.2 Turbulent Kinetic Energy

The work done by Fick [1] provided important information regarding the TKE in his high curvature FCC case. It was seen that for a simple two sphere set up the bluff body interactions generated complex flow behavior. The flow results in the FCC case generated a temporal instability that required extensive time stepping to properly capture the phenomena. Even with a relatively

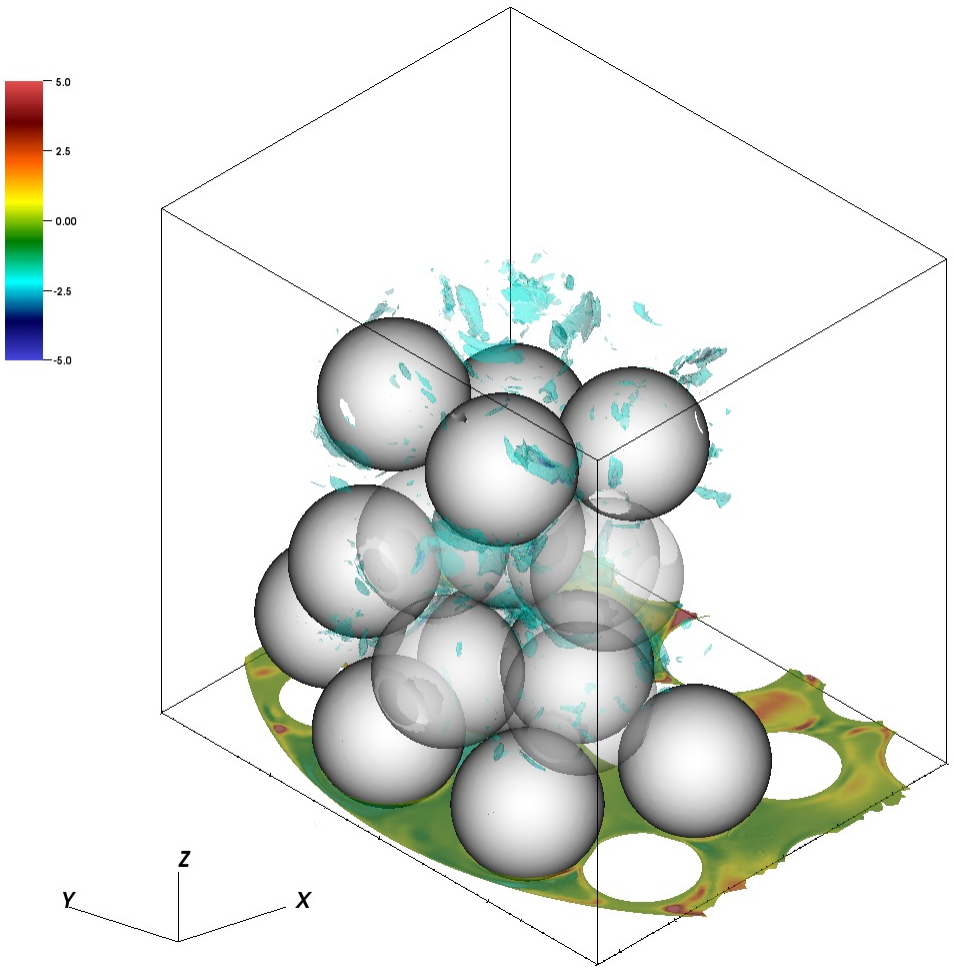

Figure 4.18: Iso-volume rendering of the negative production $-10 \leq P_{zz} \leq -1$ for Re=1050 to show the complexity of the production tensor.

simple FCC and extended FCC geometry complex flow phenomena were seen. For the random case, having high curvature, and a complex geometry the complex flow patterns where investigated, but no temporal instability were seen in the domain. This is due to the random packing having predefined regions of lower resistance where the bulk flow preference, unlike the FCC case where the geometry where symmetric and all flow paths had equal possibility of being utilized.

Figure 4.18 shows an iso-volume rendering of the negative values for the stream-wise production component for the Re=1050 case. Here we can see the complex structures due to the geometry. As expected, the negative production occurs in regions where the flow is accelerated, either by entering a contraction between pebbles or on the downstream surfaces where the flow

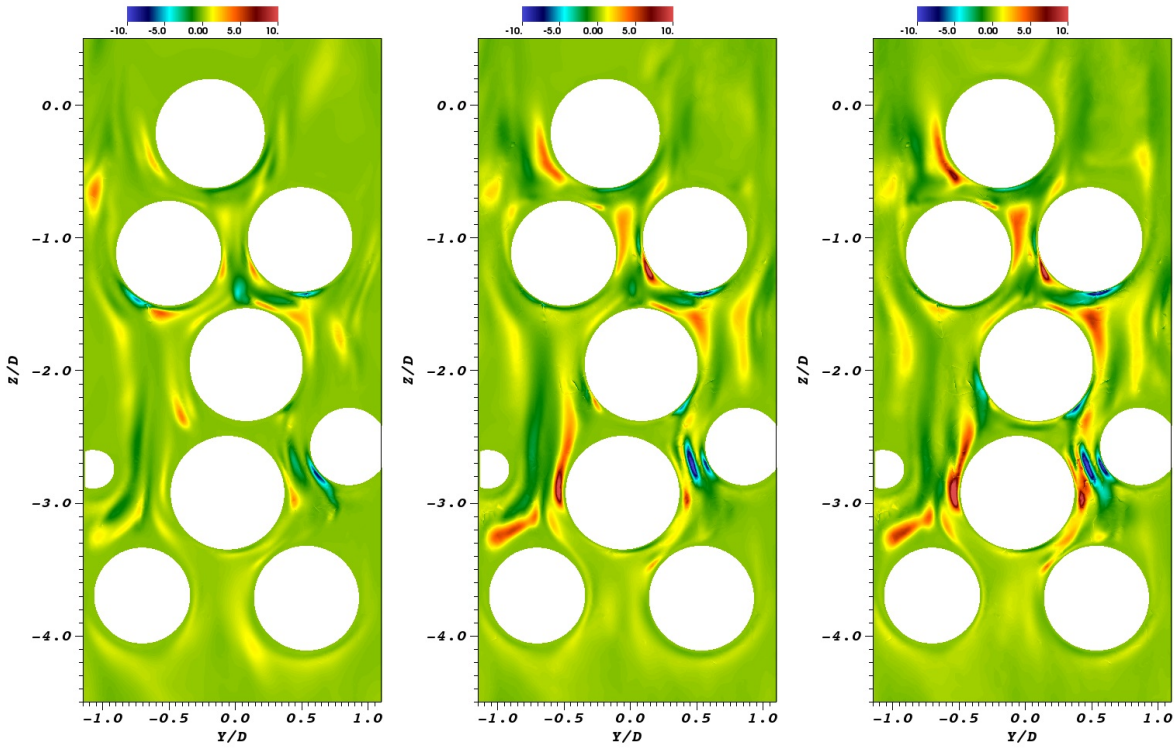

(a) Re=430 (b) Re=740 (c) Re=1050

Figure 4.19: Pseudo color field of P_{xx} for the the plane [-2.9D, Y/D, Z/D].

reattaches.

The TKE fields presented in this subjection were all calculated using the data from the production runs with $N = 5$. The gradients required to solve the TKE's are known to be steeper and requires a higher resolution to accurately resolve, unlike those required for the velocity and covariance data. With the already high mesh density it was found that the current polynomial order was adequate to capture the TKE.

Due to the TKE equation consisting of numerous terms and the research being conducted over different Reynolds numbers an overwhelming amount of data exists that can be plotted. As some of the TKE terms are more relevant to lower order methods, only these components shall be selected to be plotted. The two most important terms, regarding the physical processes taking place in the flow, is that of the production and dissipation of TKE. The data of these two components are also required for lower order models like RANS and LES.

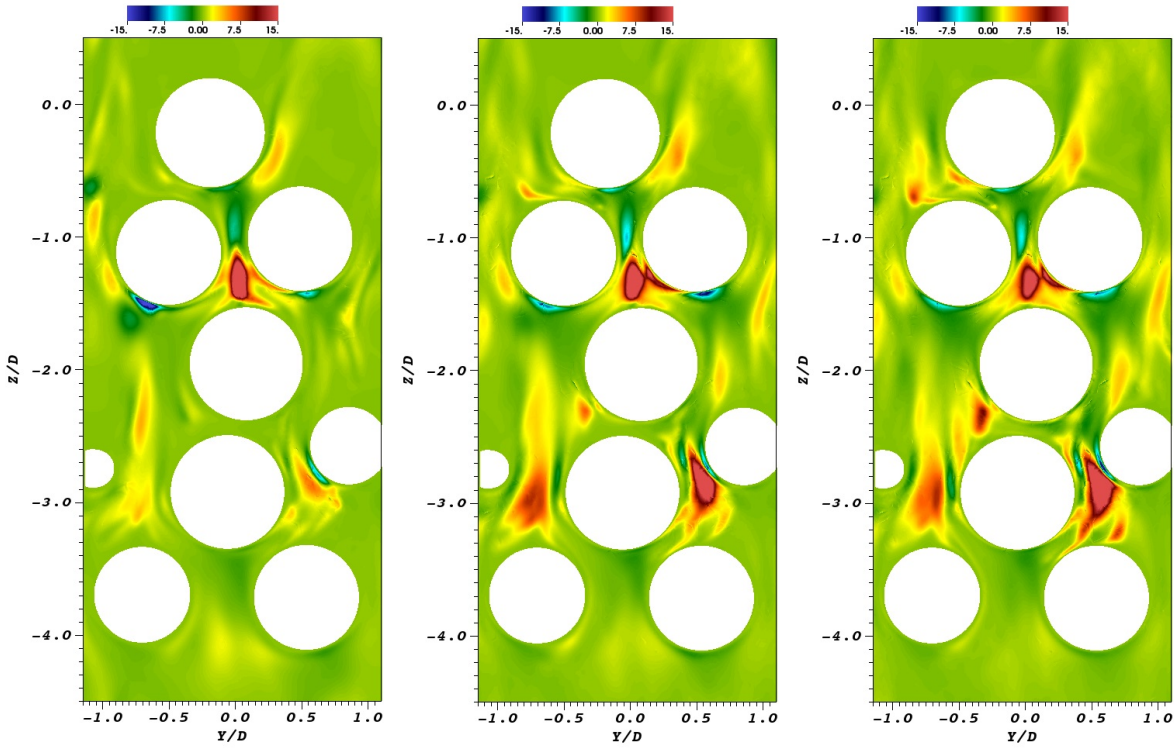

(a) Re=430 (b) Re=740 (c) Re=1050

Figure 4.20: Pseudo color field of P_{yy} for the the plane [-2.9D, Y/D, Z/D].

The TKE equation have second order tensors, each containing nine components. Due to the symmetric nature of these tensors only six components need to be reviewed. It should be noted that the individual terms structures‘ are highly dependent on the coordinate frame used. To obtain the magnitude of the specific tensor can be computed by taking half of the trace, e.g. $\frac{1}{2}\epsilon_{ik}$. The magnitude of the tensor is coordinate frame independent. Due to the complexity of the geometry the frame of reference needed to properly represent the data is crucial, as no clear symmetry or pattern exists in the domain. The data will be grouped so that each component can be compared over the three different cases. It was selected to capture the TKE near the wall of interest, all TKE terms will be shown on a plane that is orthogonal to $x = -2.9D$. This allows to see how the budgets develop in the stream-wise direction.

Figure 4.19 shows the diagonal component, P_{xx}, of the TKE for the three different cases, in a plane selected close to the wall of the simulation. For the lower Reynolds number, Fig 4.19a,

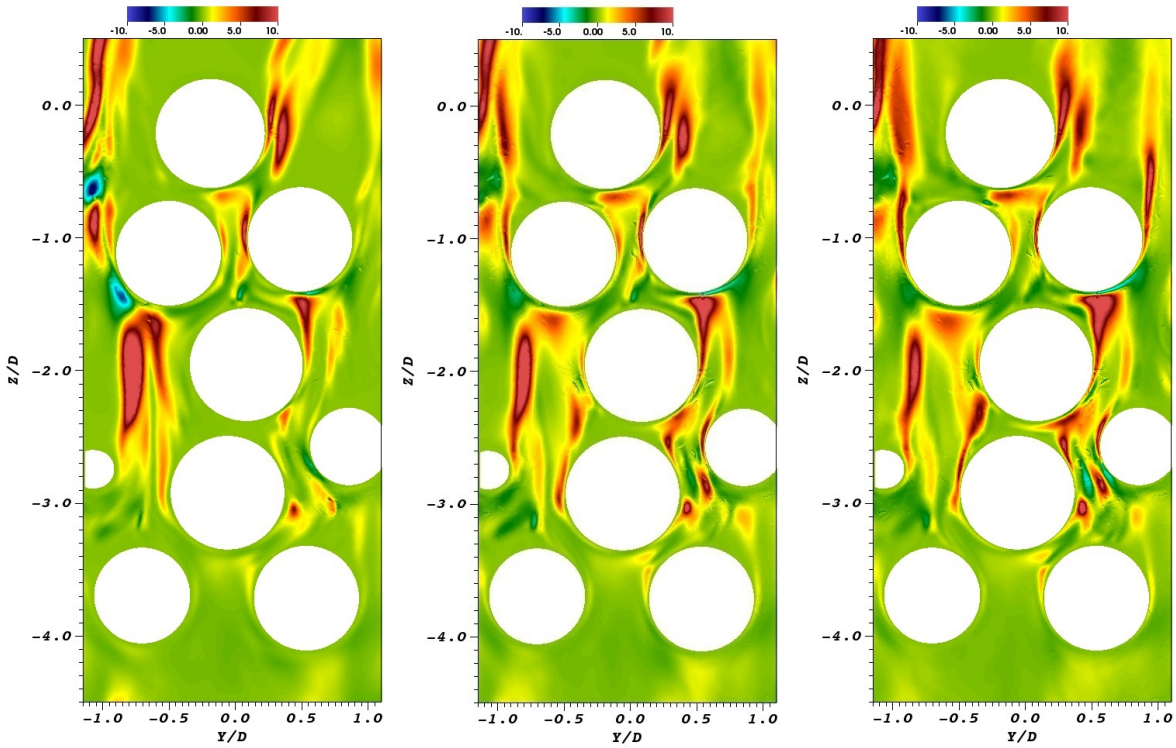

(a) Re=430 (b) Re=740 (c) Re=1050

Figure 4.21: Pseudo color field of P_{zz} for the the plane [-2.9D, Y/D, Z/D].

little production is seen in the inter pebble regions. There is some production on the downstream of a few pebbles. This is conclusive with the analysis that the flow is more vicious driven and lack fluctuations. The flow is driven by the mean velocity that follows the path of least resistance and is biased to larger flow paths. As the Reynolds number is increased, Fig 4.19b, an increase in TKE production is seen in the areas behind pebbles.

Fick [1] found that an increase in production in the wake of his FCC spheres case was indicative of flow recirculation zones. The enhanced TKE production in these areas is attributed to the strong shear layer and flow deceleration between the fluid flowing in a positive and negative velocity in these recirculation zones. This agrees to the presence of a low flow stagnation zones seen in Fig 4.15. For the largest Reynolds number, Fig. 4.19c, higher production is seen in these regions. There is a significant increase in positive and negative production in the closed spaced inter-pebble region.

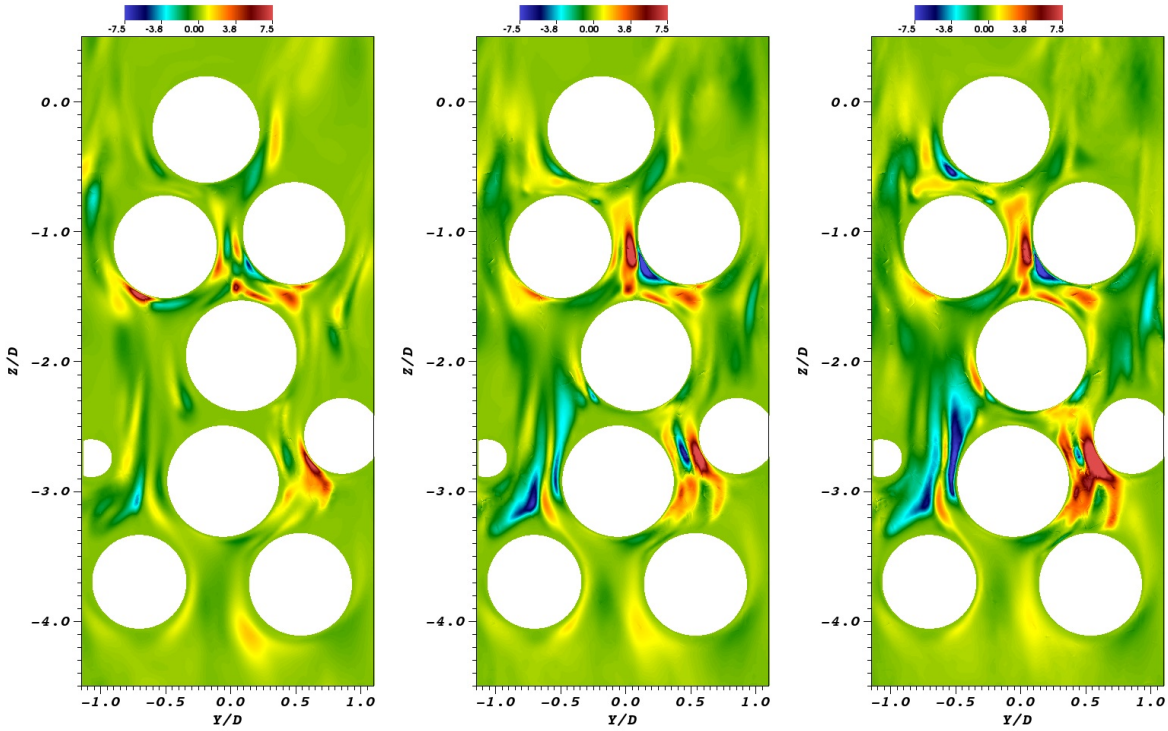

(a) Re=430 (b) Re=740 (c) Re=1050

Figure 4.22: Pseudo color field of P_{xy} for the the plane [-2.9D, Y/D, Z/D].

For the other latter component of the production P_{yy}, Fig. 4.20, higher magnitudes of production is seen in the downstream region of spheres. These magnitudes are higher in the inter pebble regions. Of particular interest are the regions of negative production on the downstream surfaces of the upper pebbles. These are the region where the flow re-attaches to the surface of the pebbles. Once again as the Reynolds numbers are the magnitude with these regions increases. Show that the more turbulent flow is less driven by the strong mean flow, but that the secondary flows start coming into consideration.

Figure 4.21, shows the stream-wise components of the production tensor. The production of TKE is seen to increase in the wakes of the spheres as separation takes place. This is conclusive with the flow rapidly decelerating as it approaches the recirculation or stagnation zone. As the flow is forced laterally into the contractions and sped up, the production magnitude decreases as the flow is more driven by the average flow rather than secondary fluctuations. For the low

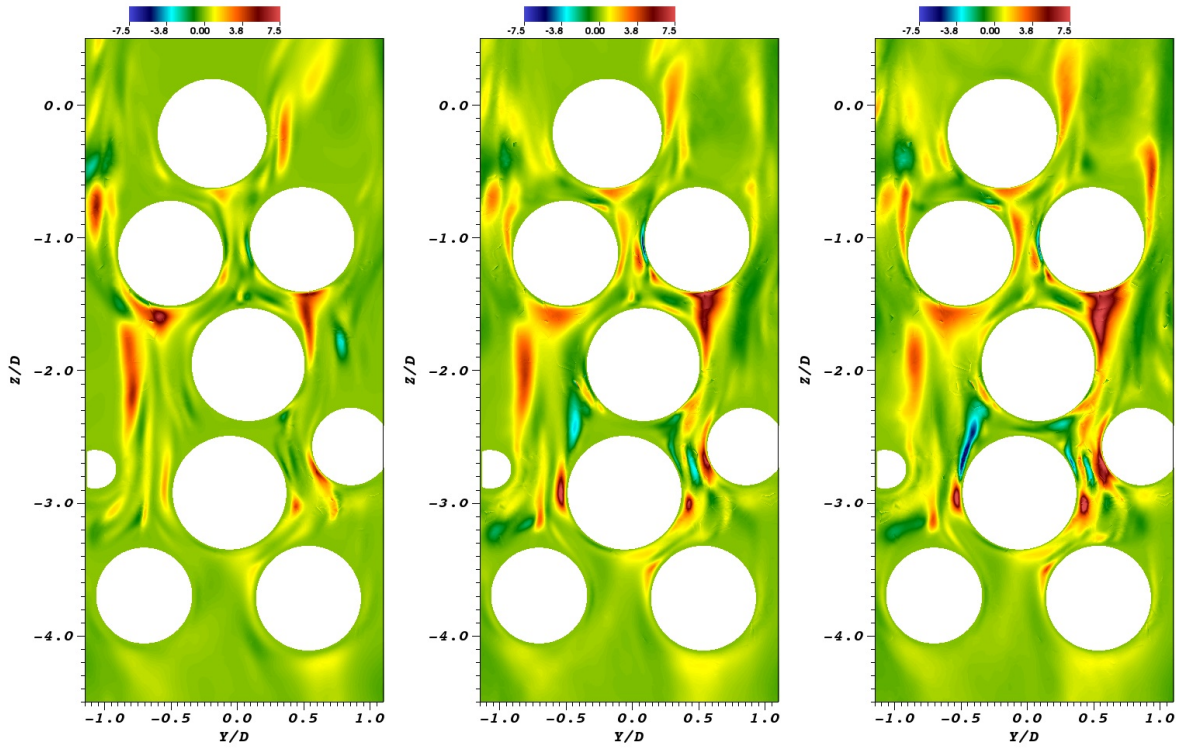

(a) Re=430 (b) Re=740 (c) Re=1050

Figure 4.23: Pseudo color field of P_{xz} for the the plane [-2.9D, Y/D, Z/D].

Reynolds number, Fig. Figure 4.21a, pockets of negative production are seen. Here TKE is taken out of the fluctuations and returned back to the mean flow. With increasing Reynolds numbers these zones decrease as more secondary flow paths are used and the influence of the averaged flow is decreased.

The transverse component of the production tensor, P_{xy}, is shown in Fig. 4.22. For the low Reynolds number, Fig. 4.22a, the little to no production is generated in the region leading to the contraction where the recirculation zone. As the Reynolds number is increased, Fig. 4.22b, we see the flow starting the accelerate to this region. as the flow is diverted around the bottom sphere a local increase in both the minimum and maximum is seen. As the flow is being accelerated, the larger increase in negative production is seen as energy is taken from the recirculation zone and added to the mean flow. Finally, we see an even larger increase as the Reynolds number is increased, Fig. 4.22c. The larger magnitudes on production is that allows for the smaller circulations

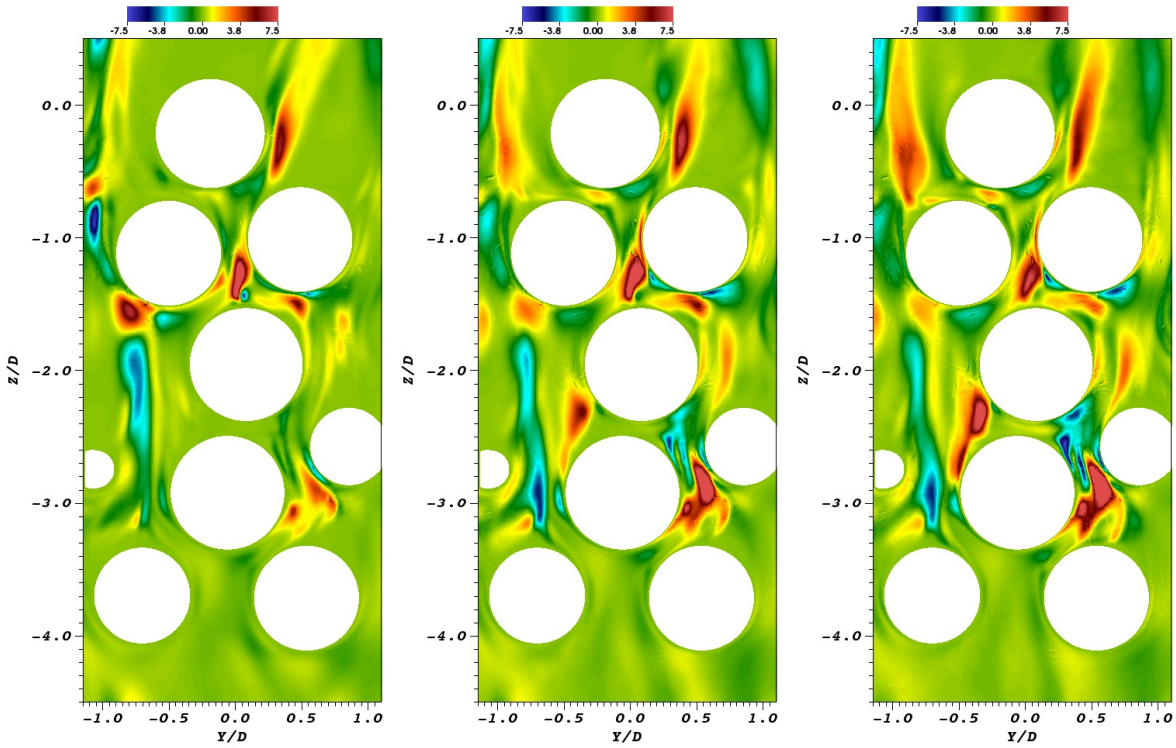

(a) Re=430 (b) Re=740 (c) Re=1050

Figure 4.24: Pseudo color field of P_{yz} for the the plane [-2.9D, Y/D, Z/D].

zones to develop in Fig. 4.15c as energy is extracted from the mean flow and added to the eddies.

The out-of-plane components, P_{xz} in Fig. 4.23, shows fairly consistent results. Unlike the results from Fick. [1], where these components had smaller magnitudes than the diagonal components, the random case‘s magnitudes are similar to the in plane‘s. This means that due to the random structure the flow has strong lateral components that add to the production as it is decelerated and diverted around the spheres. These increases are mostly seen on the downstream surfaces of the pebbles. As the Reynolds number is increased, Fig. 4.23b, the magnitude increase between the smaller pebble regions. This is emphasized in the highest Reynolds number, Fig. 4.23c as the flow can detach in between smaller gaps. With more lateral flow available the low-velocity zone seen is filled with smaller eddies.

The in-plane diagonal component, P_{yz} in Fig. 4.24, once again shows maximized magnitudes in the flow separation and shear layers behind pebbles. These magnitudes increase with an increase

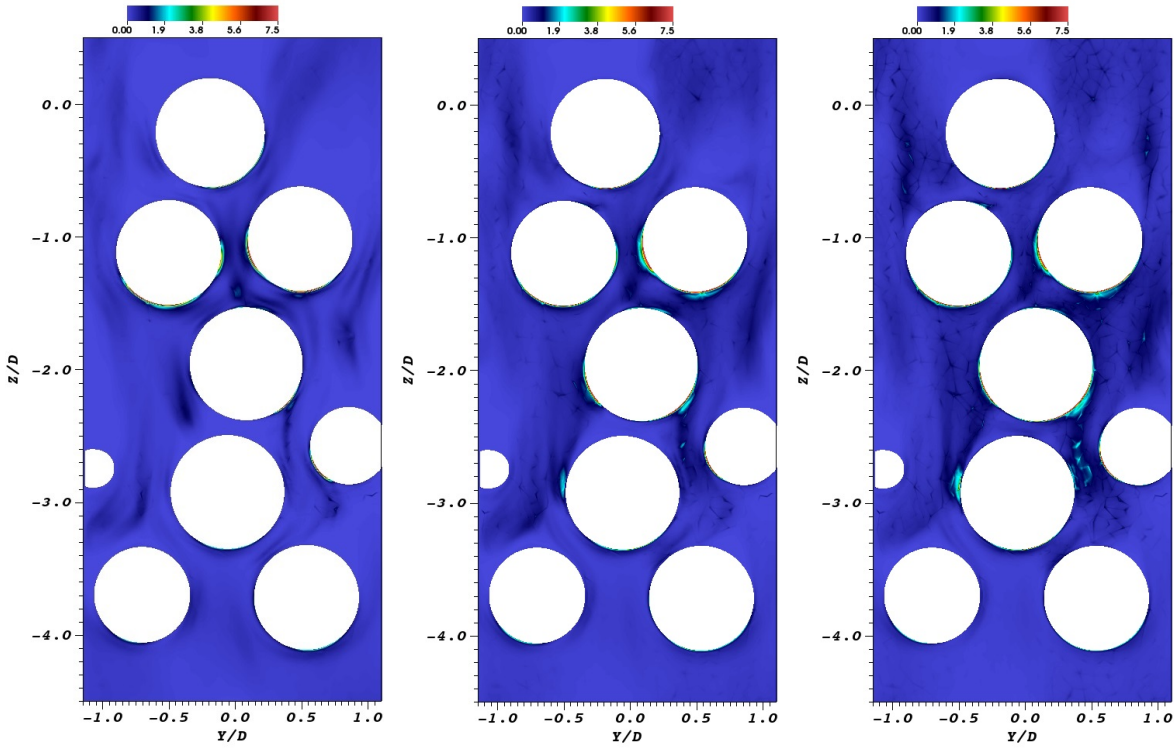

(a) Re=430 (b) Re=740 (c) Re=1050

Figure 4.25: Pseudo color field of ϵ_{xx} for the the plane [-2.9D, Y/D, Z/D].

in the Reynolds numbers. From these planes, the complex flow patterns through the random packed pebble bed are emphasized. The same trends, as seen in Fick [1], where an increase in magnitude in the flow separation and shear layers are observed. Due to the orientation of the plane, the pebbles and the flow through these pebbles, the structures exist in plains containing different normal vectors.

For the in-plane diagonal component of the TKE dissipation tensor, ϵ_{xx} in Fig. 4.25, the highest dissipation is seen on the upstream surfaces of the spheres. For the lowest Reynolds number, Fig. 4.25a, little dissipation is seen in the inter pebble regions where the flow is predominantly driven by the mean flow. The highest dissipations are seen where the flow hits the upstream surface and is then forced to change direction. For the intermediate Reynolds number, Fig. 4.25b, the regions of dissipation do increase in size, but remains concentrated to the upstream surface of the spheres. As the effects of the mean flow is decreased and more secondary flow paths utilized, some dissipation

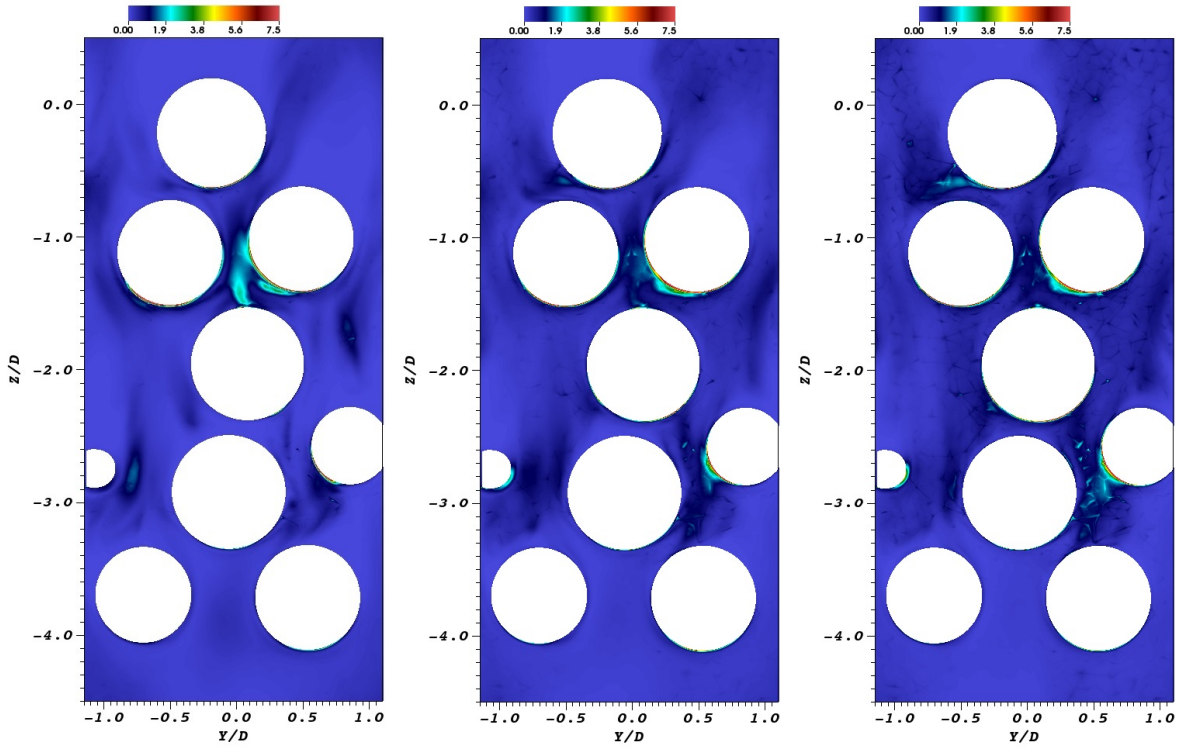

(a) Re=430 (b) Re=740 (c) Re=1050

Figure 4.26: Pseudo color field of ϵ_{yy} for the the plane [-2.9D, Y/D, Z/D].

occurs in the inter pebble regions close to the shear layer.

For the lateral component of the TKE dissipation tensor, ϵ_{yy} in Fig. 4.26, a similar trend as for the in-plane component are seen. The regions of highest dissipation are located on the upstream surfaces of the pebbles and the regions increase as the Reynolds number is increased from low, Fig. 4.26a, to high, Fig. 4.26c. It is noted that for the region downstream of the recirculation zone a small high dissipation region exists in the recirculation zone of the pebble in the $Z = -2.0D$ plane. As the Reynolds number increases this region decreases. For the higher Reynolds numbers, the high dissipation does creep up the downstream surface to closer to the pebbles equator.

For the streamwise diagonal component, ϵ_{zz} in Fig. 4.27, a similar trend as in the production is seen. Here the regions of higher dissipation follow the shear layer. For the low Reynolds number, Fig. 4.27a, the mean driven flow paths can be clearly seen as there is little dissipation in the wakes of the spears and inter pebble region. The largest dissipation is in the sheer layer of the pebble that

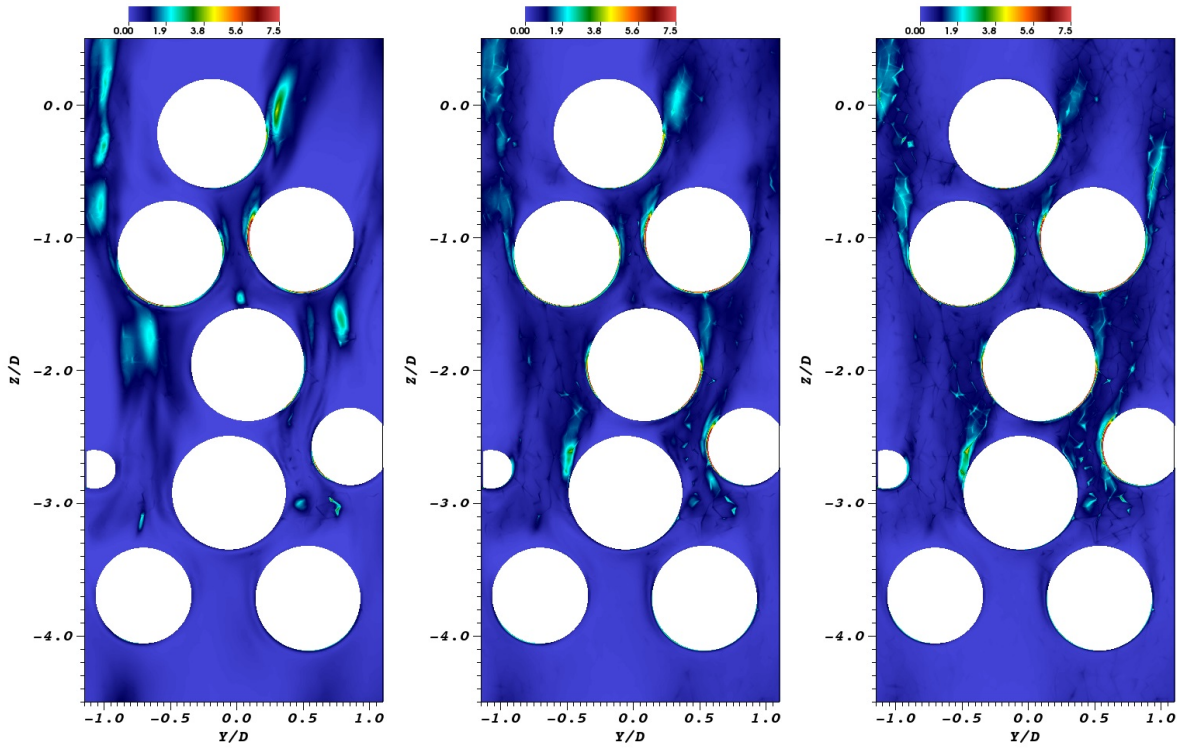

(a) Re=430 (b) Re=740 (c) Re=1050

Figure 4.27: Pseudo color field of ϵ_{zz} for the the plane [-2.9D, Y/D, Z/D].

experience the bulk of the mean flow. Once again, as the Reynolds number is increased Fig. 4.27b, more flow separation is seen from pebbles in close proximity to others. This is a result of the flow utilizing more of the smaller flow paths. the general orientation of the shear layers can be seen in Fig. 4.27b and 4.27c.

For the off-diagonal components of the dissipation tensor, the magnitudes are less than that of the diagonal ones. It is also seen that regions of local minimum and maximum are generated on the surfaces of the pebbles. For the transverse component, ϵ_{xy} in Fig. 4.28, a decrease in local dissipation is seen as the magnitude of the bulk flow, Fig. 4.28a, is decreased with an increase in Reynolds number, Fig. 4.28c, in the flow path at $Z = -1.0D$. As the Reynolds number is increased regions of larger dissipation magnitudes are generated in the smaller flow paths region, as the bulk flow through them is increased. The dissipation in the bulk flow is roughly zero. With small magnitudes in the shear layers going to the recirculation zone.

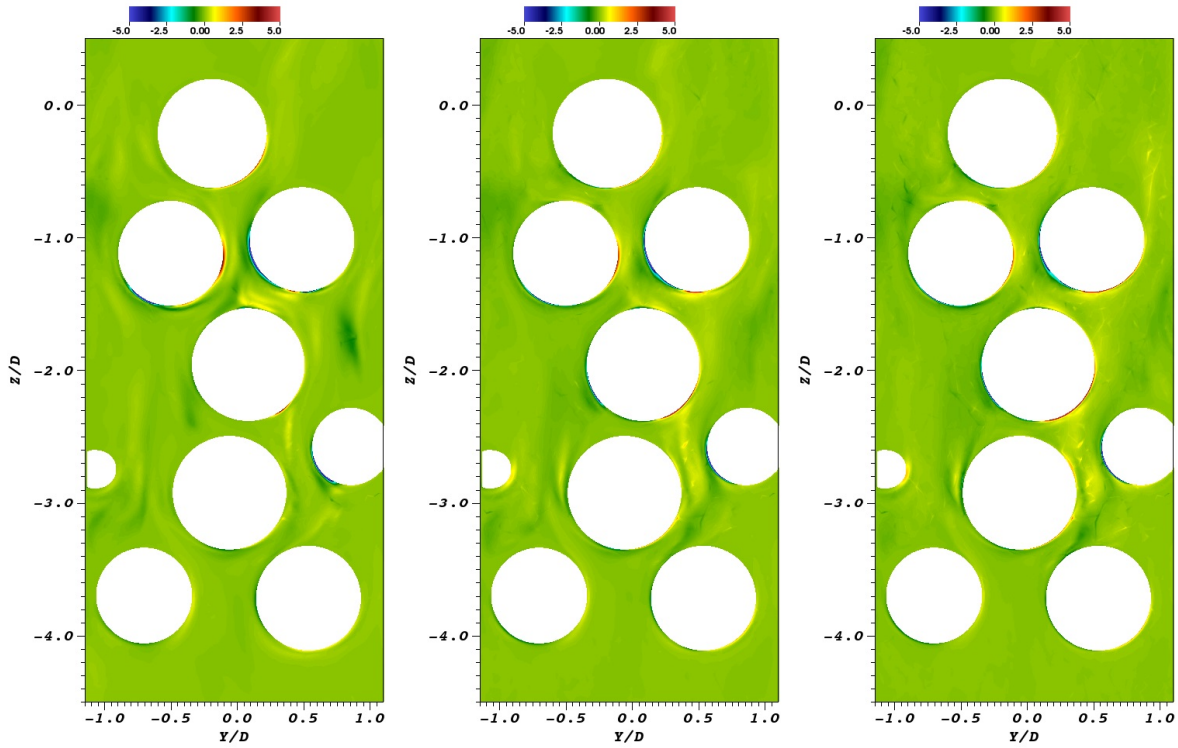

(a) Re=430 (b) Re=740 (c) Re=1050

Figure 4.28: Pseudo color field of ϵ_{xy} for the the plane [-2.9D, Y/D, Z/D].

For the out-of-plane components, Fig. 4.29, the local maximums are actually located on the downstream surface of the pebbles This is were the recirculation zones are present due to the flow detachment. The local minimums are seen on where the flow re-attaches the pebble surface. For the low Reynolds number, Fig. 4.28a there is strong out of plane flow in the inter pebble region between the upper pebbles. As the stream-wise mean flow velocity is decreased to the increase in Reynolds number, Fig. 4.28a, more lateral flow is seen and the increase in maximums are seen in on the right-hand side surfaces of the pebbles. A further increase is witnessed for the highest Reynolds number, Fig. 4.28c, indicating that cross and lateral flows starting being more relevant in the flow as the smaller bypass regions are being utilized. When looking at the bounding wall region, at the edge of the plotted domain, some positive dissipation is seen as the flow is redirected by the walls.

For the in-plane components, Fig. 4.30, is much lower than the other two components. This

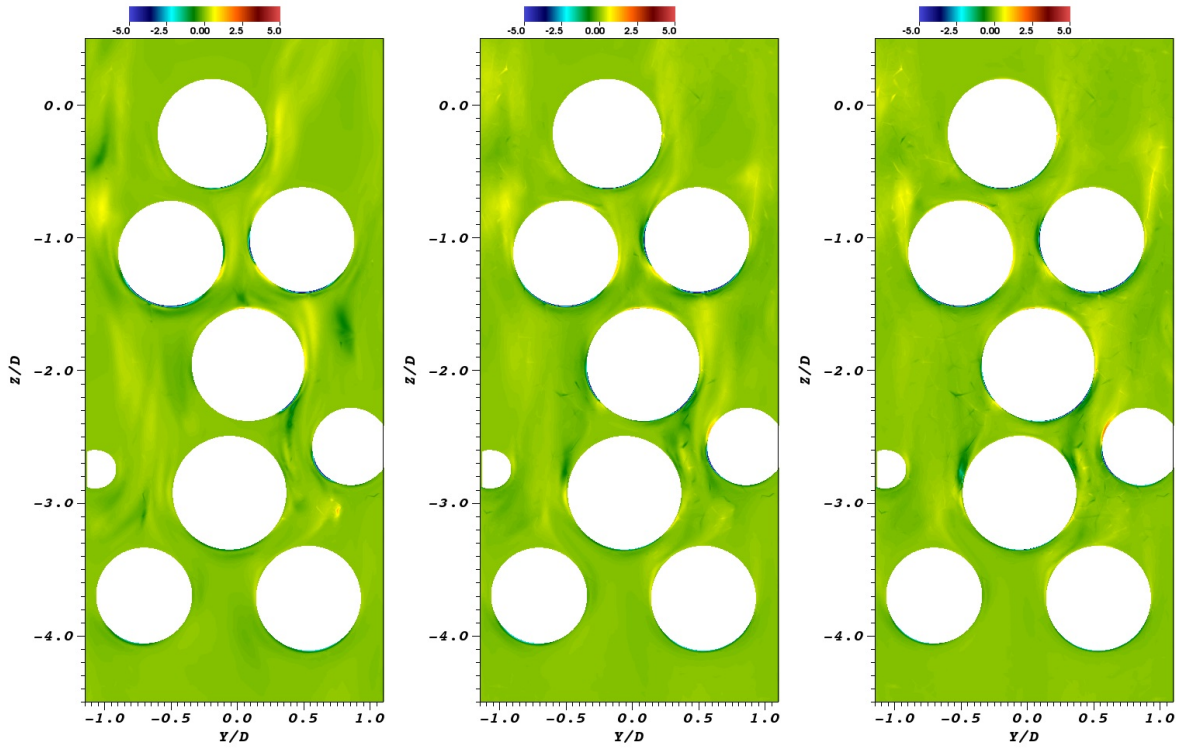

(a) Re=430 (b) Re=740 (c) Re=1050

Figure 4.29: Pseudo color field of ϵ_{xz} for the the plane [-2.9D, Y/D, Z/D].

is due to the fact that this velocity competent is directed into the bounding wall direction. this is expected as we have seen that the low-velocity recirculation zone is located. The flow in these plane tends to be slowed down as it approaches the wall due to the local wall effects. The local maximum and minimum are found as pairs on the pebble surfaces. In the inter pebble region, Fig. 4.29a, more local minimum regions are seen in the upstream surface of the pebbles. For the higher Reynolds numbers, Fig. 4.29a, these zones are increasing as well an increase in the shear later regions between the bulk and recirculation zones.

From the graphs plotted thus far, the complexity of the geometry and the interpretation of the flow is evident. Ideally one would want to utilize symmetry, as in the FCC cases of Fick [1], but the geometry does not allow it. The other option would be to have planes orthogonal to two pebble centers, to investigate the inter pebble region, but again finding these regions, due to the random packing is extremely difficult, if they exist at all in the near wall region.

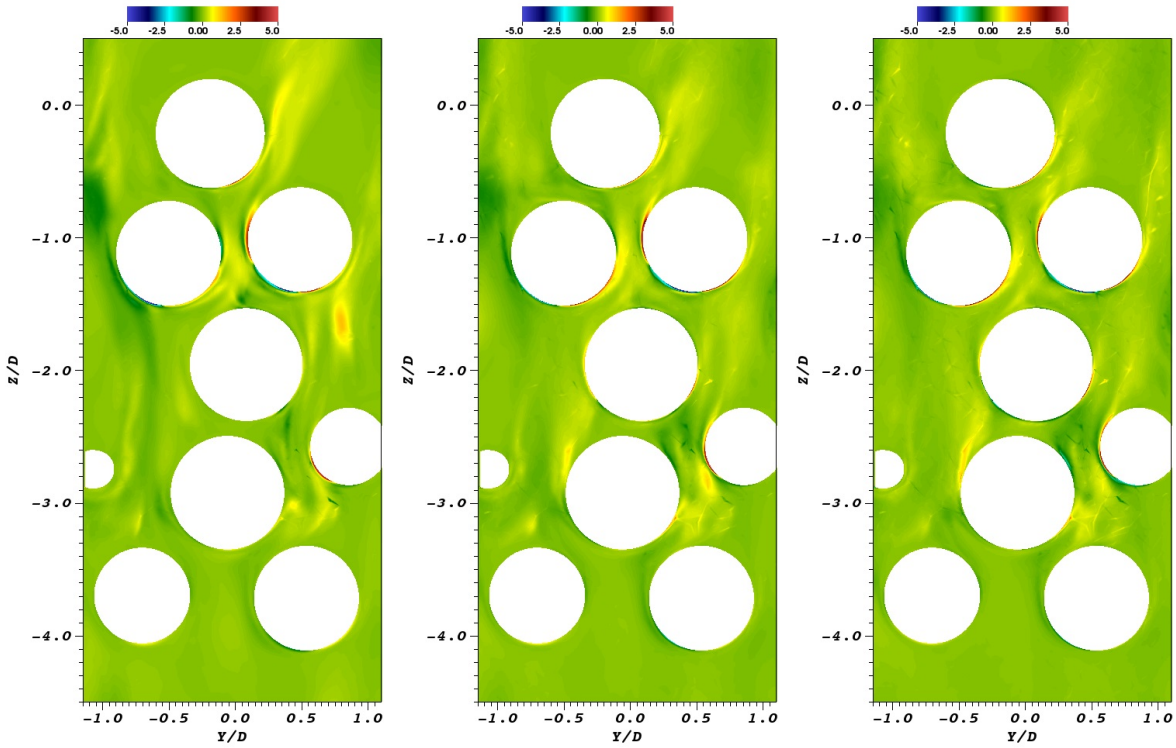

(a) Re=430 (b) Re=740 (c) Re=1050

Figure 4.30: Pseudo color field of ϵ_{yz} for the the plane [-2.9D, Y/D, Z/D].

From Eq. 2.20 it is seen that the triple product of the fluctuating velocity components is required in the calculation of the turbulent diffusion tensor. The nature of the triple product results in this term taking the longest to reach statistical stationarity. From the diagonal components of the term, Fig. 4.31, 4.32 and 4.33, it is seen that for the lowest Reynolds number the flow is stationary in the averaged time period. As the Reynolds number is increased the intermediate and high Reynolds number, which contains more fluctuations, seems to not be completely stationary. Even with that said, the structures and region of local maximum and minimum can still be distinguished. In the higher Reynolds number plots, non-physical flow features are seen. This is due to the numerical formulation of the SEM where velocity components are continues over element boundaries, where the derivatives are not. The orientation of the initial tetrahedral elements and the subsequent hexahedral conversion also affects these manifestations, depending on how the intersection plane intersects these elements.

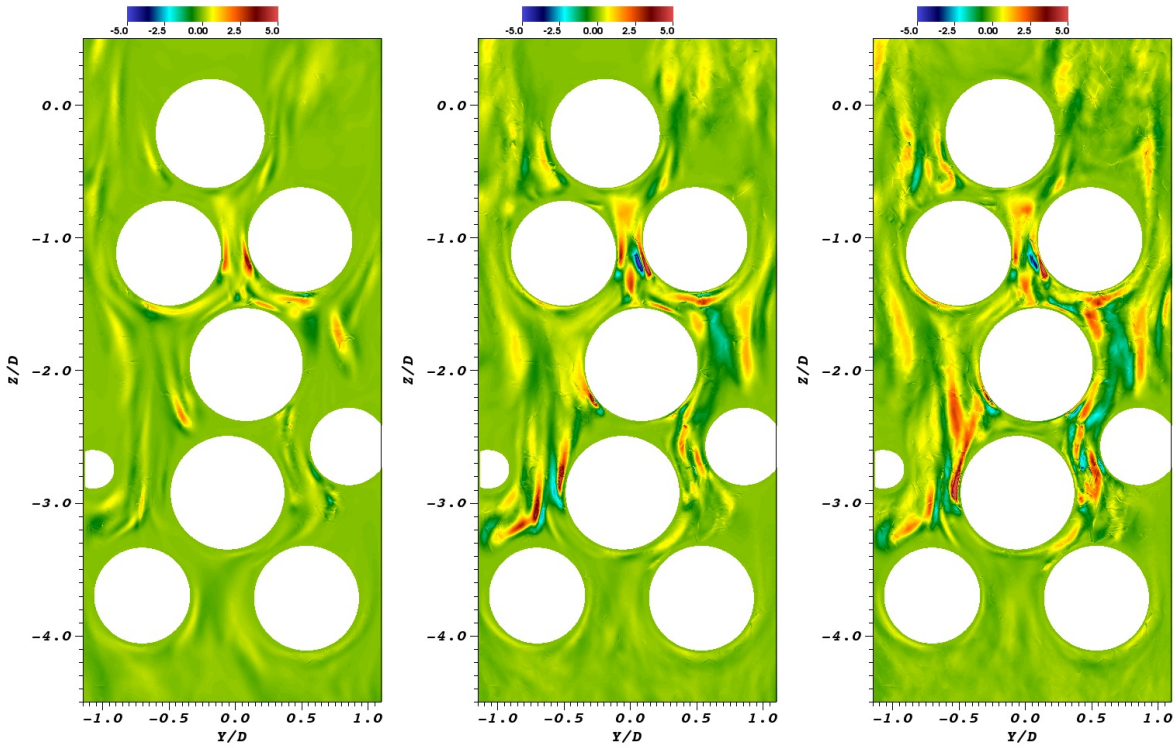

(a) Re=430 (b) Re=740 (c) Re=1050

Figure 4.31: Pseudo color field of turbulent diffusion tensor in the, x-component, for the the plane [-2.9D, Y/D, Z/D].

For the x-component, Fig. 4.31, the difference between the more viscous driven flow, Fig. 4.31a, and momentum driven, Fig. 4.31c is clearly seen. For the vicious driven flow, only small fluctuations exist as the bulk flow are concentrated to the larger flow paths. As the Reynolds number is increased, Fig. 4.31b the increase in the TKE diffusion is seen as more fluctuations are present in the flow. These flow structures are persistent with the flow separation in the shear layers. With more out of plane flow with the higher Reynolds numbers, the characteristics side-by0side positive and negative valued regions are seen. Indicating higher flow lateral flow rates propagating into the random pebble bed from the wall.

The transverse component, y-component Fig. 4.32, the same effects are seen. Here a large magnitude region is present in the inter pebble region of the low Reynolds number, Fig. 4.32a. There is also large magnitude region on the upstream surface of the pebble downstream of the

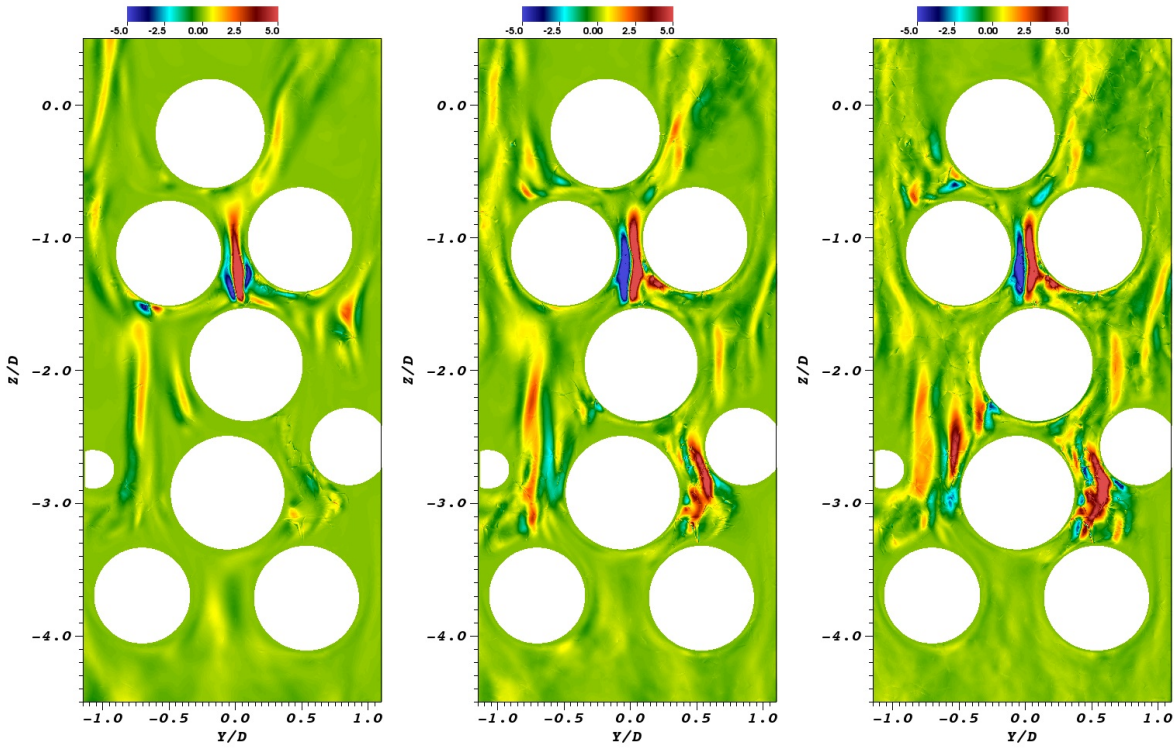

(a) Re=430 (b) Re=740 (c) Re=1050

Figure 4.32: Pseudo color field of turbulent diffusion tensor in the, y-component, for the the plane [-2.9D, Y/D, Z/D].

recirculation zone. As the Reynolds number is increased one can see more turbulent diffusion in the recirculation zone as smaller secondary zones are generated and the TKE is diffused in this region. This results in a decrease of the zone on the pebble surface for the increased Reynolds numbers, Fig. 4.32b and 4.32c. This is accompanied by the magnitude increase in the inter pebble region as the flow is accelerated. once again the characteristic side-by-side positive and negative zones are seen as the flow becomes more turbulent and secondary flow regions see more flow.

Finally for the streamwise component, z-component Fig. 4.33, some prominent structures arise. For the recirculation zone, the single side-by-side structured is seen for the low Reynolds number, Fig/ 4.33a. As the flow gets diverted around the top pebble high magnitude zones are also seen close to the wall was the flow is being split after separating from the pebble. As the Reynolds number is increased and the circulation zone shrinks, Fig 4.33b and 4.33c, more side-by-

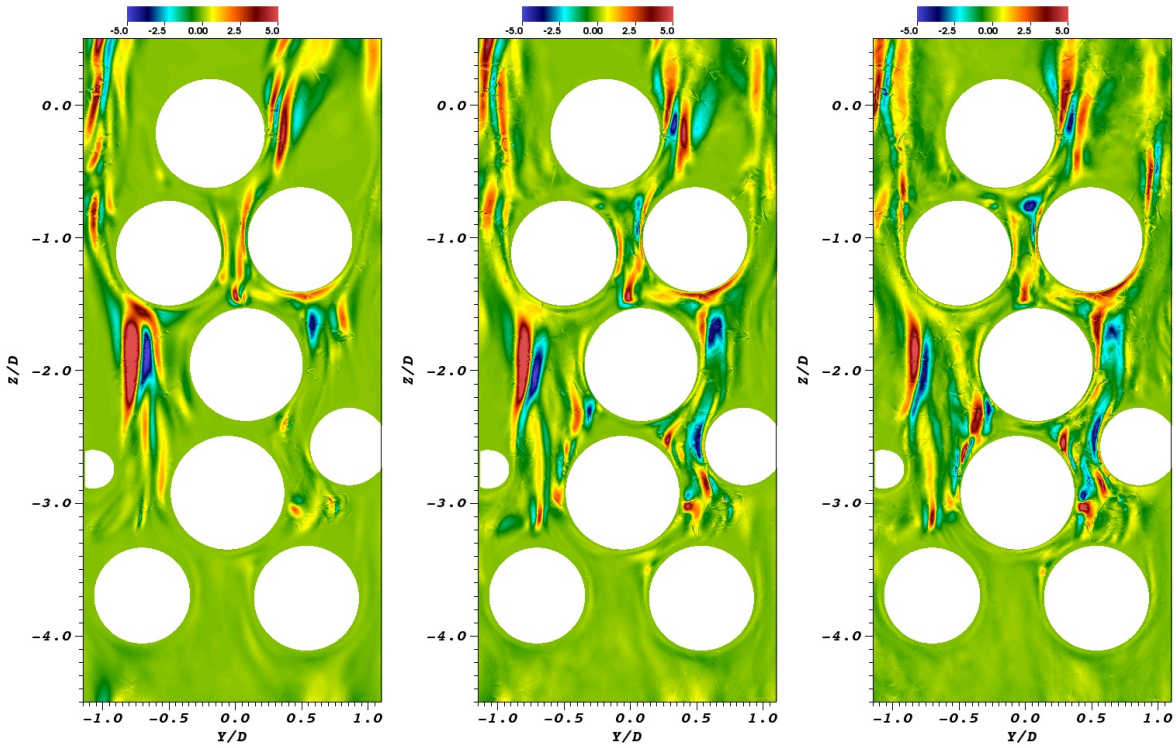

(a) Re=430 (b) Re=740 (c) Re=1050

Figure 4.33: Pseudo color field of turbulent diffusion tensor in the, z-component, for the the plane [-2.9D, Y/D, Z/D].

side structures form matching the increased number of secondary resuscitation zones seen in Fig 4.15c. This indicates more fluctuations in the transverse and later planes as the bulk mean velocity decrease to the secondary flows increasing. This can clearly be seen in the inter pebble region of the high Reynolds number, Fig. 4.33c as multiple side-by-side structures developed, indicating complex flow separation in the shear layer.

The viscous diffusion tensor is shown in Fig. 4.34. Due to the viscous action dominating in the boundary layer the figures focus on the inter pebble region. As the viscous term is most dominating in the boundary layer, we see it maximized here, close to the pebble surfaces. For the lower Reynolds number, Fig. 4.34a, the effects of the term is seen further from the surface as the flow is more viscous driven. As the Reynolds number is increased, the areas of local maximum decreases, but the magnitude remains the same. Only the x-component of the diffusion tensor is

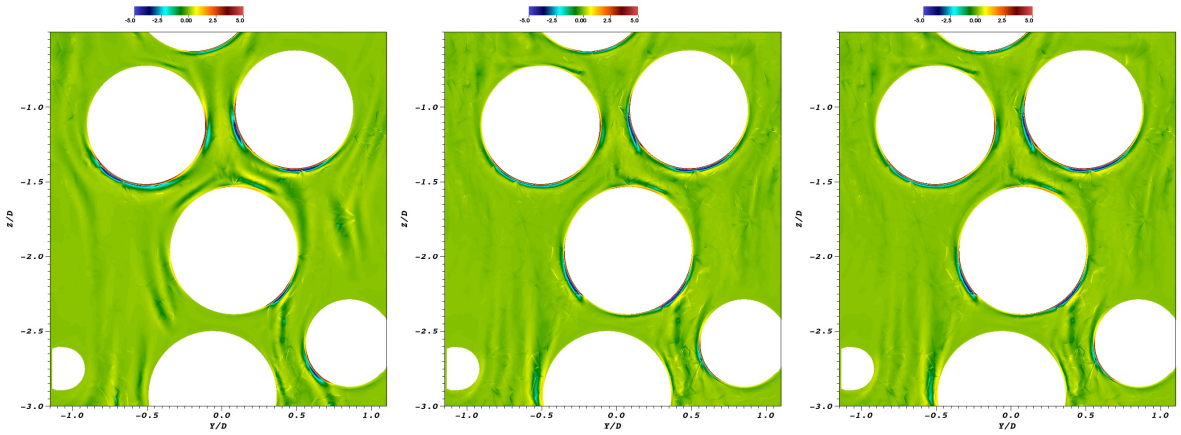

(a) Re=430 (b) Re=740 (c) Re=1050

Figure 4.34: Pseudo color field of viscous diffusion tensor in the, x-component, for the the plane [-2.9D, Y/D, Z/D].

plotted, but the y- and z-components have the same trend. Due to the evaluated Reynolds number being significantly lower than that of Fick [1], we see a tensor with almost zero magnitude in the main flow regions. The FCC case localized maximums and minimums were scattered in the free stream region as well.

4.3.3 Experimental cross-verification

Due to the nature of the random-packed pebble bed, no q-DNS data is available to do cross-verification as for the FCC case done by Fick [1]. The experimental work can be found in the work done by Nguyen [41]. The experiments were run co-current with the DNS study. Even though quantitative line out comparisons was not present, qualitative contour plots in the plane of interest were available. Figure 4.35 shows a side by side, pseudo-color plot of the experimental and DNS time-averaged results at the $Z = -2.285D$ plane.

Comparing the geometry from the experimental PIV and DNS study, the uncertainties in finding the pebble locations from the PIV planes, as mentioned earlier in the chapter, is evident. In the near wall region the pebble locations do match, the only difference is the pebble-pebble contact region, at $[-2.5D, 0.5D]$. When moving further into the domain the pebble located at $[-1.25D, -1.0D]$ seems to be higher positioned in the DNS than in the experimental set-up.

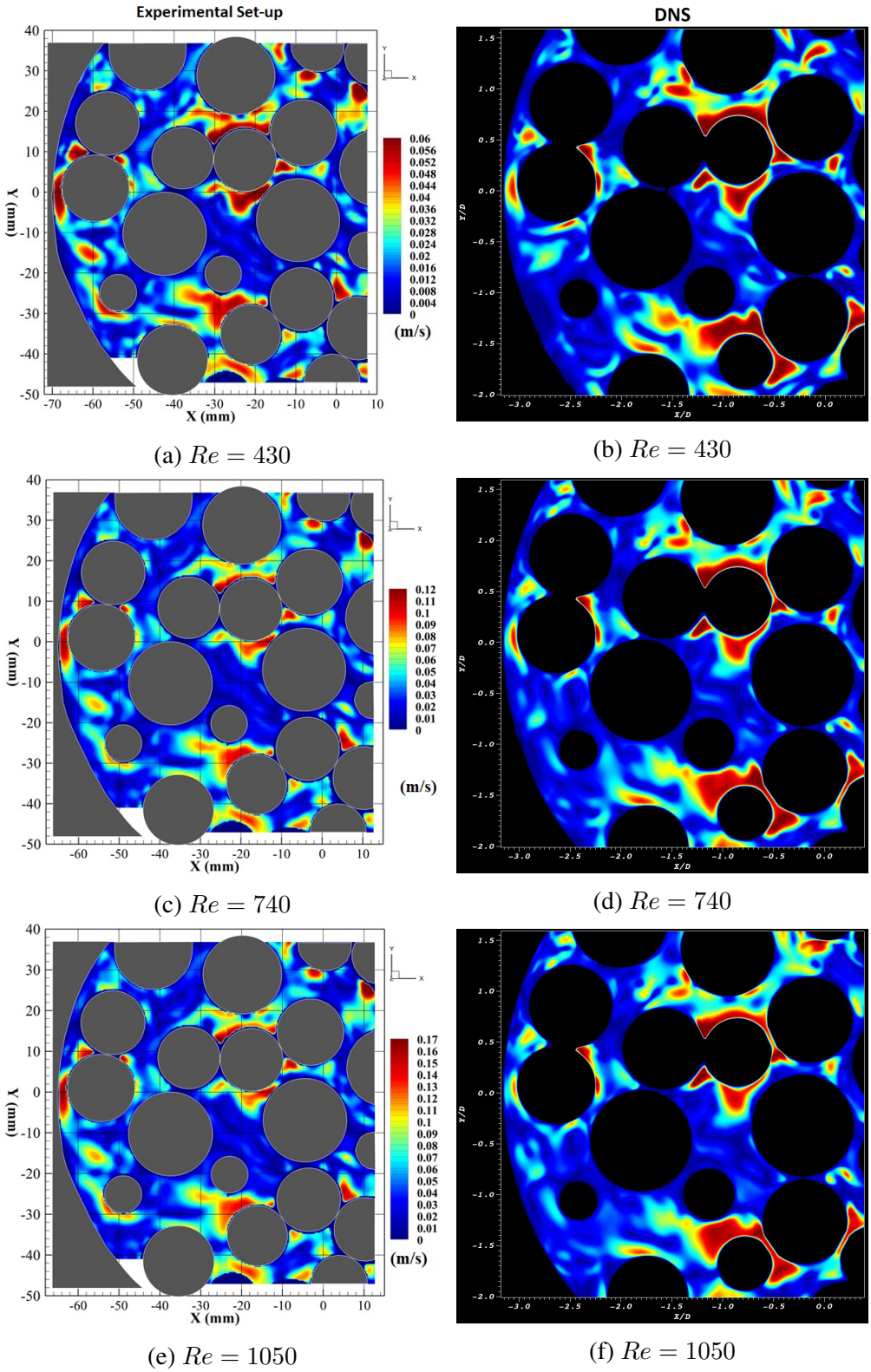

(a) $Re = 430$

(b) $Re = 430$

(c) $Re = 740$

(d) $Re = 740$

(e) $Re = 1050$

(f) $Re = 1050$

Figure 4.35: Qualitative comparison between experimental, reprinted from [41] (left, averaged for $11s$) and DNS study (right, averaged for $115CU$) at $Z = -2.285D$.

Some further minor differences can be seen where the close proximity pebble assumption during the moving boundary method was applied. These uncertainties are due to the numerical error in the determination of the pebble locations and meshing strategy. Other unquantified uncertainties such as experimental vibrations during operation and the subsequent pebble movement can only be quantified once the experimental results are published and available for comparison.

For the flow comparisons, we see the same structures in the DNS as in the experimental set-up. It should be noted that the snapshot shown for the experimental set-up was only averaged over 11 seconds, where the DNS study was averaged over 115 CU. For the DNS results, the statistics were not converged after 11 CUs of averaging. For the near wall region, where the two pebbles are touching, it is seen that the flow does not penetrate the all the way to the contact point, as the wall and viscous effects stop the flow. This is seen for all three experimental Reynolds numbers. For the DNS where the pebble-pebble contact is approximated as a cylindrical contact the size of the boundary layer, the same effect is seen. This gives confidence that pebble-pebble contact approximation is satisfactory. For the close proximity approximation, larger flow paths are present in the DNS, due to the element movement being suppressed here. These larger flow paths to allow some flow through and some higher velocity differences are seen where these approximations are made.

For the low Reynolds number, Fig. 4.35a and 4.35b, the magnitudes between the experiment and DNS are fairly similar. As the Reynolds numbers are increased, Fig 4.35c to 4.35e, the DNS results do show lower values in the near wall region. This can be attributed to the experimental averaging time. For the low Reynolds number, the 11 seconds averaging window seems to be sufficient, but as the Reynolds number is increased and the fluctuations increase more averaging time is required for these statistics to converge. This trend was seen in the DNS as the lower Reynolds number‘s first and second order statistics converged in less CUs that the higher ones.

4.4 Conclusion

In this section, the DNS analysis for the flow through a randomly packed pebble bed was shown for three different experimental Reynolds numbers. The new meshing methodology used

to mesh the randomly packed pebble bed was discussed. The spatial and temporal resolution of the mesh was tested to the Kolmogorov time and length scales. From the DNS conformance test, an adequate spatial discretization where chosen that yielded the best resolution and computational effort. This served as a rude grid convergence study as performing a complete one would have been computational to expensive. This was done on the bases of Fick [1] that showed that the Kolmogorov scales can be used as an explicit test of DNS conformance.

Due to the random packing nature, no temporal instabilities were found in the flow and the turbulence statistics converged after 23 FTTs. As no instabilities were found, POD was not implemented as an analysis tool. The analysis of the flow was focused on a region closes to where the PIV measurements were taken to allow for quantitative comparisons once experimental data was available. In this region, a low-velocity recirculation zone was found in the wake of a pebble close to the wall. The TKE budget terms were investigated and discussed in this region for all three Reynolds numbers.

Lastly, a qualitative comparison between the DNS and available experimental data was done. Due to the complexity and difficulty of the experimental, some discrepancies between the experimental and DNS geometry was observed. Even with the minor geometric deviations, the same flow structures were observed in the majority of the investigated plane.

5. NUMERICAL EXPERIMENT III: RANDOM PACKED PEBBLE BED - REDUCED DOMAIN

This section corresponds to the final work done for the dissertation research. A large amount of computational resources required to perform DNS on the random packed pebble bed was highlighted in the previous chapters. The work presented in this study was to investigate how simplifying the geometry would affect the flow dynamics and TKE of the random packed pebble bed in the near wall region. The goal was to investigate the validity of employing geometric symmetry as exploited in other CFD studies, such as PWR fuel assemblies and prismatic block cores, to reduce the computational cost. To the authors best knowledge, no literature existed that perform this study on random packed pebble bed geometries. Due to the random nature of the pebble bed, the effects of decreasing the domain is unknown.

The insight gained from the previous study‘s practical consideration regarding the size and associated computational burden was the drive for the study. For practical reactor simulation as many near wall pebbles need to be simulated in the stream-wise the direction, while keeping the azimuthal angle as small as possible without introducing significant error to the results. This will decrease the computational burden required while still retaining accuracy.

This section follows the same layout as the previous with a background, methodology, results and discussion and ended with a conclusion.

5.1 Background

It was found, that most of the literature pertaining to the turbulent flow through pebble beds were focused on idealized structured packing away from bounding walls, i.e in the center of reactor cores away from the reactor vessel walls. A series of papers where published by Shams et al. [9, 31, 38, 11, 42] on structured pebble beds as well as an LES study on a random packing [10]. Further studies were that of Hassan [32, 12] and few thesis [1, 18, 43, 44]. Only limited experimental work has been found such as the work done by Nguyen [45, 41].

Literature investigating the effect of wall effects on the flow over bluff bodies were singled out to a fundamental investigation. Some experimental work include [46], where some single sphere [47], two spheres [34] and hemisphere [48] investigations were performed. Fick [1] expanded on this by having an expanded FCC case that is wall bounded at one side. The results from these works indicate the effect that the wall has on the flow. Most of these flows assumed periodic flow conditions for the non-bounded faces.

These studies showed that low-velocity recirculation regions from behind spheres. These patterns are repeated in structured cases. In practical reactors systems, such stagnation regions would have reduced convective heat transfer, resulting in significant temperature gradients on both the fuel and bounding wall. Thermal fatigue can cause decreased safety margins in these regions, that can ultimately effect long term operations.

To develop DNS flow data for an entire pebble bed reactor, with current computing resources available, is impossible. Having done DNS on a full segment of the experiment, it poses an ideal opportunity to see how decreasing the domain and employing symmetry assumptions would affect the flow fields. This will allow confidence in modeling more pebbles in the stream-wise direction allowing to better quantify the wall effects in random packed pebble cases. This will also provide reference data that can be used in lower fidelity RANS based simulations.

This study presents how reducing the domain to a quarter segment of the full geometry affects the DNS and TKE results of the random packed pebble bed.

5.2 Methodology

This section will discuss the methodology used during the study. The case outline and simplification steps made will be listed, along with flow and boundary condition information. The computational aspects of the simplification will be explained. The method of how the data was interpolated will be viewed. How the simplification affected the flow and TKE will be highlighted before the full case TKEs are given.

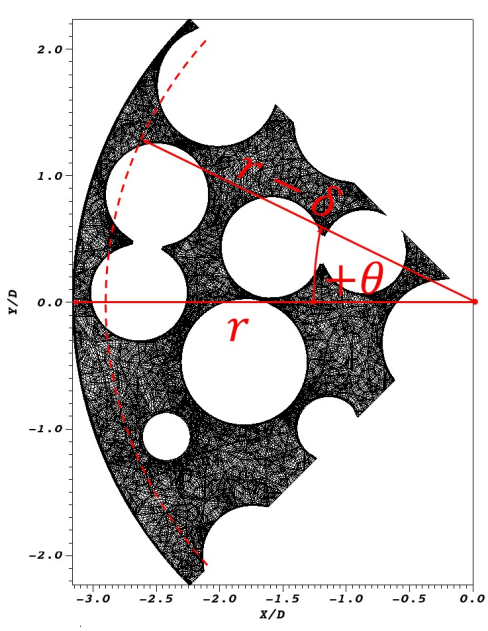

(a) Sectional plain at $Z/D = -2.285$ showing the quarter domain.

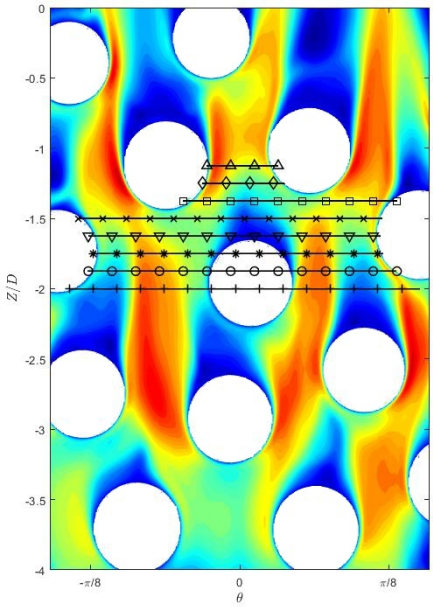

(b) Two-dimensional view of the interpolation lines distributed at $\delta = 0.125D$ from the wall.

Figure 5.1: Planar slices to show positions of interpolation lines.

5.2.1 Case Outline

The geometries presented in this section is the same random pebble configuration treated in the previous section. The computational domain was reduced to a quarter of the full domain by removing a $90°$ wedge from the full geometry. The cut was made $\pm 45°$ from the negative x-axis, resulting in a domain size of $[x/D \leq 0, -3.15 \leq y/D \leq -3.15, -5 \leq z/D \leq 1]$ as seen in Fig. 5.1a. The same meshing strategy and assumptions have been applied to this case as in the full experimental case. This resulted in a mesh resulting in $278,738$ elements, which is roughly four times smaller than the full geometry.

The case was restarted by interpolating the developed flow of the full case over the newly developed mesh. Due to the randomness of the pebbles periodic boundary conditions were not suitable for this case. It was chosen to apply zero-slip wall boundary conditions to the new cut planes. The

flow was allowed to develop for 5 FTTs before the mesh was tested for DNS requirements. As expected the quarter case, meshed with the same parameters as for the full case, showed the same trend for the Kolmogorov scales plotted in Fig. 4.9. The same polynomial order, $N = 5$, was thus selected for the simplified case.

Besides applying a zero-slip wall boundary condition to the cut plain, a zero-gradient symmetry condition was also applied for a different case. In this symmetry case the momentum equation diverged in the wake of pebbles close to where the two symmetry plains intersected at $[0, 0, Z/D]$, due to the high curvature of the pebbles in the close proximity on the symmetric boundary condition, combined with the recirculation zone in the wake of the pebbles. To make the simulation stable the cut plane was split into two different boundary conditions. All the elements at $[x/D \geq -0.1]$ was set to a zero-slip wall boundary condition, where the rest of the cut plain was set to zero-gradient symmetric. This assumption allowed the flow to be developed, the same as the wall case, without the results diverging. With this case being the same mesh, but different boundary conditions, the Kolmogorov scales remains essentially unchanged.

5.2.2 Interpolation

From the full case, the complexity of representing the results was highlighted. For this comparison, it was decided to investigate the results on radial slices selected at a set distance, δ, from the wall, as seen in Fig. 5.1a. The radial slice was dived into 1258 and 3200 equally spaced data collection points over the arch and streamwise lengths respectively. This a resolution of 4 million collection points over the radial surface. The angle, θ, is chosen as positive in the clockwise direction, measured from the negative x-axis.

Figure 5.1b shows the positions of the interpolation lines along the arc length in the near wall region. The arc is taken at $\delta = 0.125D$ from the wall. The rationale for the distance from the wall will be discussed in a later subsection. The lines were chosen around the pebble in the center of the plane shown in Fig. 5.1b. The first line was chosen at $Z = -2D$, which corresponds to roughly the center of the particular sphere. From there the lines were placed at $0.125D$ increments in the streamwise direction. The radial distribution of the lines was kept between $-\pi/8 \leq \theta \leq \pi/8$, or

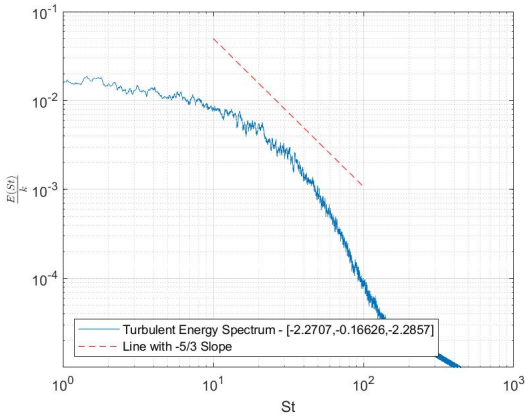

(a) Line01

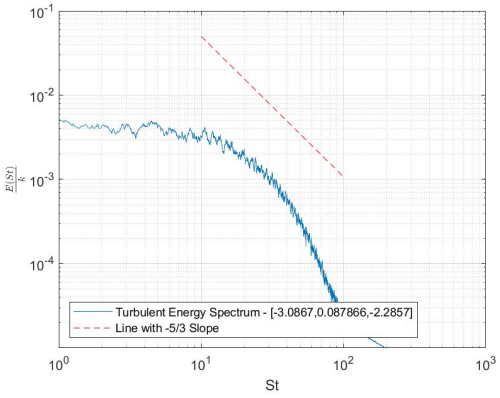

(b) Line08

Figure 5.2: Power spectrum taken in the center of the line location at $[Z/D = -2.285]$.

until a line intersected another pebble surface.

5.2.3 Computational Consideration

The simplified domain consisted of $278,738$ spectral elements. Based on the scoping runs from the full random packed DNS study, a polynomial order of $N = 6$ was chosen for the production run. This resulted in a domain of roughly 34 million collection points.

The temporal stepping was done by employing a characteristics scheme, which allowed for a stable time intergeneration with a CFL number of 3. This time step was smaller than the minimum calculated Kolmogorov time scale for the case. The power spectrum of the streamwise fluctuating component, u_z, which is normalized by the TKE, is for the inter pebble gap in a near and far wall region is plotted in Fig. 5.2. From the two power spectrum plots, it is observed that the energy content of the high-frequency fluctuations are negligible at $St \geq 500$, confirming that the case conforms to the DNS requirements.

Both the wall and symmetric boundary condition cases utilized the same restart, averaging and statistical stationarity routines discussed in the full DNS case. The cases were developed for 35 CUs before averaging were done. The cases were averaged for a total of 115 CUs, at $N = 5$, and was found that the turbulence statistics showed adequate time independence after the averaging

Table 5.1: Computational Parameters to calculate Kolmogorov scales for simplified Random packed pebble bed with symmetric boundary conditions, Re = 1050.

	Polynomial Degree		
Parameter	5^{th}	7^{th}	9^{th}
Time Step length	1×10^{-4}	5×10^{-5}	2.5×10^{-5}
GLL points	34.84×10^{6}	60.20×10^{6}	142.71×10^{6}
Nodes (Cores)	$512(8192)$	$1024(16384)$	$2048(32768)$
Core Hours/FTT	98.30×10^{3}	461.32×10^{3}	1.98×10^{6}

time. Table 5.1 shows the computational expenses of the highest Reynolds number of the simplified case. For both the wall and symmetry boundary conditions the calculated core hours were almost identical. When comparing the full and simplified case the decrease in core hours, although not exactly 1/4th, is still witnessed. Not only was the simplified case capable of running on fewer nodes, but due to the smaller node allocation, it could be run more frequently due to the way the ALCF job scheduler worked.

5.3 Results and discussion

The following subsection discusses how the distance of the radial plain was selected. The effects of the simplified geometry on the first-, second-order statistics and TKE‘s are then evaluated. The section is then finished by plotting the interpolated turbulence statistics and TKE in the near wall region.

5.3.1 Plain selection

From the previous chapter, the complexity of the geometry was highlighted. In order to better quantify the turbulence statistics, the DNS data has to be visualized in a different manner. The analysis of the effects of the domain simplification will be done on a radial basis, as shown in Fig. 5.1a. To get a better perspective of the geometry, different radial slices were taken. The distance of the slices was measured from the bounding wall. Figure 5.3 shows three slices at $\delta = 0.125D, 0.625D$ and $1.125D$, resulting in the near wall region, half a pebble and a full pebble

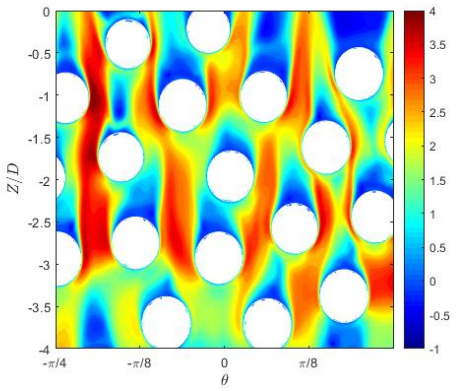

(a) $\delta = 0.125D$

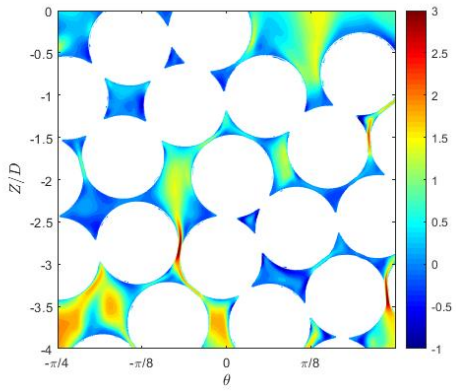

(b) $\delta = 0.625D$

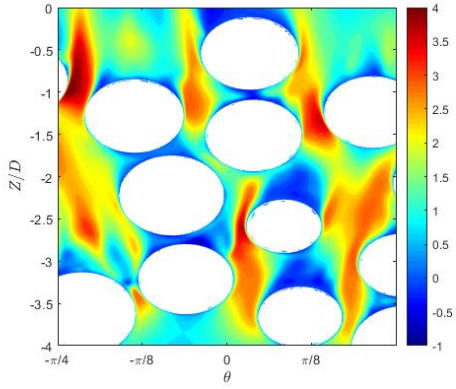

(c) $\delta = 1.125D$

Figure 5.3: Psuedo-color of the averaged stream wise velocity, $\langle u_z \rangle$, for $Re = 1050$ to show the radial distribution of pebbles at different distances from the bounding wall.

diameter from the wall respectively. These radial slices give a better overall prescriptive of how the spheres are arranged in the near wall region, as well as identifying possible patterns in the random packed geometry.

For the near wall region, Fig. 5.3a, clear large flow paths are seen as local voids are created where the pebbles rest against the wall. As the focus is moved further away from the wall, Fig. 5.3b, the packing of the spheres are closer as the experiment was shaken to remove internal voids. This results in fewer direct flow paths and more pebbles within close proximity can be seen. The close-proximity approximation used when meshing the spheres in close proximity can be better seen as all the pebbles are intersected approximately at the same radius. Moving a full pebble

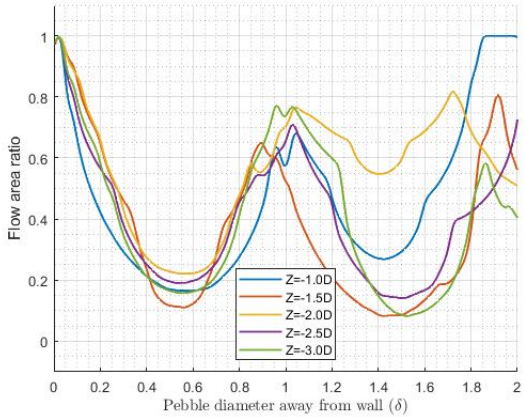

(a) The ratio of flow area to total arch length as the distance from the wall is increased.

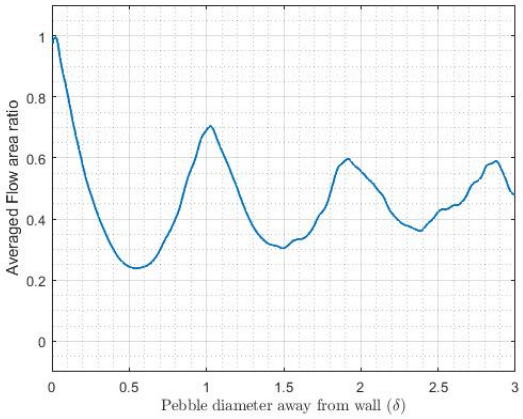

(b) The averaged ratio of flow area to total arch length as the distance from the wall is increased.

Figure 5.4: Porisity analysis of the random packed pebble bed.

diameter away from the near wall region, Fig.5.3c, the inter pebble regions open up to larger cavities, but due to the angle, fewer spheres are present at this distance.

Due to the random packing nature of the pebble bed finding repeating patterns are challenging. In order to see if the packing of the pebbles possesses any hidden repeating patterns, an effective flow length was calculated as a function of the distance from the wall, Fig 5.4a. This ratio was calculated by determining the total fluid region, along with the length of the arc at a set distance from the wall, divided by the total length of the arc. This was done for $-\pi/4 \leq \theta \leq \pi/4$ and $0 \leq \delta \leq 2$. A value of 1 corresponds to the arc containing only the fluid flow, to 0 containing only the pebble. Figure 5.4a shows the ratio for different locations in the stream-wise direction. From this, it is seen that on the wall, $\delta = 0$, the ratio is approximately unity as the pebbles-wall interaction approximation was used. As we move further from the wall all the Z/D locations decrease steadily, with roughly the same gradient and same minimum. This indicates that the distribution of the pebbles against the wall is roughly uniform, but as the distance from the wall is increased, the packing truly becomes random.

Du Toit [49] found that calculating the averaged porosity of a PBR and plotting it as a function from the wall a dampened oscillatory function is witnessed. He observed three distinct regions, the

near wall region with large fluctuations in the porosity that is about two pebble diameters from the wall. The transition region where the fluctuations are less as the packing becomes more random for the next 3 pebble diameters. Finally, the bulk region where the porosity approaches a fixed value and almost uniform structure. When calculating the averaged porosity of the experimental bed, Fig. 5.4b, the same dampened oscillatory behavior is seen as was observed by Du Toit [49]. With the experimental set-up only being 6 pebble diameters in diameter it is seen that the center of the experiment is in the transition zone and no bulk packing structure exists.

For the remainder of the study and this chapter the near wall region at $\delta = 0.125D$, will be investigated. This allows for the longest arch length and enough spheres from the cut plane to see how the simplification propagates through the domain. The focus will also be directed to the highest Reynolds number, $Re = 1050$, as it was found that the higher Reynolds number does not only have more cross and lateral flows, but also will be closer to conditions actually found within pebble bed reactors.

5.3.2 First-order statistics

For the first order statistics, all the cases were averaged for the same averaging window after the flow was developed. Figure 5.5a, shows the averaged stream-wise velocity plot, $\langle U_z \rangle$, for, $Re = 1050$ at $\delta = 0.128D$. This corresponds to a radial porosity of 0.78. From here the low-velocity recirculation zones, in the wake of the pebbles can clearly be seen. Two distinct packing structures are visible, at $\theta \geq 0$ the pebbles close to the wall is mostly staggered, where $\theta \leq 0$ a more in line arrangement can be seen. Large recirculation regions are seen around this flow path. From this clear large flow areas of high averaged streamwise velocity is seen. For the staggered configuration, the high velocities are only seen when the flow is accelerated around the pebbles.

Figures 5.5b and 5.5c, shows the difference in averaged stream-wise velocity, the full case results minus the simplified case results, for the wall and symmetric case respectively. For the wall case, Fig 5.5b, the largest difference is seen close to the edges of the domain, with smaller variation as the distance from the wall is increased. The largest difference is seen at $\pm\pi/4$, where the wall boundary is located. This is seen where pebbles being intersected by the wall creates small flow

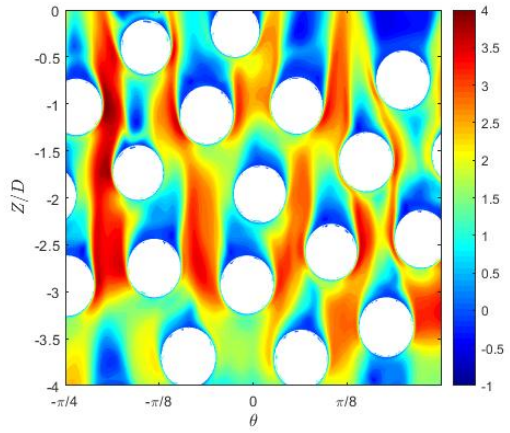

(a) Full geometry

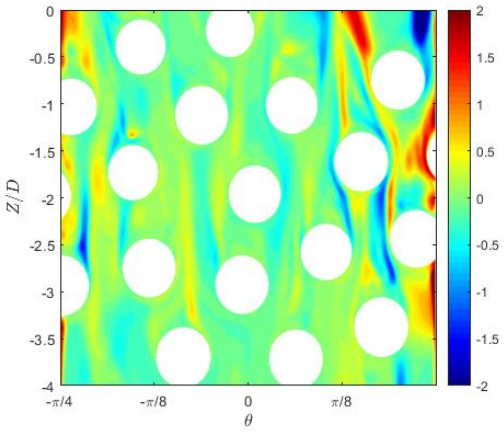

(b) Difference between full and wall case.

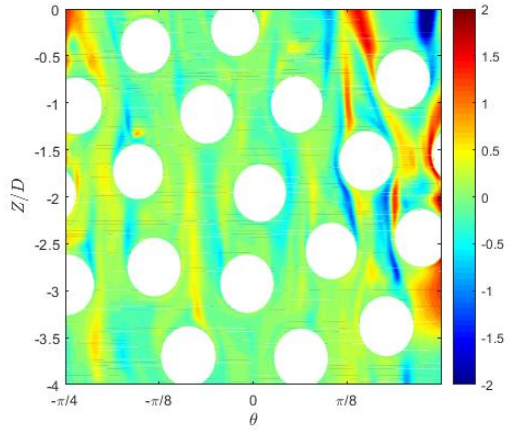

(c) Difference between full and symmetry case.

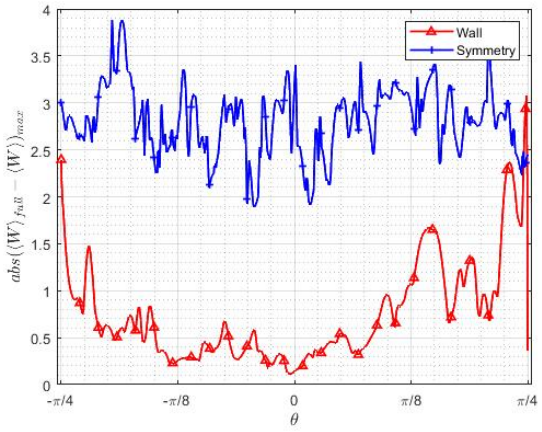

(d) Line plot showing the maximum absolute difference in $\langle U_z \rangle$ between the full, wall and symmetric cases at the specific angle.

Figure 5.5: Psuedo-color of the averaged stream wise velocity, $\langle U_z \rangle$, for $Re = 1050$ to show the effects of the boundary condition for the simplified cases.

paths where the flow is rapidly accelerated as the flow area decreases between the pebble and wall boundary. For the symmetry boundary case, Fig. 5.5c, these higher velocities are not seen on the boundary, however, the increase is rather seen on the downstream surface of the pebble located at $Z = -2.5D$. This difference perturbs the flow field and results in larger deviations in the wake of this pebble. It should be noted that some minor visualization artifacts are present in the results for the symmetric case. This is attributed to the import of data into Matlab for this case.

When comparing the absolute maximum difference at each increment of θ, Fig. 5.5d, the

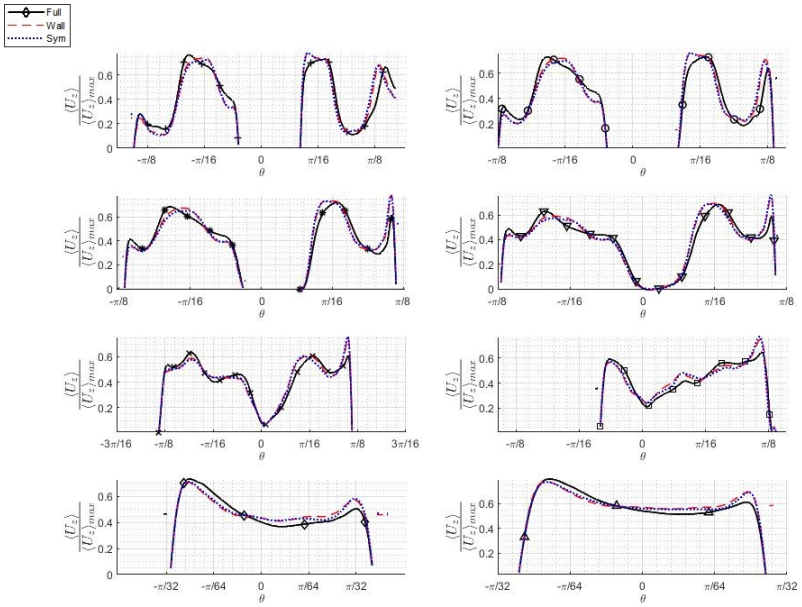

Figure 5.6: Normalized interpolated line profiles for $\langle U_z \rangle$. (Full: solid black, Wall: dash red, Symmetry: dot blue)

difference is clear. For both cases, a large deviation from the full case can be seen near the edge of the two simplified cases. For the wall case, the absolute difference decreases to almost zero in the center of the domain, where for the symmetric boundary condition case the difference seems to fluctuate around a set, higher average.

Figure 5.6 shows the interpolation line profiles for the streamwise velocity, $\langle U_z \rangle$, for all three cases, full in solid black, the wall in dash red and symmetry in dotted blue, normalized by the maximum value in the domain. The line-outs for the three cases all follow a similar trend indicating that in the center of the domain, the streamwise velocity is not much affected by the boundary conditions. It can be seen that the peak of maximum magnitude changes only slightly as the flow paths contract. For the lines spanning large arch lengths, the two distinct peaks with a valley of low velocity can be seen. Moving into the wake of the central pebble a stagnation point is seen on the downstream surface of the pebble. The velocity increases as the distance from the pebble are increased. The profiles also flatten out the further downstream they are. As we enter the contracted area between the to downstream pebbles the same line profile as in the FCC case of Fick [1] can

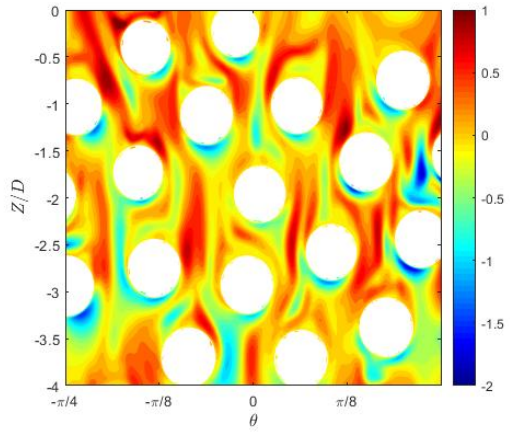

(a) Full geometry

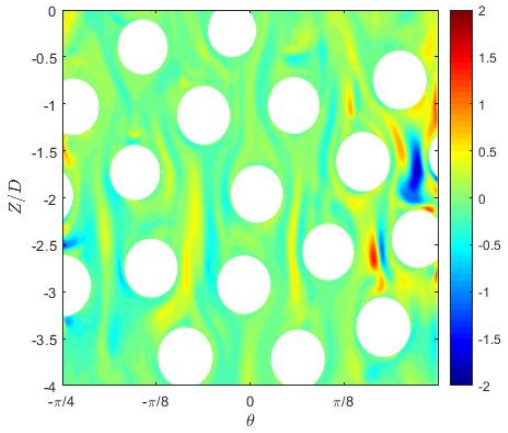

(b) Difference between full and wall case.

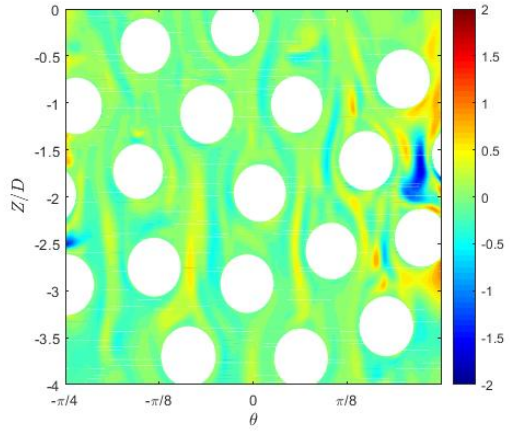

(c) Difference between full and symmetry case.

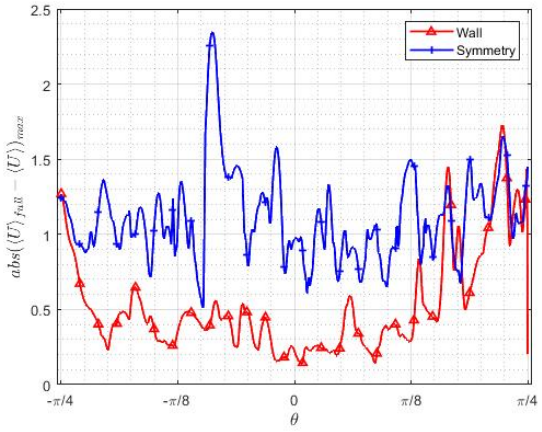

(d) Line plot showing the maximum absolute difference in $\langle U_x \rangle$ between the full, wall and symmetric cases at the specific angle.

Figure 5.7: Psuedo-color of the averaged in-plane velocity, $\langle U_x \rangle$, for $Re = 1050$ to show the effects of the boundary condition for the simplified cases.

be seen, even though the pebbles are not completely in line.

For the averaged in-plane velocity, $\langle U_x \rangle$, is shown in, Fig. 5.7a. From this, the values of negative magnitude can be seen on the bottom surfaces of the spheres as the flow gets accelerated towards the wall. The large areas of positive in-plane flow show where the flow is coming off the wall and moves towards the center of the domain. The positive structures are mostly seen in the inter pebble regions downstream of pebbles. For the differences, Fig. 5.7b and 5.7c, some small deviations from the full case‘s flow pattern can be seen between the pebbles, but most are once

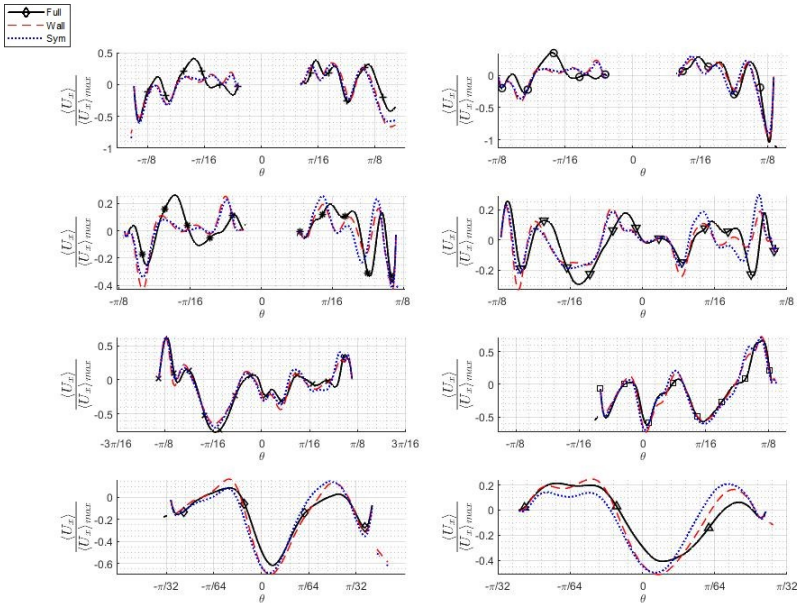

Figure 5.8: Normalized interpolated line profiles for $\langle U_x \rangle$. (Full: solid black, Wall: dash red, Symmetry: dot blue)

again visible near the boundary of the cases. When comparing the different flow fields, it appears that the way the pebble is intersected by the cut plane has a role to play in the difference.

The interpolation line profiles for the in-plane flow velocity, $\langle U_x \rangle$ in Fig. 5.8, shows alternating positive and negative flow. The positive values indicate flow moving away from the wall, where negative values indicate flow towards the wall. For lines spanning larger gaps, the flow switches magnitude more often with higher values at the pebble surfaces than in the mean flow region. It is noted that in the contracted region, downstream stream of center pebble, these fluctuations decrease as the flow is more mean flow driven. It is seen that for profiles on the downstream of the pebble surface the flow gets diverted towards the wall, as the flow is accelerated close to the sphere surface. The line-outs for the wall and symmetry cases follow the trend of the full case in the contraction but do slightly overestimate the in-plane velocities. For the large gaps, the trends are similar close to the sphere walls but deviate in the mean flow area.

For the cross-flow component, $\langle U_y \rangle$ in Fig. 5.9a, the positive-negative pairs are seen on the upstream surfaces of the spheres as the flow gets diverted around them. For the wall and symmetry

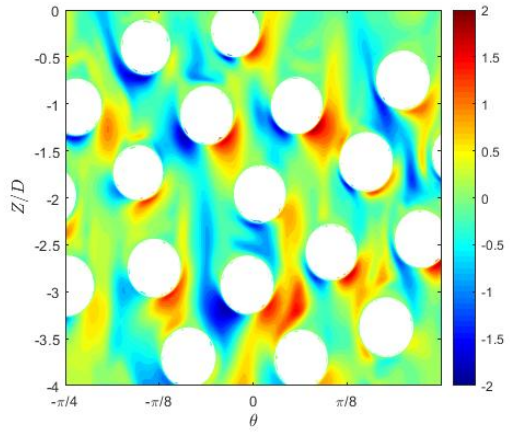

(a) Full geometry

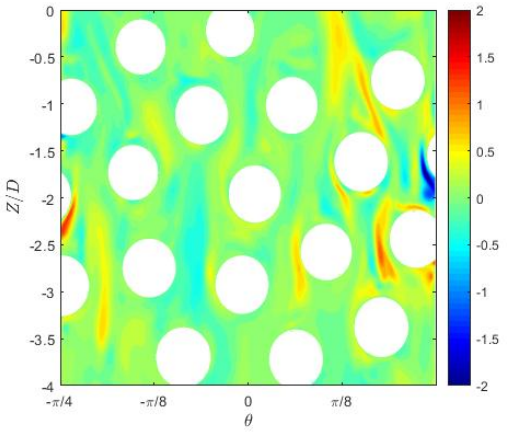

(b) Difference between full and wall case.

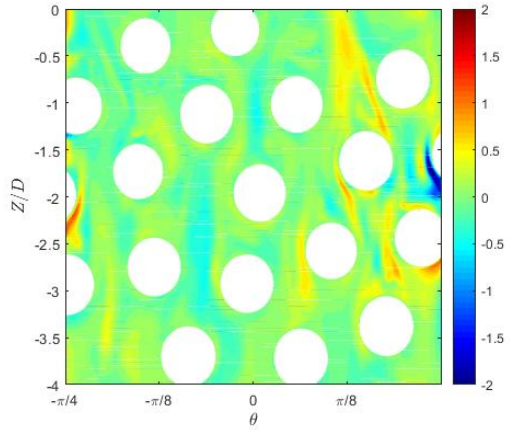

(c) Difference between full and symmetry case.

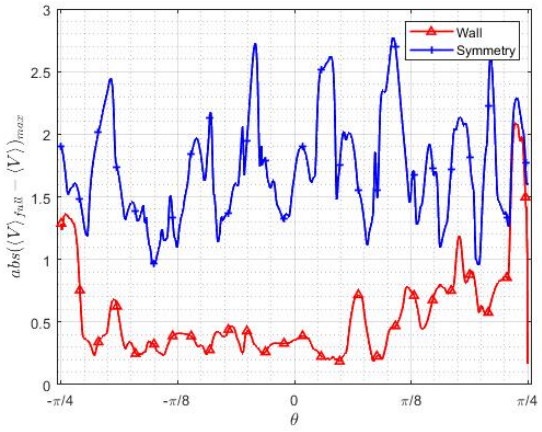

(d) Line plot showing the maximum absolute difference in $\langle U_y \rangle$ between the full, wall and symmetric cases at the specific angle.

Figure 5.9: Psuedo-color of the averaged cross-flow velocity, $\langle U_y \rangle$, for $Re = 1050$ to show the effects of the boundary condition for the simplified cases.

cases, Fig. 5.9b and 5.9c, the largest variation from the full flow are once again seen near the walls. For the absolute difference, Fig. 5.9d, the wall boundary case has again the lower values.

The interpolation line profiles for the cross-flow velocity, $\langle U_y \rangle$ in Fig. 5.10, shows less frequent switch between positive and negative values. The results for the three cases all follow the same trend, but with small variations on the local peaks of the plot. The highest values are seen on the downstream surfaces of the spheres, as the flow gets diverted around the high curvature. In the large inter pebble regions, one sees multiple sign changes in the flow. As the flow path contracts,

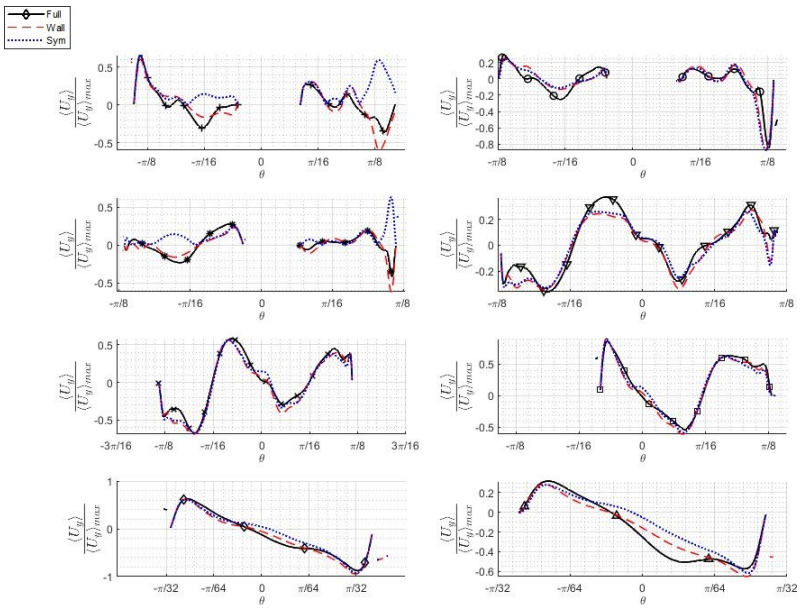

Figure 5.10: Normalized interpolated line profiles for $\langle U_y \rangle$. (Full: solid black, Wall: dash red, Symmetry: dot blue)

the flow becomes more mean flow driven and fewer fluctuations are seen. Once again, a similar profile as that seen in the cross-flow component for the FCC case of Fick [1].

From the lateral and cross flow components of first-order statistics, it was concluded that for pebbles with large inter pebble regions, a frequent change in sign occurs along the arc length and as the arc length is decreased these changed reduce in frequency. It was also seen that for pebble‘s whose center point is actually located outside of the domain the effects are relatively small, but when the center is actually located inside the domain larger errors are expected. For the absolute maximum difference, Fig. 5.7d, the same trend is seen where the wall-bounded case has a lower error close to the center of the domain. It is seen that for the cross-flow component the error is smaller for the symmetry plane than in the streamwise direction. From the first order statistics it is also seen that the for the averaged velocities, all the simplifications gave similar results on the center of the domain.

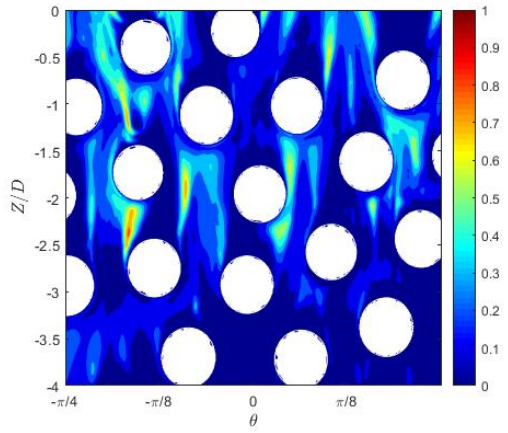

(a) Full geometry

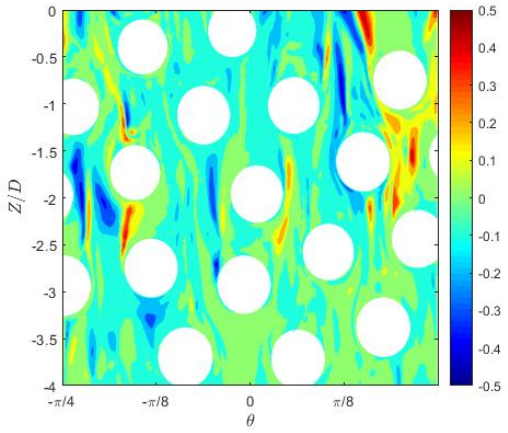

(b) Difference between full and wall case.

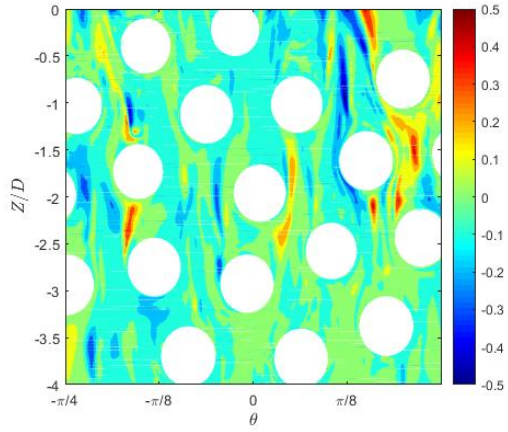

(c) Difference between full and symmetry case.

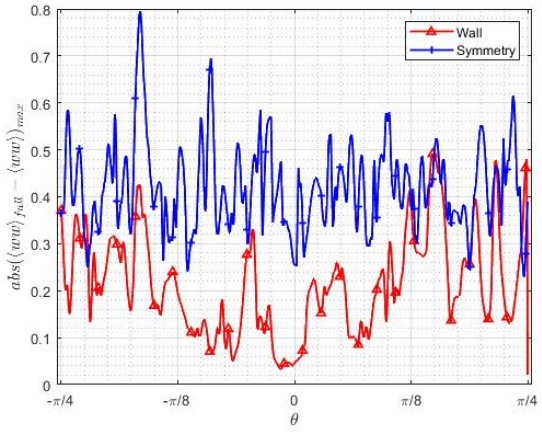

(d) Line plot showing the maximum absolute difference in $\langle u_z u_z \rangle$ between the full, wall and symmetric cases at the specific angle.

Figure 5.11: Psuedo-color of the stream wise Reynolds stresses, $\langle u_z u_z \rangle$, for $Re = 1050$ to show the effects of the boundary condition for the simplified cases.

5.3.3 Second-order statistics

The second order statistics in the near wall region gives the associated Reynolds stresses. These are calculated from the time-averaged variance and covariance, which is dependent on the fluctuations in the flow fields. For the streamwise Reynolds stresses, $\langle u_z u_z \rangle$ in Fig. 5.11a, a clear increase in magnitudes are seen in the regions between the fast flowing mean driven flow and the recirculation zones. For the rest of the domain, the stresses are near zero which means that there is little to

no fluctuations on these regions.

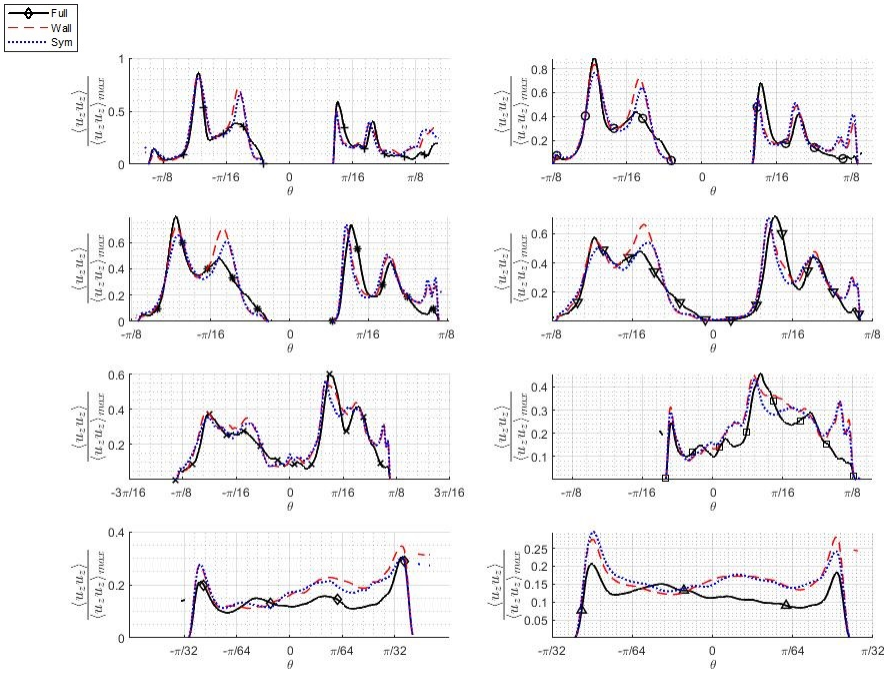

Figure 5.12: Normalized interpolated line profiles for $\langle u_z u_z \rangle$. (Full: solid black, Wall: dash red, Symmetry: dot blue)

For the wall-bounded case, Fig. 5.11b, the largest location of variation occurs in the downstream regions behind the pebbles that were intersected by the cut plane. In the mean flow regions itself, little variation is seen, but on the interface between the mean flow and recirculation zones, the wall-bounded case show differences. This is attributed to some of the stream-wise flow, that would have entered this domain due to the curvature of the intersected pebbles being lost.

For the symmetry case, Fig. 5.11c, smaller deviations are seen near the boundary of the case, but the same structures are witnessed in the transition regions between the high velocity mean driven flow and the recirculation zones.

When comparing the absolute maximum difference per angle, Fig. 5.11d, the wall-bounded case shows an overall lower difference in the streamwise Reynolds stresses than that of the sym-

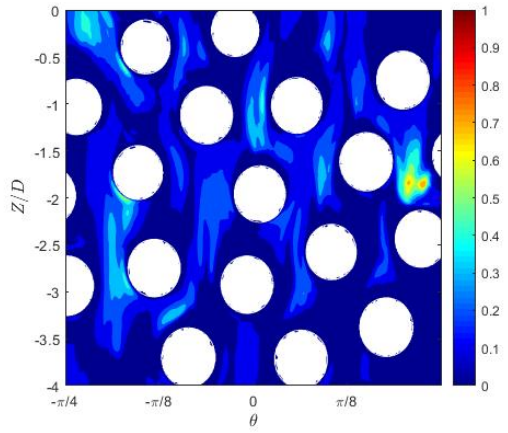

(a) Full geometry

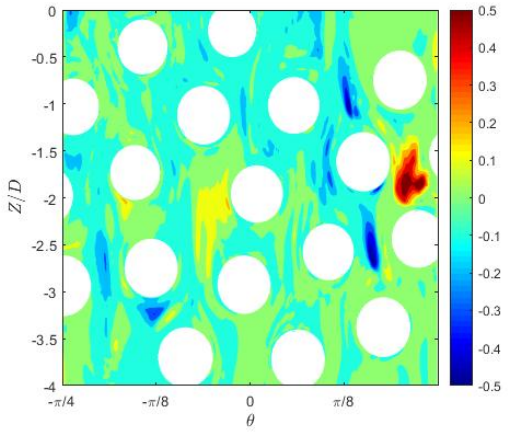

(b) Difference between full and wall case.

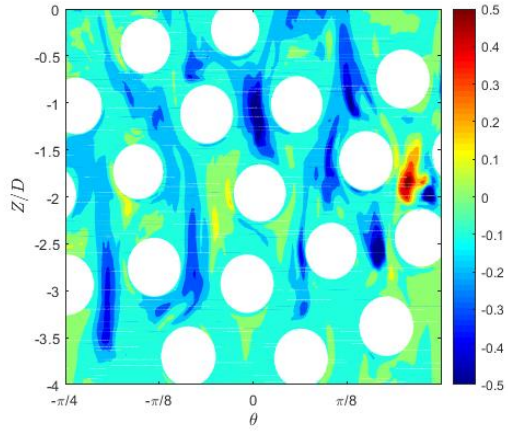

(c) Difference between full and symmetry case.

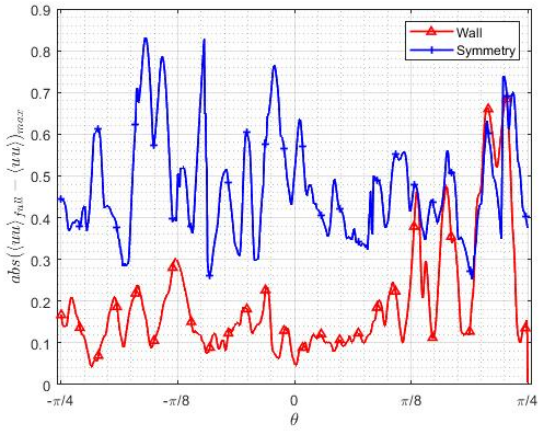

(d) Line plot showing the maximum absolute difference in $\langle u_x u_x \rangle$ between the full, wall and symmetric cases at the specific angle.

Figure 5.13: Psuedo-color of the stream wise Reynolds stresses, $\langle u_x u_x \rangle$, for $Re = 1050$ to show the effects of the boundary condition for the simplified cases.

metric case. For both cases, there is no significant error between the boundary and the center of the domain. Even though the magnitude of the difference is low, this shows that the streamwise fluctuations are somewhat affected by the flow in the rest of the domain.

The interpolation line profiles for the streamwise Reynolds stresses, $\langle u_z u_z \rangle$ in Fig. 5.12, shows peaks in the magnitude within the shear layer as the flow detaches from the pebble surface. Regions of high stress are also observed in the layer between the mean and stagnation zones. As the flow path restricts and the flow gets accelerated fewer peaks are observed in the mean flow region,

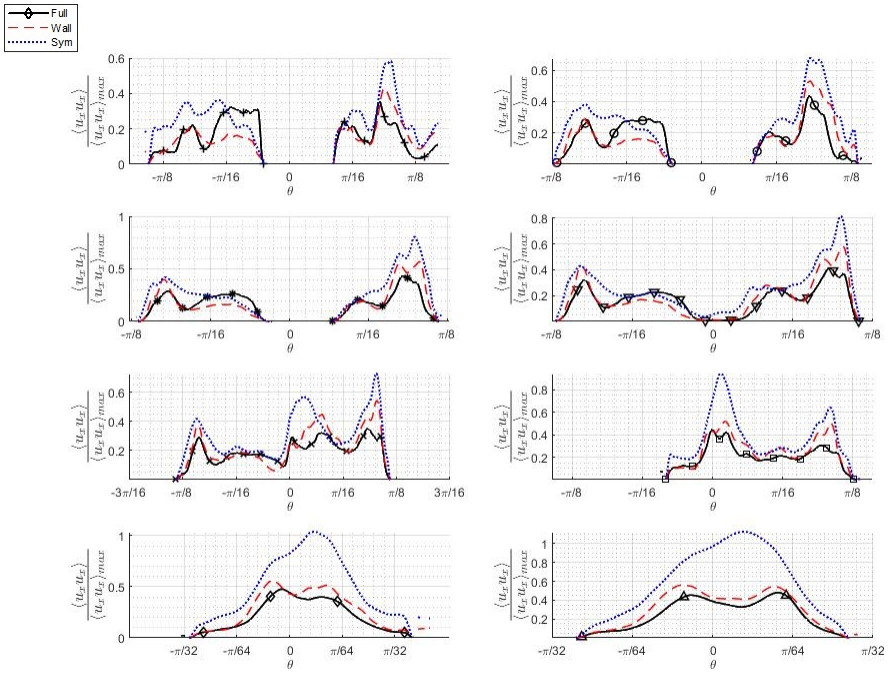

Figure 5.14: Normalized interpolated line profiles for $\langle u_x u_x \rangle$. (Full: solid black, Wall: dash red, Symmetry: dot blue)

while the shear layer peaks are still visible. This indicates that little fluctuations occur as the flow accelerates in the contracted region. When comparing the line-outs of the simplified cases the results are similar except for the shear layer of the center pebble where the Reynold stress is overestimated. In the contraction region, the same form is seen but the stress profiles seem to be switched by $180°$.

For the in-plane component of the Reynolds stress, $\langle u_x u_x \rangle$ in Fig. 5.13a, only small regions of high stress is witnessed. This indicates that little fluctuations are present in this direction close to the wall. This is due to the flow being mostly mean flow driven in the gaps between the pebbles and little fluctuation is present as the flow is being accelerated. The wall bounded case, Fig. 5.13b, underpredicts the lateral Reynolds stress near the wall, as the wall eliminates all flows close to the wall due to the wall action and boundary layers. A bit into the domain the wall-bounded cases overpredicts the stresses in the mean flow region. From Fig. 5.13c large regions of over-predictions are seen in the inter-pebble regions. For the simplified case the in-plane Reynolds

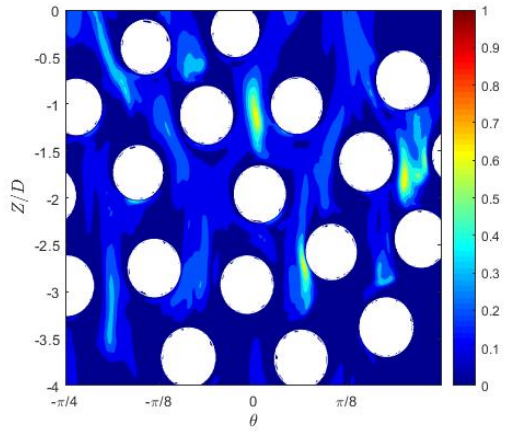

(a) Full geometry

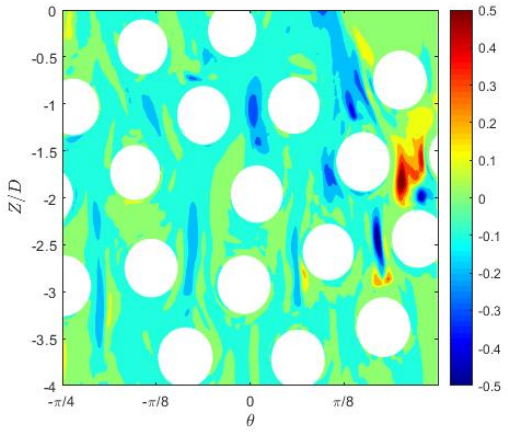

(b) Difference between full and wall case.

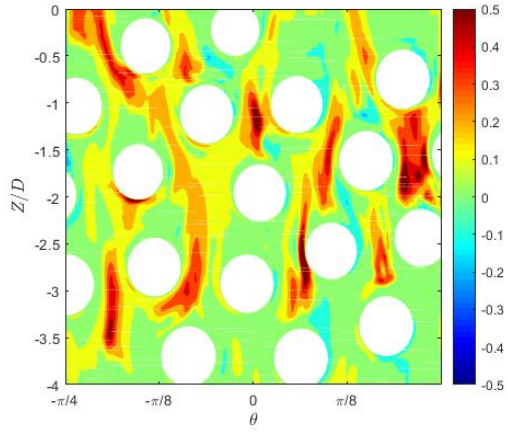

(c) Difference between full and symmetry case.

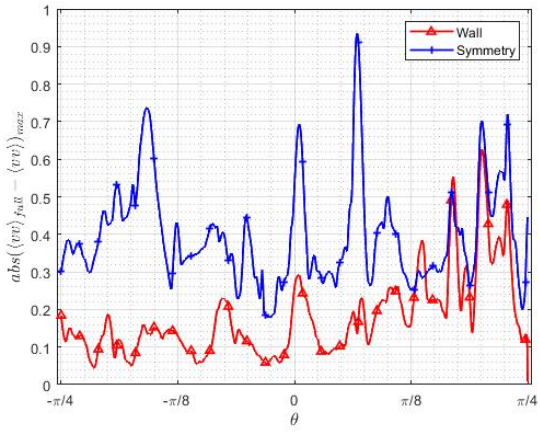

(d) Line plot showing the maximum absolute difference in $\langle u_y u_y \rangle$ between the full, wall and symmetric cases at the specific angle.

Figure 5.15: Psuedo-color of the stream wise Reynolds stresses, $\langle u_y u_y \rangle$, for $Re = 1050$ to show the effects of the boundary condition for the simplified cases.

stresses are overpredicted by both boundary cases, even though the same form is being followed.

The interpolation line profiles for the lateral Reynolds stresses, $\langle u_x u_x \rangle$ in Fig. 5.14, shows large fluctuations in the magnitude, with different peaks in the regions spanning a large θ. The smallest values are located next to the wall, where the peaks are located in the shear layer as the flow gets diverted around the pebble and detaches. In the contraction region, these peaks are smoothed out and located more towards the center of the flow path.

From the absolute magnitude of the difference, Fig. 5.13d, the trend is seen. In the wall region,

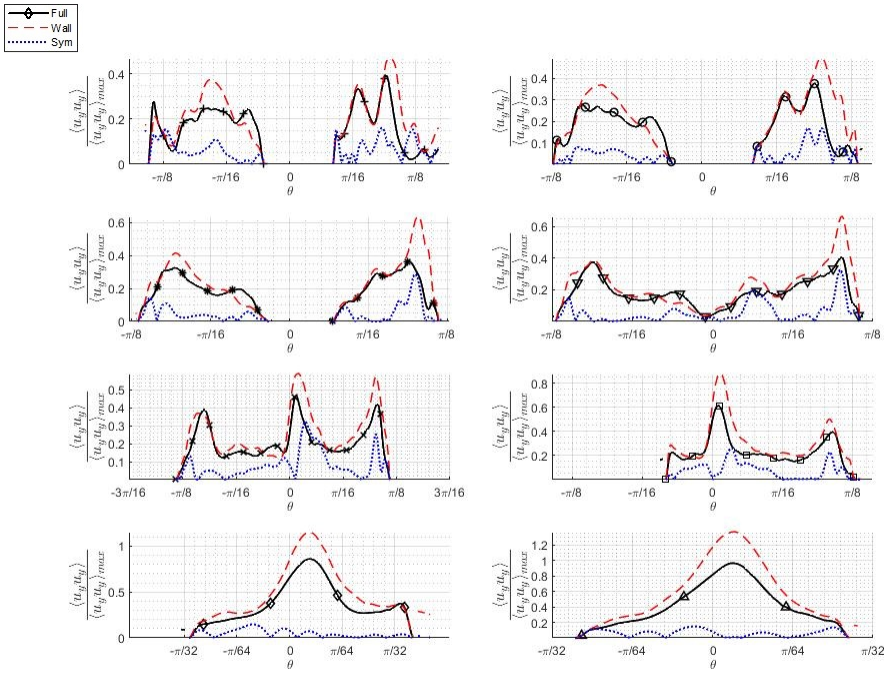

Figure 5.16: Normalized interpolated line profiles for $\langle u_y u_y \rangle$. (Full: solid black, Wall: dash red, Symmetry: dot blue)

$\theta \approx \pi/4$, the wall, and symmetric cases show similar differences. As one moves further from the wall the absolute difference reduces for the wall case, where the symmetry case remains with fairly large variation.

From the cross-flow component of the Reynolds stresses, $\langle u_y u_y \rangle$ in Fig. 5.15a, small regions of high stress are seen in the wake pebbles of pebbles. This coupled with the lateral flow component of the stress indicates that little to no flow or fluctuations happen in the recirculation zone of the pebbles close to the wall.

The cross-flow component for the wall-bounded case, Fig. 5.15b, shows the same trend as that for the lateral. The symmetric case, Fig. 5.15c, overpredicts the cross flow not only at the boundary but within the domain as well. This indicates that the zero-gradient condition introduces a significant cross-flow component to ensure the conservation of mass and momentum on the boundary.

The interpolation line profiles for the cross-flow Reynolds stresses, $\langle u_y u_y \rangle$ in Fig. 5.16, shows

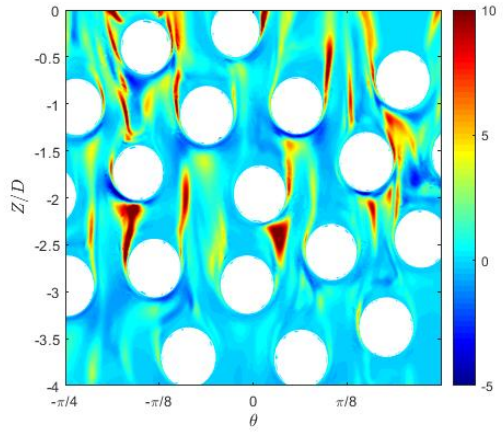

(a) Full geometry

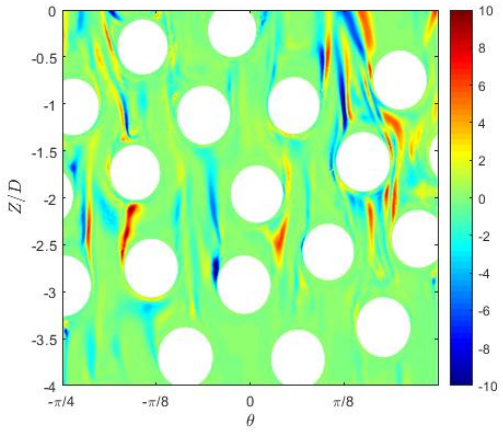

(b) Difference between full and wall case.

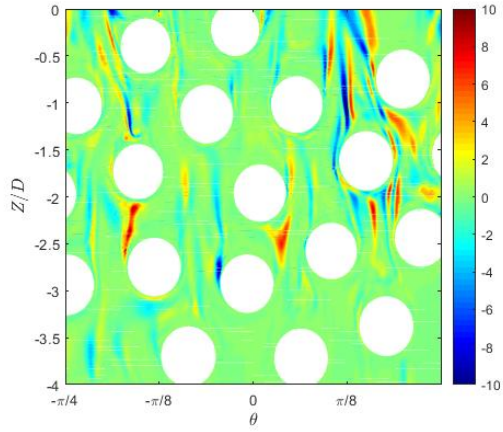

(c) Difference between full and symmetry case.

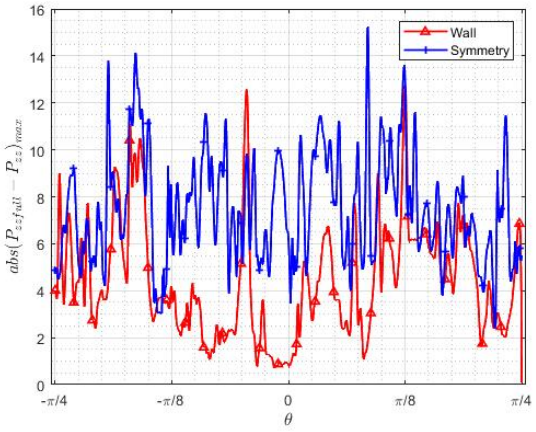

(d) Line plot showing the maximum absolute difference in P_{zz} between the full, wall and symmetric cases at the specific angle.

Figure 5.17: Psuedo-color of the stream wise Production, $\langle P_{zz} \rangle$, for $Re = 1050$ to show the effects of the boundary condition for the simplified cases.

fluctuating magnitudes, with different peaks in the regions spanning a large θ. The smallest values are located next to the wall, where the peaks are located in the shear layer as the flow gets diverted around the pebble and detaches. In the contraction region, these peaks are smoothed out and located more towards the center of the flow path. From the line outs, the wall-bounded case does follow the trends of the full case but overpredicts the Reynolds stresses. For the symmetry case, the stresses are underpredicted.

Due to the large amounts of data already presented the off-diagonal component discussion of

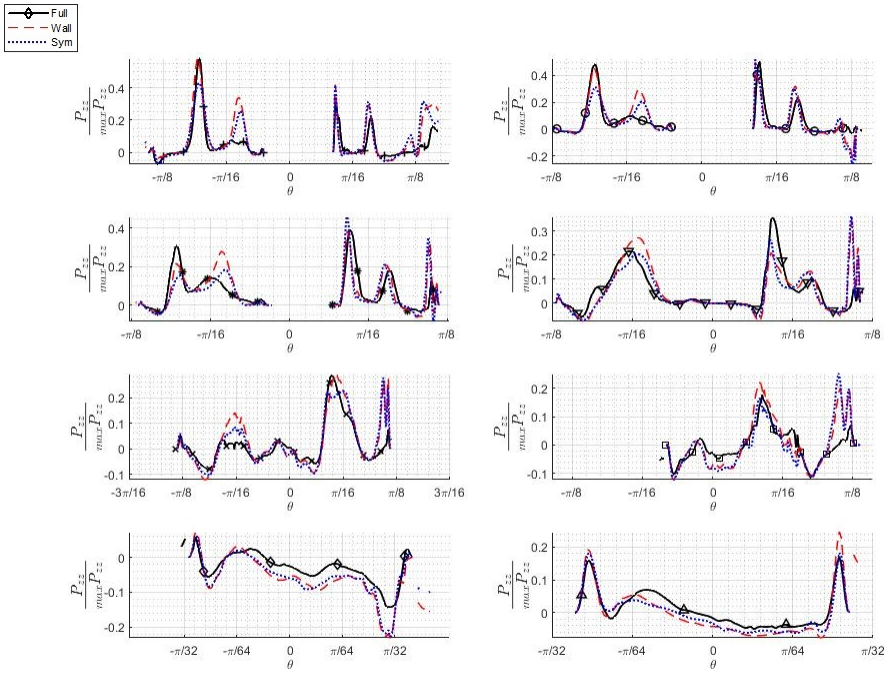

Figure 5.18: Normalized interpolated line profiles for $\langle P_{zz} \rangle$. (Full: solid black, Wall: dash red, Symmetry: dot blue)

the Reynolds stress tensor was omitted for simplicity. The line outs can be found in Appendix A.

5.3.4 TKE

The streamwise component of the production tensor, P_{zz} in Fig. 5.17a, shows large values in the shear layer between the mean and recirculation zone. Highest stream-wise production is seen in the regions where the flow is decelerated. Large negative production is found on the upstream surfaces of the spheres where the flow re-attaches and gets accelerated around the spheres. In the recirculation zone, in the wake of the pebbles, little production is seen.

When comparing the differences between the wall, Fig. 5.17b, and symmetry case, Fig. 5.17a. It is seen that the large differences are not only isolated to the boundary of the domain, but also in the shear layers. This is because the production is calculated by the gradient of the average velocity and the associated Reynolds stresses. From the previous subsection, it was seen that the simplification did not affect the averaged velocities much, but did the Reynolds stresses. The

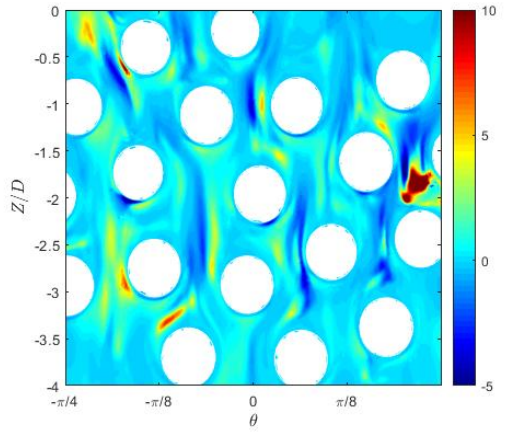

(a) Full geometry

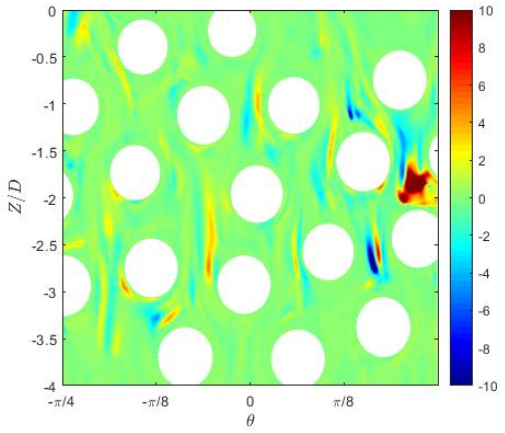

(b) Difference between full and wall case.

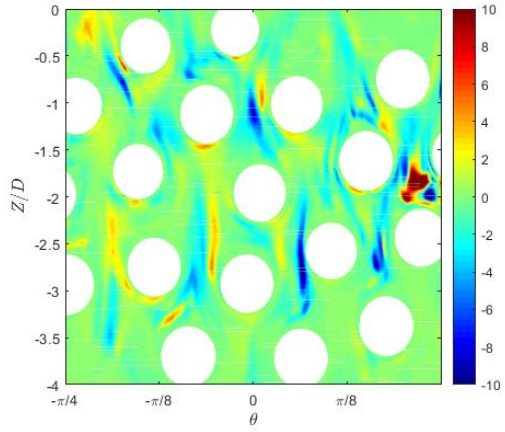

(c) Difference between full and symmetry case.

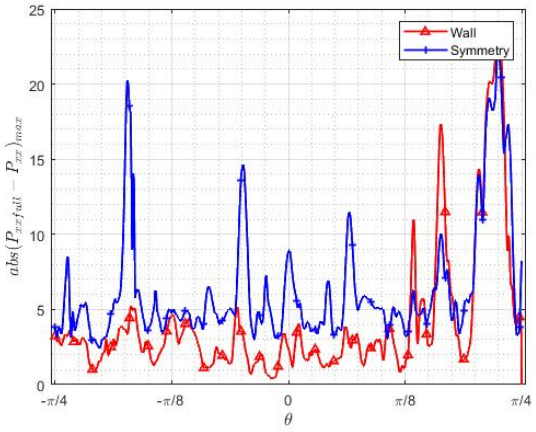

(d) Line plot showing the maximum absolute difference in P_{xx} between the full, wall and symmetric cases at the specific angle.

Figure 5.19: Psuedo-color of the in plane Production, P_{xx}, for $Re = 1050$ to show the effects of the boundary condition for the simplified cases.

absolute magnitude in the difference, Fig. 5.17d, can be seen to highlight the matter.

The interpolation line profiles for the streamwise production component, P_{zz} in Fig. 5.18, the high peaks in the shear layer is seen. For the first few lines covering a larger span, numerous peaks are witnessed as the flow from the upstream pebbles get combined. Little to no production is seen in the wake region of the center pebble. As the flow path contracts the production flattens out and the peaks are only seen in the shear layer. On the upstream surface shear layer, negative production is seen as the flow re-attaches to the surface and gets accelerated. When the flow detaches past the

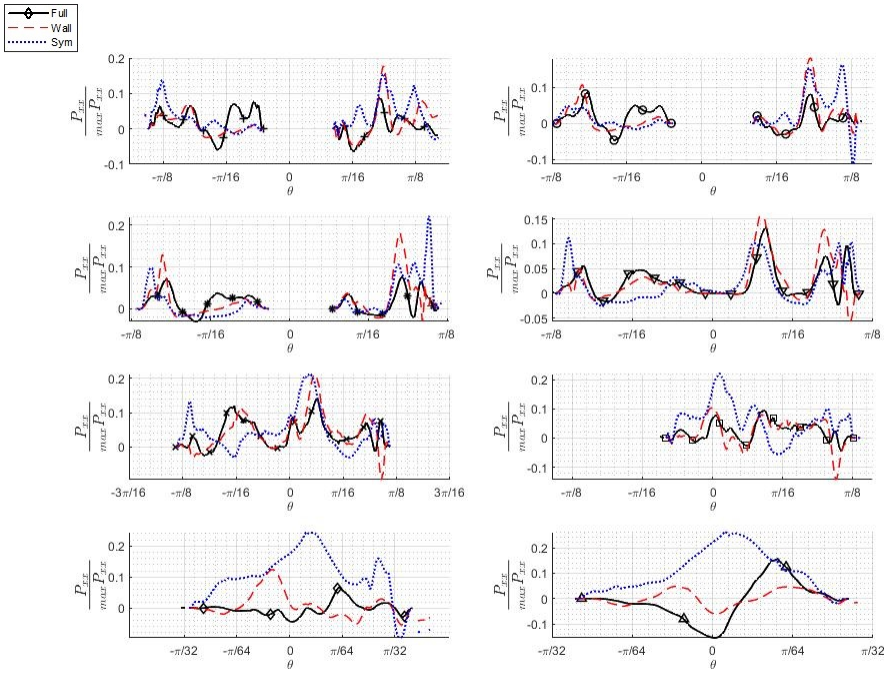

Figure 5.20: Normalized interpolated line profiles for P_{xx}. (Full: solid black, Wall: dash red, Symmetry: dot blue)

equator of the pebble the interaction between the recirculation zone and the mean flow generates the production of TKE. The line outs for the simplified cases do follow the same trend as the full case, but the peaks are over estimated.

The in-plane component of the production tensor, P_{xx} in Fig. 5.19a, has negative production on the upstream surfaces where the flow gets accelerated around the spheres. A large positive cell is seen in the wake of the pebble located at $[-\pi/4, -2.5D]$, under further inspection of the geometry it was seen that a sphere is located just off the plane where the flow is being decelerated against causing a low-velocity region. For the wall case, Fig. 5.19b, the difference in results are located to wake region of this sphere and minor deviations in the shear layers. For the symmetry case, Fig. 5.19c, the production is overestimated in the shear layers between pebbles. The absolute difference, Fig 5.19d show that both the wall and has a large variation in the results at $\theta \approx \pi/4$. The symmetry has high peaks area throughout the domain.

The interpolation line out profiles for the in-plane component of the production tensor is shown

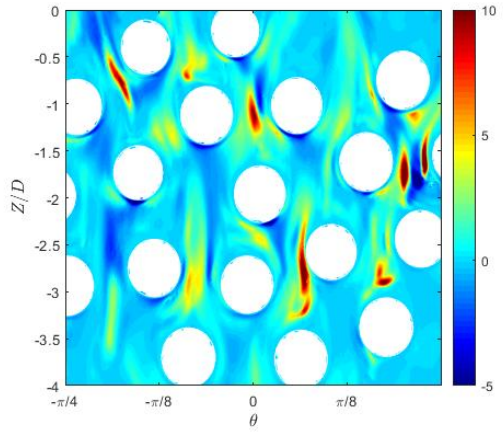

(a) Full geometry

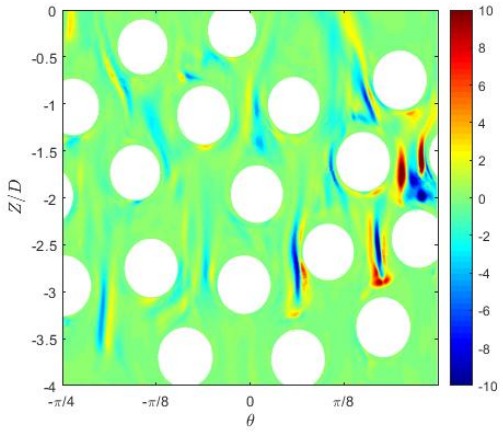

(b) Difference between full and wall case.

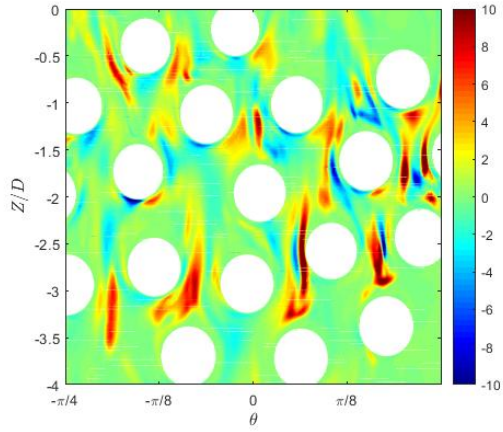

(c) Difference between full and symmetry case.

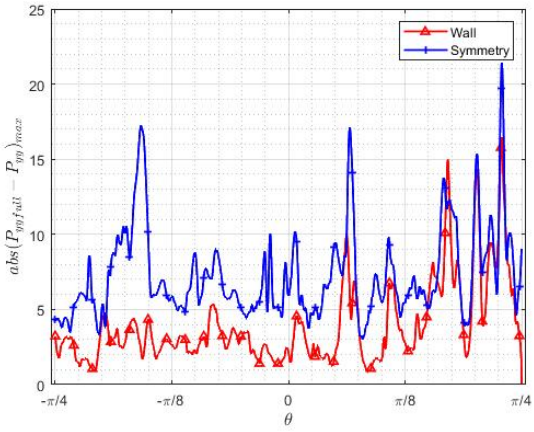

(d) Line plot showing the maximum absolute difference in P_{yy} between the full, wall and symmetric cases at the specific angle.

Figure 5.21: Psuedo-color of the cross flow Production, P_{yy}, for $Re = 1050$ to show the effects of the boundary condition for the simplified cases.

in Fig. 5.20. The clear overestimation of the production is seen in the profiles for the wall and symmetry case. For the large span profiles, the trends match up close to the pebble surfaces but deviate further from the wall. In the contraction, the production does not match up at all.

The cross-flow component, P_{yy} in Fig. 5.21a, shows negative production in the shear layer of the flow and upstream surfaces of the spheres as the flow is accelerated around the sphere. The wall bounded case, Fig. 5.21b, shows positive-negative pairs in the wakes of pebbles. These over and underestimations are larger for the symmetric case, Fig. 5.21c.

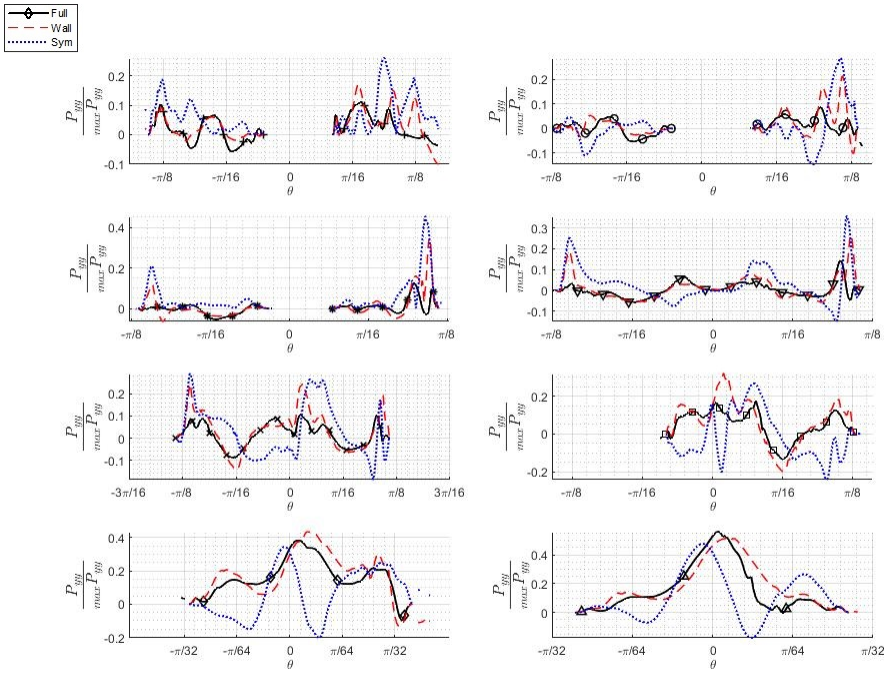

Figure 5.22: Normalized interpolated line profiles for P_{yy}. (Full: solid black, Wall: dash red, Symmetry: dot blue)

The interpolation line-out profiles for the cross-flow component of the production tensor is shown in Fig. 5.22. For the full case, the highest production is located in the contraction between the two spheres. The simplification wall bounded case captures the trend, but the symmetric case fails to capture the production. For the other line profiles, the wall case overestimates the peaks of the production, but the general trend is pretty much satisfied. The symmetric case struggles to match the profiles of the full case.

The streamwise component of the dissipation tensor, ϵ_{zz} in Fig. 5.23a, shows high dissipation in the boundary layer on the upstream surfaces of the pebbles where the mean flow re-attaches. Some lower dissipation regions are seen in the shear layer of the pebbles. Most of the dissipation occurs on pebble surfaces where the flow reattaches. The wall bounded case, Fig 5.23b underpredicts the dissipation in the shear layer and greatly overpredicts the dissipation on the pebble surfaces. The symmetric case, Fig. 5.23c shows the same trend. This can be seen when comparing the absolute magnitude difference, Fig. 5.23d, where both cases have similar values and peaks.

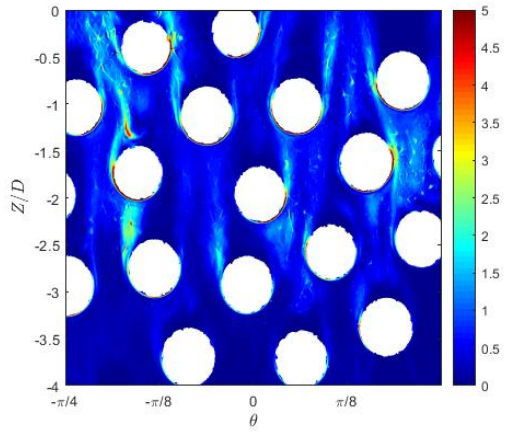

(a) Full geometry

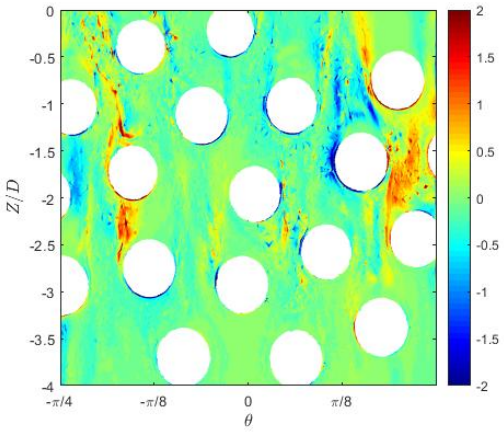

(b) Difference between full and wall case.

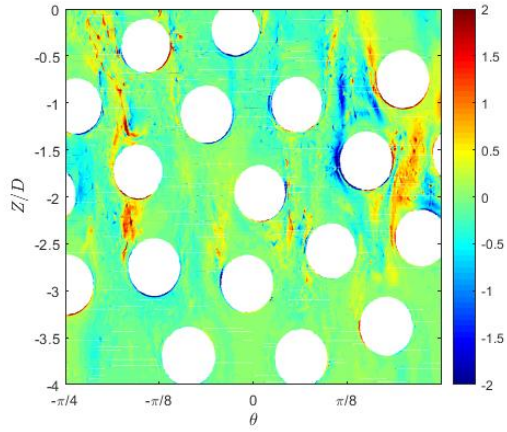

(c) Difference between full and symmetry case.

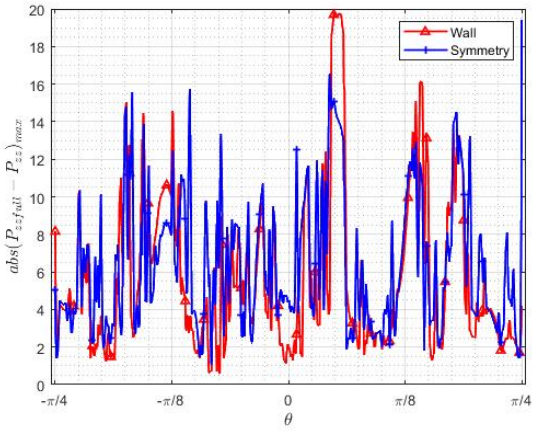

(d) Line plot showing the maximum absolute difference in ϵ_{zz} between the full, wall and symmetric cases at the specific angle.

Figure 5.23: Psuedo-color of the stream wise Production, ϵ_{zz}, for $Re = 1050$ to show the effects of the boundary condition for the simplified cases.

When comparing the interpolation line profiles, Fig. 5.24, it is seen that little dissipation occurs in the mean flow region. High dissipation is seen on the surface of the spheres where the flow reattaches. Even though the symmetry and wall-bounded cases capture the mean flow region dissipation well, they greatly overpredict the dissipation on the walls of the spheres.

The in-plane component of the dissipation tensor, ϵ_{xx} in Fig. 5.25a, shows very little dissipation in the domain, Most of the high dissipation regions are once again found on the upstream surfaces as the flow reattached and gets directed towards the wall. The high pocked of dissipation in the

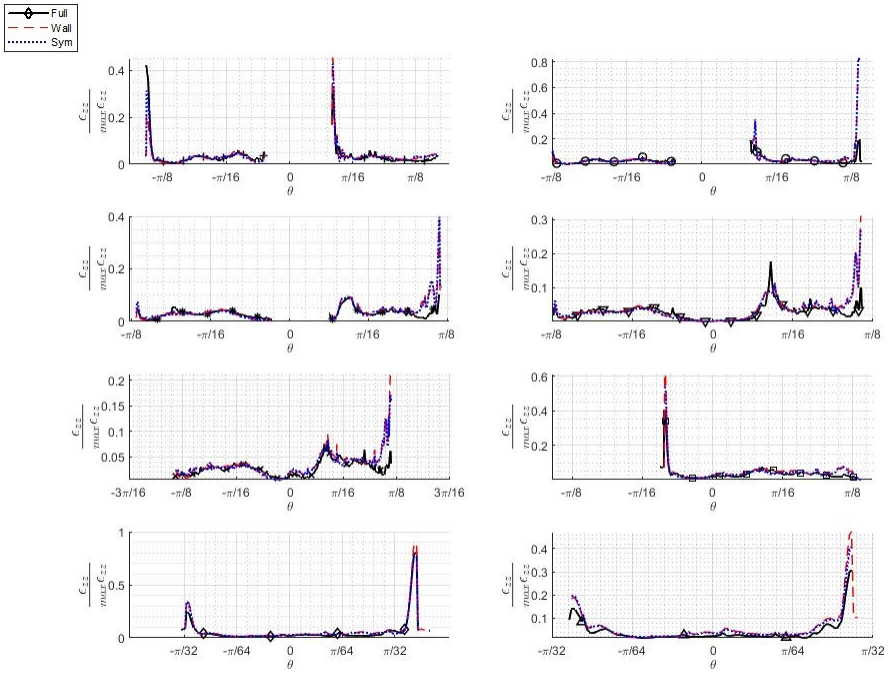

Figure 5.24: Normalized interpolated line profiles for ϵ_{zz}. (Full: solid black, Wall: dash red, Symmetry: dot blue)

wake of the right pebble is seen as the flow comes off the pebble that is just out of the plane. The wall bounded case, Fig. 5.25b, have some deviation on near the wall and the upstream surfaces of pebbles close to the wall. The symmetric case, Fig. 5.25c sows large regions of overprediction. The absolute magnitude difference, Fig. 5.25d, shows the lower error of the wall-bounded case to that of the symmetric one.

The interpolation lines of the in-plane component, Fig. 5.26, shows the same trend as the streamwise. The inter pebble dissipation is closely matched by the simplified cases but is overestimated near the walls.

The cross-flow component, ϵ_{yy} in Fig. 5.27a, follows the same trend of the previous two components. The maximum values are seen on the upstream surfaces of the spheres and little to no dissipation the rest of the domain. For the wall-bounded case, Fig. 5.27b the dissipation on the pebble surfaces are overestimated. There is also a large variation on the region close to the boundary. The symmetric case, Fig 5.27b shows large regions of underestimation around the

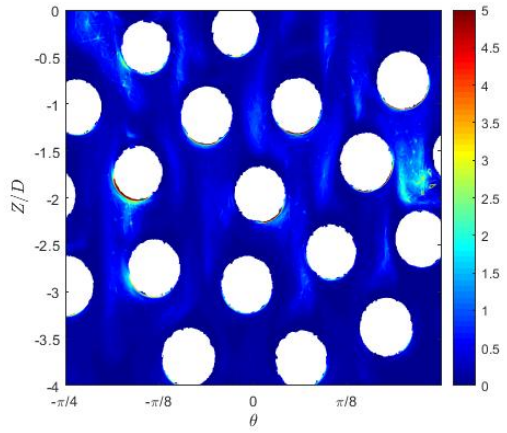

(a) Full geometry

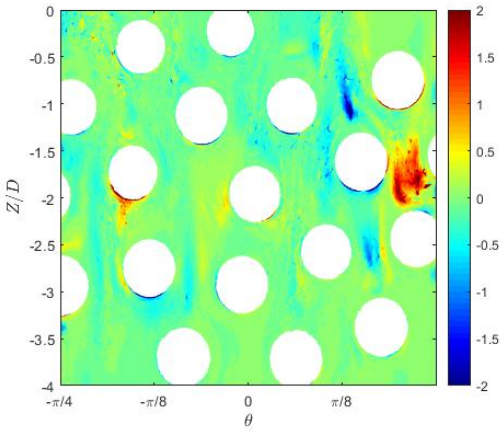

(b) Difference between full and wall case.

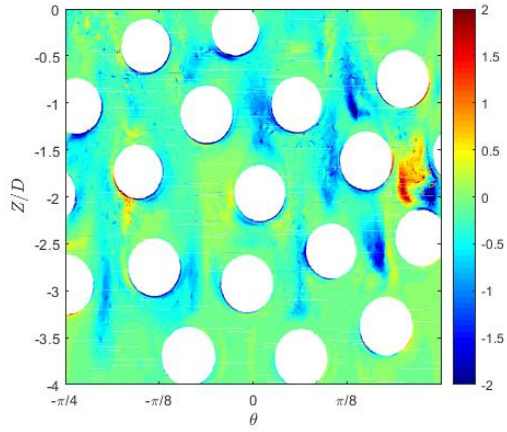

(c) Difference between full and symmetry case.

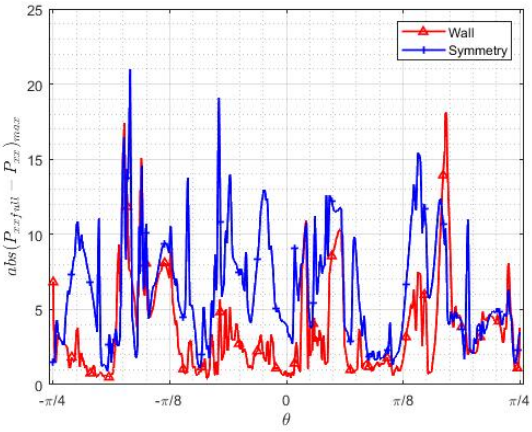

(d) Line plot showing the maximum absolute difference in ϵ_{xx} between the full, wall and symmetric cases at the specific angle.

Figure 5.25: Psuedo-color of the in plane Production, ϵ_{xx}, for $Re = 1050$ to show the effects of the boundary condition for the simplified cases.

upstream surfaces of the spheres, as well as the shear layer between the pebbles. From the absolute magnitude difference, Fig. 5.27d, both cases follow the same trend with the symmetry case having fewer fluctuations and larger peaks.

The interpolation profiles for the cross-flow component, Fig. 5.28, shows that the wall-bounded case overestimates the peaks of the dissipation, but follows the profile. The symmetric case, on the other hand, underestimates the cross-flow component in the contraction region between the two pebbles.

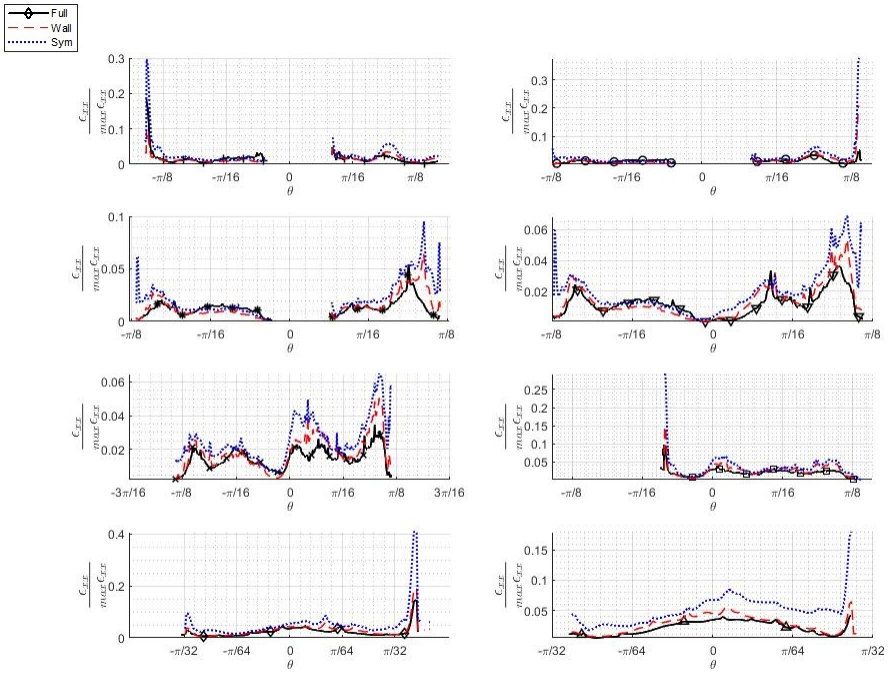

Figure 5.26: Normalized interpolated line profiles for ϵ_{xx}. (Full: solid black, Wall: dash red, Symmetry: dot blue)

With the diagonal components of the wall and symmetry cases deviating from the full case, it was found redundant to show the off-diagonal components as well, as these follow the same trend. Because the dissipation is calculated from the gradient of the fluctuations small deviations introduced to the fluctuations based on the boundary conditions resulted in deviations presented in this subsection. The other TKE budget terms were omitted from this section as the data presented already become overwhelming and repetitive. These terms were also omitted as they do not play a big role in the lower fidelity schemes.

The omitted off-diagonal components of the production and dissipation term line outs can be found in Appendix B.

5.4 Conclusions

This section detailed the effects simplifying the domain and the resulting influence the boundary conditions has on the first- and second order statistics, as well well as the TKE for a randomly

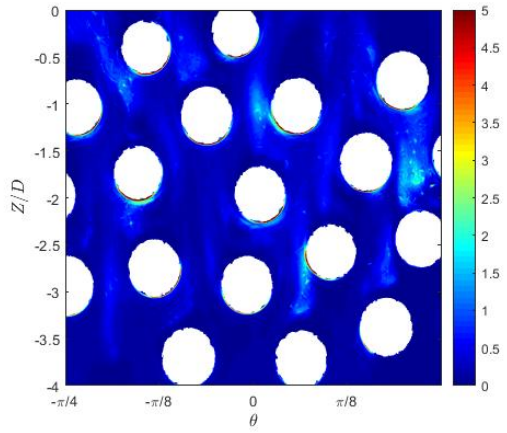

(a) Full geometry

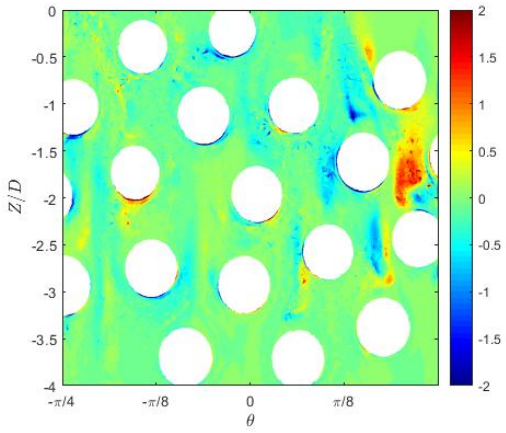

(b) Difference between full and wall case.

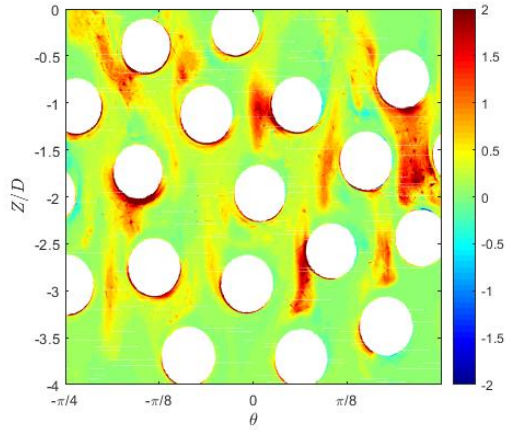

(c) Difference between full and symmetry case.

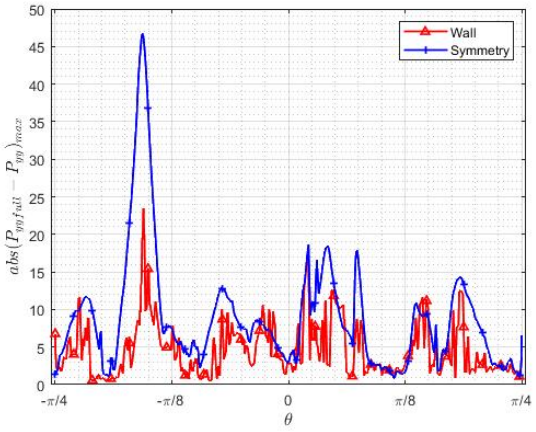

(d) Line plot showing the maximum absolute difference in ϵ_{yy} between the full, wall and symmetric cases at the specific angle.

Figure 5.27: Psuedo-color of the cross flow Production, ϵ_{yy}, for $Re = 1050$ to show the effects of the boundary condition for the simplified cases.

packed pebble bed. From the literature review, no work has been done to investigate the effects of reducing the domain. The focus of the study was on the near-wall region in the center of the domain. The results obtained was compared to that of the full geometry DNS data.

It was found that for the first order statistics the simplification cases produced results that were within reasonable margins of the full geometry. For the second order statistics, that is dependent on the fluctuations in the flow, it was found that the results obtained from the simplified cases deviated too much from the full geometry. Lastly, diagonal components of the production and dissipation

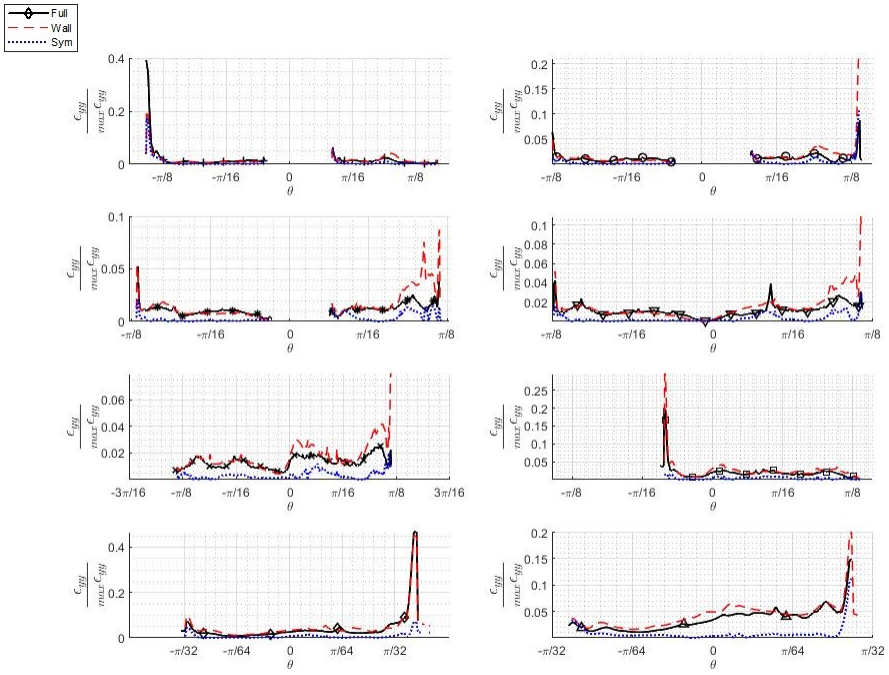

Figure 5.28: Normalized interpolated line profiles for ϵ_{yy}. (Full: solid black, Wall: dash red, Symmetry: dot blue)

tensor were compared to one another. For the streamwise components the results between the three cases matched within a good margin. The in-plane and cross flow components, on the other hand, deviated drastically.

From this study, we can conclude that the streamwise results of the first and second order statics, as well as the streamwise components of the production and dissipation tensor, is not affected by the reduction of the case nor the boundary conditions. For the other components, only those of the first order statistics provided acceptable results after the simplification.

6. CONCLUSIONS

In this section, conclusions from the different numerical experiments are used to for an overarching set of conclusions. The goal of each numerical investigation is restated in the preceding subsections. The study is then finished off by discussing the conclusions for each objective.

6.1 Conclusions

The conclusions are drawn as they were presented in the results section of each chapter.

6.1.1 Numerical Experiment I

- Verify the simulation and meshing methodology by using the available numerical simulation from previous research.

DNS data, from the previous study done by Fick [1], on the flow past two spheres in a free stream as used to verify the correct implementation of the case. The time-averaged flow fields, associated second-order statistics, POD and axial center-line velocities were used to draw comparisons. Form these almost exact comparisons were obtained for the same pebble spacing.

It was paramount that the simulation methodology is confirmed before the pebble spacing was varied and the focus ultimately be moved to the random packed case. Since the objective of varying the pebble spacing for the free stream flow would help identify flow behaviors in the random packed bed.

- Confirm the increase in meta-stable behavior with varying pebble spacing

Comparing the first- and second order turbulence statistics and the respective components for the TKE transport equation, it was observed that a critical pebble spacing exists that maximized the asymmetry and magnitude of the time-averaged flow. This is consistent with the varying results obtained from the random packed experimental case.

6.1.2 Numerical Experiment II

- Mesh generation for a random packed pebble bed.

The boundary layer projection, developed by Argonne and modified for the random pebble case, showed to have decreased the number of elements per pebble by almost a factor of 10. This new method allowed for adequately meshing the complex and high curvature geometry of a random packed pebble bed for the use of SEM methods. The boundary layer extrusion took care of the pebble-pebble interaction, while the close proximity stopped element movement where pebbles are to close to one another.

- Generate a high-fidelity database of time-invariant flow data.

  Three different Reynolds numbers were simulated to investigate the flow behavior of the random packed pebble bed. From these simulations a high-fidelity time-invariant database for the flow near the wall was generated for:

  - First- and second-order turbulence statistics
  - Turbulent kinetic energy budget terms.

  The results presented in Chapter 4 was tested for DNS requirements by calculating the Kolmogorov scales for different polynomial orders. From these criteria, the data conforms to the requirements of DNS.

  The data of the fifth-degree discretization showed the complexity of the flow through the random packed pebble and the computational cost associated with DNS. For practical applications, it is important to show that once DNS requirements are met the results do not change, but the associated computational cost for higher polynomial orders increases. Thus first- and second order statistics do not require high polynomial orders Due to the packing of the bed no temporal oscillations were found.

6.1.3 Numerical Experiment III

- Investigate reduced domain approximation.

When reducing the full geometry to a quarter it was found that the cut plane caused numerical instability near the center of the domain, a small wall bounded section needed to be included to ensure the solutions does not diverge. It was observed the spheres whose centroid was located just inside the cut plane introduced numerical instabilities due to the high curvature and small flow paths created for the zero-gradient condition. For both the wall and symmetric boundary condition the computational cost was reduced by almost a factor of 4. This reduction in computational cost can allow for bigger streamwise geometries to be investigated.

- Generate first of its kind DNS results.

The purpose of this study was to investigate how the simplification of the geometry affected the turbulence statistics in the near wall region of the unstructured pebble bed. The statistics were observed a set radial distance from the wall. In this region, different wall packings were observed with more dominant flow channels. It was found that in the contraction between pebbles the flow relaminarize. Multiple stagnation zones have been observed in the wakes of the spheres next to the wall. As stated, these stagnation zones can have significant effects on the heat transfer characteristics on a practical system, as the convective heat transfer is significantly reduced in these regions resulting in large temperature gradients. These potential thermal stresses, combined with long core operating time can result in a decrease in structural integrity.

For the simplification cases, it was seen that both the wall and symmetry case provided adequate first order statistics in the near wall region in the center of the region of interest. For the second order statistics, only the streamwise component did not deviate from the full case. The cross and lateral flow Reynolds stresses were not adequately captured by the simplification which indicates that these components are dependent on the rest of the geometry. The TKE budgets were shown that the streamwise components' profiles were captured, but the magnitudes were overestimated by the simplified cases.

6.1.4 Future Work

Based on the finding of this study, a number of subsequent studies may be initiated to expand upon the analysis presented. Future and proposed work can include:

- The addition to heat transfer to characterize the effects of varying fluid temperatures and properties has on the flow and temperature distribution in the random and random packed geometries. It would be recommended that conjugated heat transfer be used for such a study. The study can first be performed with constant fluid properties to before temperature dependent properties are introduced for comparison between iso-thermal, iso- and varying properties.

- Investigate the effects of larger flow domains. As this study only covered a small section of the experimental random packed pebble bed it is proposed to increase the domain high, say duplicating the geometry in the stream wise direction. That way better comparisons on the domain independence can be drawn as a repeating pattern will be present.

- Investigate the effects of simulating higher Reynolds numbers that is actually found during reactor operations.

REFERENCES

[1] L. H. Fick, *Direct numerical simualtion of incompressible flows in domains of close packed spheres*. PhD thesis, Texas A&M University, 2017.

[2] A. M. U. Guide, "Rel. 14.5," *ANSYS Inc*, 2012.

[3] I. ANSYS, "Cfd tutorial manual," 2007.

[4] M. A. Fütterer, L. Fu, C. Sink, S. de Groot, M. Pouchon, Y. W. Kim, F. Carré, and Y. Tachibana, "Status of the very high temperature reactor system," *Progress in Nuclear Energy*, vol. 77, pp. 266–281, 2014.

[5] P. Sabharwall, S. M. Bragg-Sitton, and C. Stoots, "Challenges in the development of high temperature reactors," *Energy conversion and management*, vol. 74, pp. 574–581, 2013.

[6] R. F. Garcia, M. R. Gomez, J. C. Carril, and J. R. Gomez, "Vhtr-based power plants' performance enhancement using rankine cycles," *Progress in Nuclear Energy*, vol. 71, pp. 206–215, 2014.

[7] S. B. Pope, *Turbulent flows*. IOP Publishing, 2001.

[8] C. Argyropoulos and N. Markatos, "Recent advances on the numerical modelling of turbulent flows," *Applied Mathematical Modelling*, vol. 39, no. 2, pp. 693–732, 2015.

[9] A. Shams, F. Roelofs, E. Komen, and E. Baglietto, "Improved delayed detached eddy simulation of a randomly stacked nuclear pebble bed," *Computers & Fluids*, vol. 122, pp. 12–25, 2015.

[10] A. Shams, F. Roelofs, E. Komen, and E. Baglietto, "Large eddy simulation of a randomly stacked nuclear pebble bed," *Computers & Fluids*, vol. 96, pp. 302–321, 2014.

[11] A. Shams, F. Roelofs, E. Komen, and E. Baglietto, "Large eddy simulation of a nuclear pebble bed configuration," *Nuclear Engineering and Design*, vol. 261, pp. 10–19, 2013.

[12] Y. A. Hassan, "Large eddy simulation in pebble bed gas cooled core reactors," *Nuclear Engineering and Design*, vol. 238, no. 3, pp. 530–537, 2008.

[13] A. T. Patera, "A spectral element method for fluid dynamics: laminar flow in a channel expansion," *Journal of computational Physics*, vol. 54, no. 3, pp. 468–488, 1984.

[14] Y. Maday and A. T. Patera, "Spectral element methods for the incompressible navier-stokes equations," in *IN: State-of-the-art surveys on computational mechanics (A90-47176 21-64). New York, American Society of Mechanical Engineers, 1989, p. 71-143. Research supported by DARPA.*, pp. 71–143, 1989.

[15] P. Fischer, J. Lottes, S. Kerkemeier, O. Marin, K. Heisey, E. Obabko, A. annd Merzari, and Y. Peet, "Nek5000 user documentation," *Argonne National Laboratory*, 2016.

[16] M. O. Deville, P. F. Fischer, and E. H. Mund, *High-order methods for incompressible fluid flow*, vol. 9. Cambridge university press, 2002.

[17] S. Girimaji, "Lecture notes on turbulence processes," Spring 2018.

[18] P. Ward, *Direct Numerical Simulation of the Flow in a Pebble Bed*. PhD thesis, Texas A&M University, 2014.

[19] A. N. Kolmogorov, "The local structure of turbulence in incompressible viscous fluid for very large reynolds numbers," in *Dokl. Akad. Nauk SSSR*, vol. 30, pp. 299–303, 1941.

[20] P. Holmes, J. L. Lumley, G. Berkooz, and C. W. Rowley, *Turbulence, coherent structures, dynamical systems and symmetry*. Cambridge university press, 2012.

[21] L. Sirovich, "Turbulence and the dynamics of coherent structures. i. coherent structures," *Quarterly of applied mathematics*, vol. 45, no. 3, pp. 561–571, 1987.

[22] E. Merzari, W. Pointer, and P. Fischer, "Numerical simulation and proper orthogonal decomposition of the flow in a counter-flow t-junction," *Journal of Fluids Engineering*, vol. 135, no. 9, p. 091304, 2013.

[23] A. G. Tomboulides and S. A. Orszag, "Numerical investigation of transitional and weak turbulent flow past a sphere," *Journal of Fluid Mechanics*, vol. 416, pp. 45–73, 2000.

[24] G. S. Constantinescu and K. D. Squires, "Les and des investigations of turbulent flow over a sphere at re= 10,000," *Flow, Turbulence and Combustion*, vol. 70, no. 1-4, pp. 267–298, 2003.

[25] I. Rodriguez, R. Borell, O. Lehmkuhl, C. D. P. Segarra, and A. Oliva, "Direct numerical simulation of the flow over a sphere at re= 3700," *Journal of Fluid Mechanics*, vol. 679, pp. 263–287, 2011.

[26] L. H. Fick, E. Merzari, and Y. A. Hassan, "Direct numerical simulation of pebble bed flows: database development and investigation of low-frequency temporal instabilities," *Journal of Fluids Engineering*, vol. 139, no. 5, p. 051301, 2017.

[27] L. H. Fick, E. Merzari, and Y. A. Hassan, "Calculation of turbulent kinetic energy budgets for flow through a pebble bed using dns," in *2016 24th International Conference on Nuclear Engineering*, pp. V005T15A058–V005T15A058, American Society of Mechanical Engineers, 2016.

[28] L. H. Fick, E. Merzari, O. Marin, and Y. A. Hassan, "Investigation of the dynamics of incompressible flow in domains of multiple close-packed spheres," in *ASME 2017 Fluids Engineering Division Summer Meeting*, pp. V01BT12A007–V01BT12A007, American Society of Mechanical Engineers, 2017.

[29] J.-J. Lee, S.-J. Yoon, G.-C. Park, and W.-J. Lee, "Turbulence-induced heat transfer in pbmr core using les and rans," *Journal of Nuclear Science and Technology*, vol. 44, no. 7, pp. 985–996, 2007.

[30] J.-J. Lee, G.-C. Park, K.-Y. Kim, and W.-J. Lee, "Numerical treatment of pebble contact in the flow and heat transfer analysis of a pebble bed reactor core," *Nuclear Engineering and Design*, vol. 237, no. 22, pp. 2183–2196, 2007.

[31] A. Shams, F. Roelofs, E. Komen, and E. Baglietto, "Numerical simulations of a pebble bed configuration using hybrid (rans–les) methods," *Nuclear Engineering and Design*, vol. 261, pp. 201–211, 2013.

[32] Y. A. Hassan and E. Dominguez-Ontiveros, "Flow visualization in a pebble bed reactor experiment using piv and refractive index matching techniques," *Nuclear Engineering and Design*, vol. 238, no. 11, pp. 3080–3085, 2008.

[33] S. Mittal and V. Kumar, "Flow-induced oscillations of two cylinders in tandem and staggered arrangements," *Journal of Fluids and Structures*, vol. 15, no. 5, pp. 717–736, 2001.

[34] G.-q. Tang, C.-q. Chen, M. Zhao, and L. Lu, "Numerical simulation of flow past twin near-wall circular cylinders in tandem arrangement at low reynolds number," *Water Science and Engineering*, vol. 8, no. 4, pp. 315–325, 2015.

[35] L. Fick, E. Merzari, and Y. Hassan, "Direct numerical simulation of the flow through a structured pebble bed near a wall boundary," in *ASME/JSME/KSME 2015 Joint Fluids Engineering Conference*, pp. V001T03A008–V001T03A008, American Society of Mechanical Engineers, 2015.

[36] C. Du Toit and P. Rousseau, "Modeling the flow and heat transfer in a packed bed high temperature gas-cooled reactor in the context of a systems cfd approach," *Journal of Heat Transfer*, vol. 134, no. 3, p. 031015, 2012.

[37] B. Eisfeld and K. Schnitzlein, "The influence of confining walls on the pressure drop in packed beds," *Chemical Engineering Science*, vol. 56, no. 14, pp. 4321–4329, 2001.

[38] A. Shams, F. Roelofs, E. Komen, and E. Baglietto, "Quasi-direct numerical simulation of a pebble bed configuration. part i: Flow (velocity) field analysis," *Nuclear Engineering and Design*, vol. 263, pp. 473–489, 2013.

[39] J. H. Ferziger and M. Peric, *Computational methods for fluid dynamics*. Springer Science & Business Media, 2012.

[40] E. Merzari, W. Pointer, J. Smith, A. Tentner, and P. Fischer, "Numerical simulation of the flow in wire-wrapped pin bundles: Effect of pin-wire contact modeling," *Nuclear Engineering and Design*, vol. 253, pp. 374–386, 2012.

[41] T. Nguyen, R. Muyshondt, Y. Hassan, and N. Anand, "Experimental investigation of cross flow mixing in a randomly packed bed and streamwise vortex characteristics using particle image velocimetry and proper orthogonal decomposition analysis," *Physics of Fluids*, vol. 31, no. 2, p. 025101, 2019.

[42] A. Shams, F. Roelofs, E. Komen, and E. Baglietto, "Optimization of a pebble bed configuration for quasi-direct numerical simulation," *Nuclear Engineering and Design*, vol. 242, pp. 331–340, 2012.

[43] A. Gandhir, *Computational Analysis of Fluid Flow in Pebble Bed Modular Reactor*. PhD thesis, Texas A & M University, 2012.

[44] G. Yesilyurt, *Numerical simulation of flow distribution for pebble bed high temperature gas cooled reactors*. PhD thesis, Texas A&M University, 2004.

[45] T. Nguyen, E. Kappes, S. King, Y. Hassan, and V. Ugaz, "Time-resolved piv measurements in a low-aspect ratio facility of randomly packed spheres and flow analysis using modal decomposition," *Experiments in Fluids*, vol. 59, no. 8, p. 127, 2018.

[46] M. Ozgoren, A. Okbaz, S. Dogan, B. Sahin, and H. Akilli, "Investigation of flow characteristics around a sphere placed in a boundary layer over a flat plate," *Experimental Thermal and Fluid Science*, vol. 44, pp. 62–74, 2013.

[47] H. Zhao, X. Liu, D. Li, A. Wei, K. Luo, and J. Fan, "Vortex dynamics of a sphere wake in proximity to a wall," *International Journal of Multiphase Flow*, vol. 79, pp. 88–106, 2016.

[48] M. Tavakol, O. Abouali, and M. Yaghoubi, "Large eddy simulation of turbulent flow around a wall mounted hemisphere," *Applied Mathematical Modelling*, vol. 39, no. 13, pp. 3596–3618, 2015.

[49] C. G. Du Toit, “Radial variation in porosity in annular packed beds,” *Nuclear Engineering and Design*, vol. 238, no. 11, pp. 3073–3079, 2008.

APPENDIX A

REYNOLDS STRESSES

This appendix contains the line-out plots for the off diagonal terms of the Reynolds stress that was omitted from chapter 5.

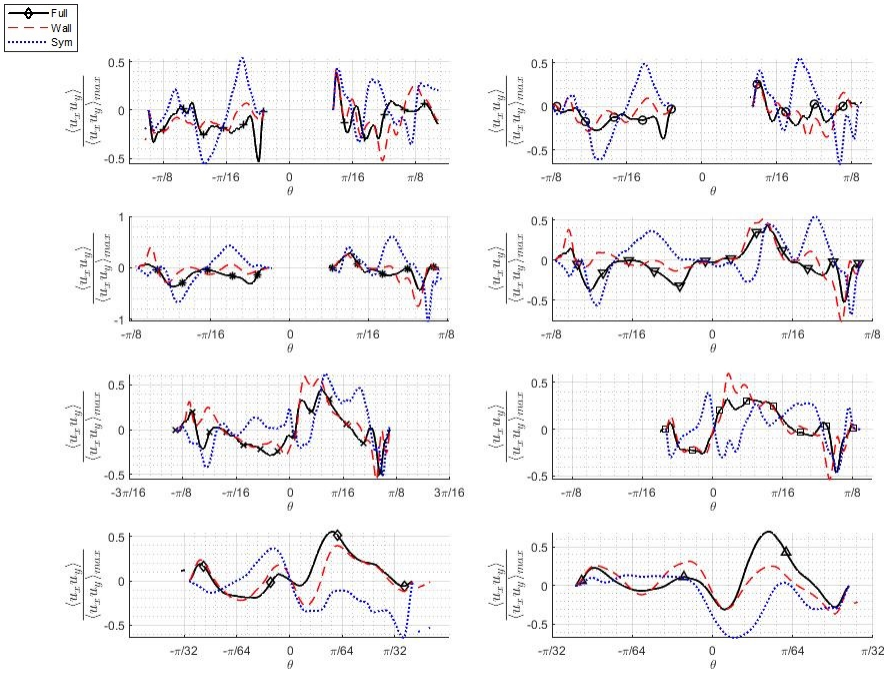

Figure A.1: Normalized interpolated line profiles for $\langle u_x u_y \rangle$. (Full: solid black, Wall: dash red, Symmetry: dot blue)

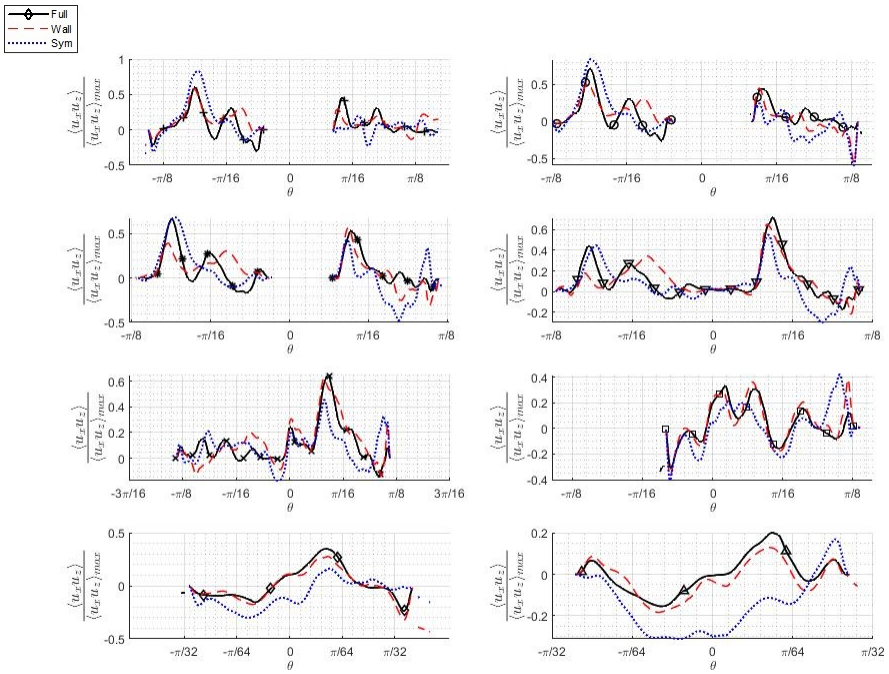

Figure A.2: Normalized interpolated line profiles for $\langle u_x u_z \rangle$. (Full: solid black, Wall: dash red, Symmetry: dot blue)

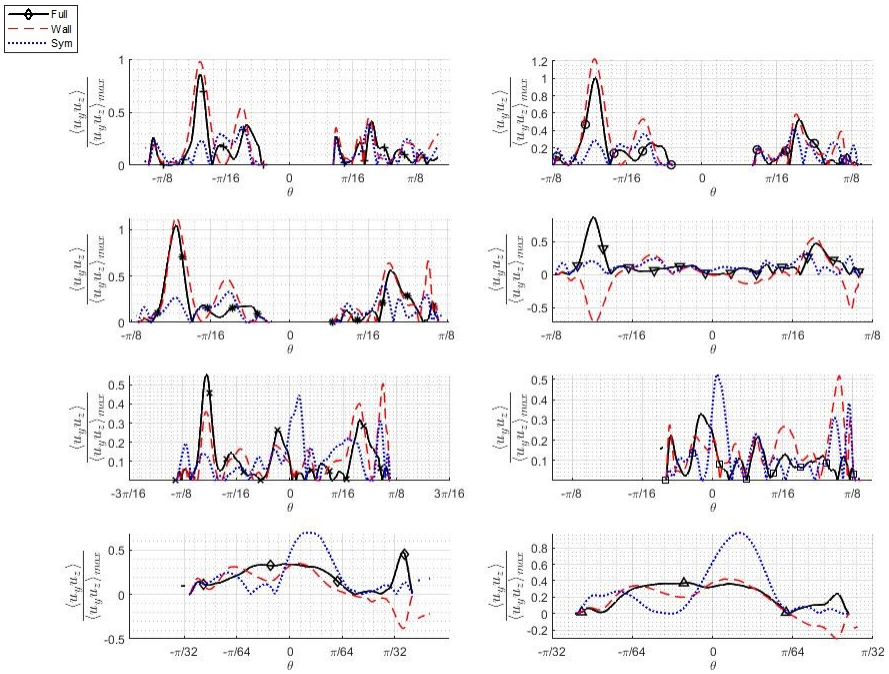

Figure A.3: Normalized interpolated line profiles for $\langle u_y u_z \rangle$. (Full: solid black, Wall: dash red, Symmetry: dot blue)

APPENDIX B

TURBULENT KINETIC ENERGY

This appendix contains the line-out plots for the TKE budgets that was not presented in Chapter 5.

B.1 Production

The line-outs of the TKE production's off diagonal components are presented here.

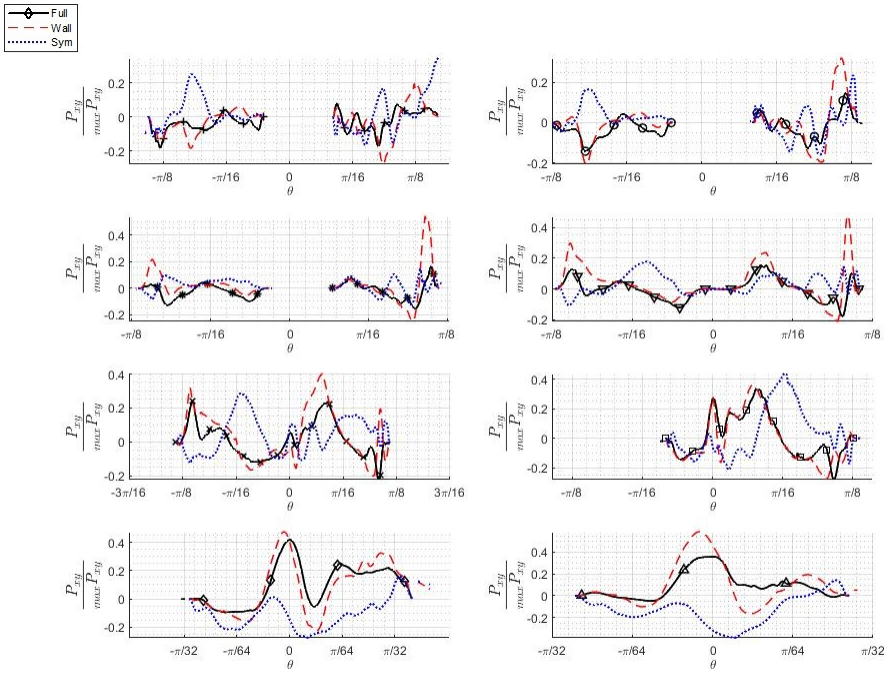

Figure B.1: Normalized interpolated line profiles for P_{xy}. (Full: solid black, Wall: dash red, Symmetry: dot blue)

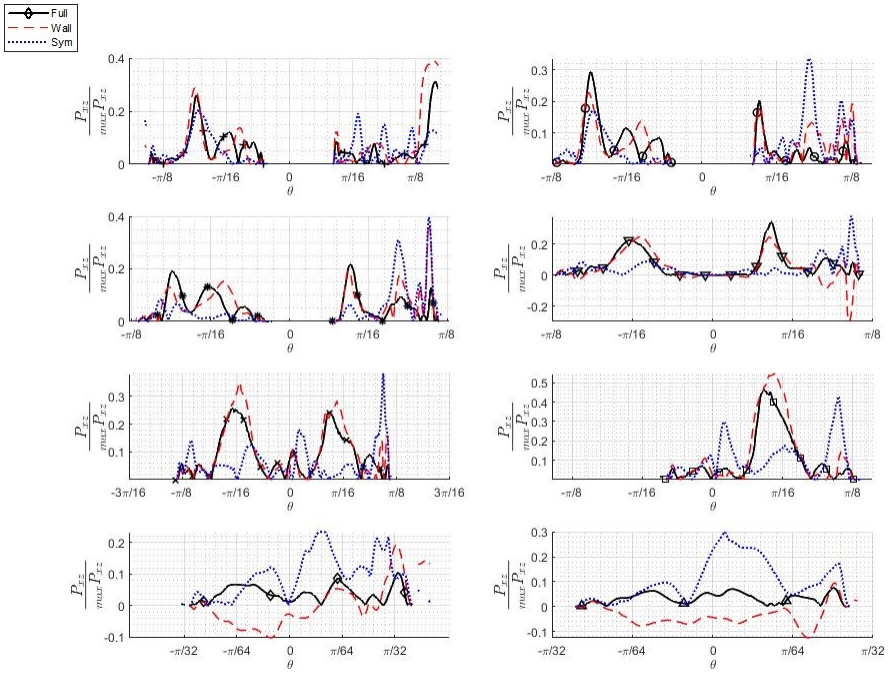

Figure B.2: Normalized interpolated line profiles for P_{xz}. (Full: solid black, Wall: dash red, Symmetry: dot blue)

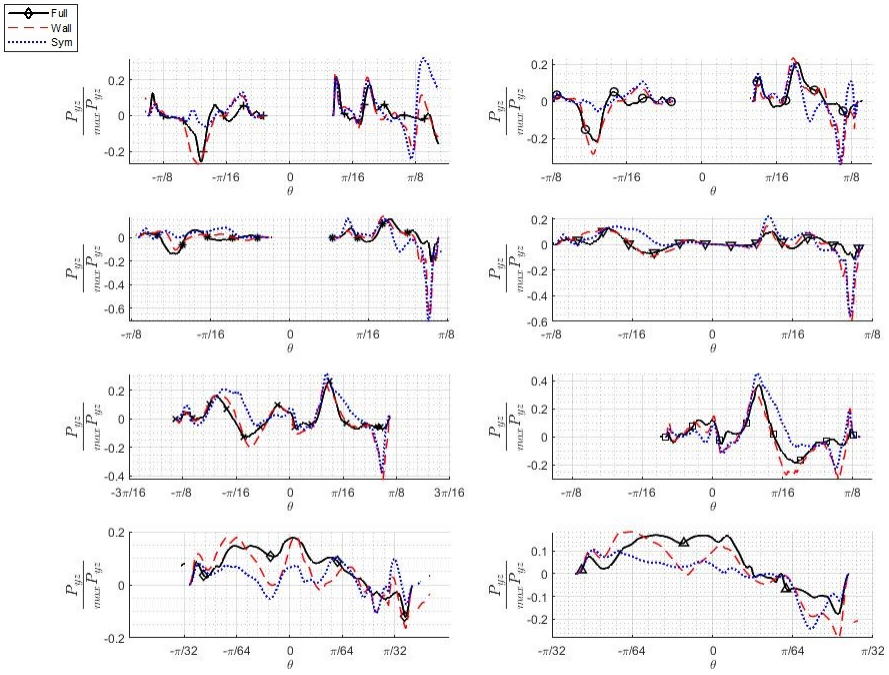

Figure B.3: Normalized interpolated line profiles for P_{yz}. (Full: solid black, Wall: dash red, Symmetry: dot blue)

B.2 Dissipation

The line-outs of the TKE dissipation's off diagonal components are presented here.

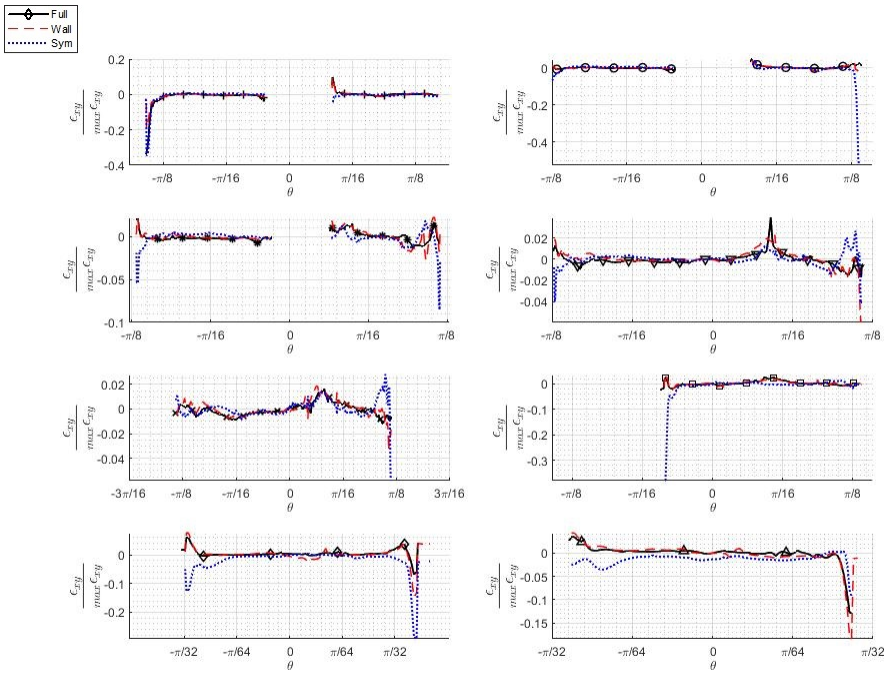

Figure B.4: Normalized interpolated line profiles for ϵ_{xy}. (Full: solid black, Wall: dash red, Symmetry: dot blue)

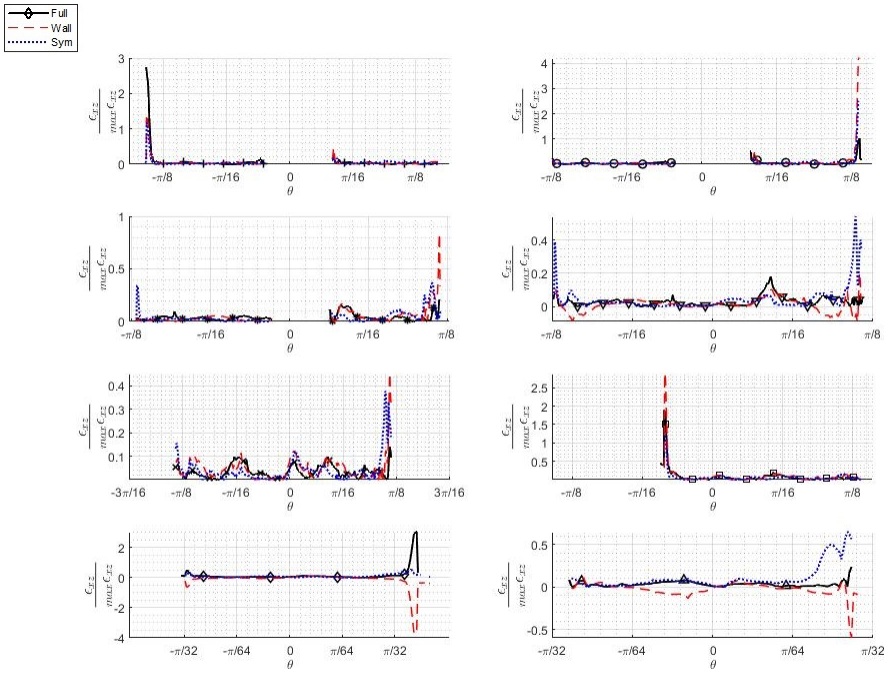

Figure B.5: Normalized interpolated line profiles for ϵ_{xz}. (Full: solid black, Wall: dash red, Symmetry: dot blue)

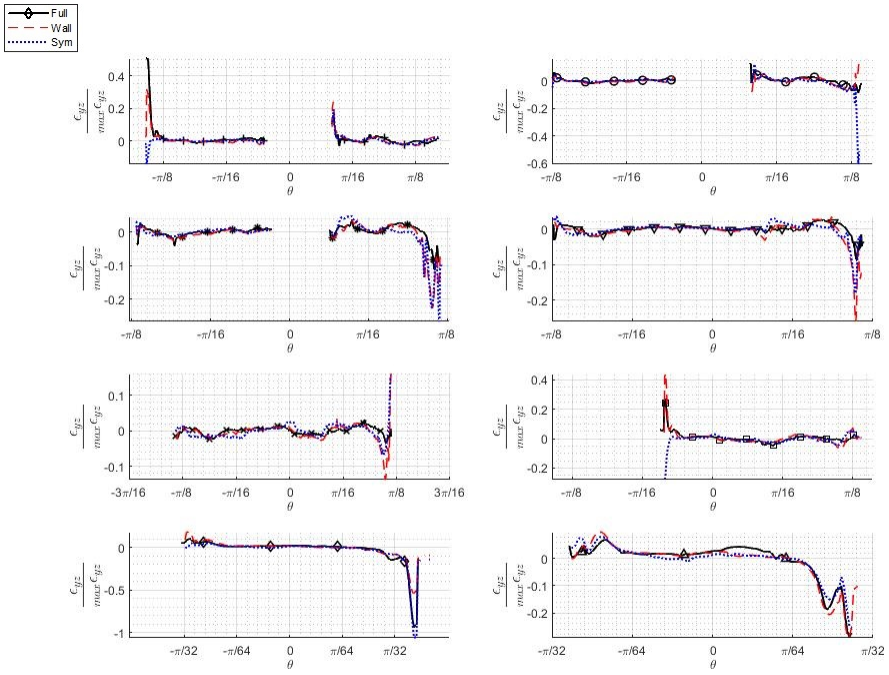

Figure B.6: Normalized interpolated line profiles for ϵ_{yz}. (Full: solid black, Wall: dash red, Symmetry: dot blue)